

Ram Pressure Stripping in High-Density Environments

Alessandro Boselli · Matteo Fossati ·
Ming Sun

Received: date / Accepted: date

Abstract Galaxies living in rich environments are suffering different perturbations able to drastically affect their evolution. Among these, ram pressure stripping, i.e. the pressure exerted by the hot and dense intracluster medium (ICM) on galaxies moving at high velocity within the cluster gravitational potential well, is a key process able to remove their interstellar medium (ISM) and quench their activity of star formation. This review is aimed at describing this physical mechanism in different environments, from rich clusters of galaxies to loose and compact groups. We summarise the effects of this perturbing process on the baryonic components of galaxies, from the different gas phases (cold atomic and molecular, ionised, hot) to magnetic fields and cosmic rays, and describe their induced effects on the different stellar populations, with a particular attention to its role in the quenching episode generally observed in high density environments. We also discuss on the possible fate of the stripped material once removed from the perturbed galaxies and mixed with the ICM, and we try to estimate its contribution to the pollution of the surrounding environment. Finally, combining the results of local and high redshift observations with the prediction of tuned models and simulations, we try to quantify the importance of this process on the evolution of galaxies of different mass, from dwarfs to giants, in various environments and at different epochs.

A. Boselli
Aix Marseille Univ, CNRS, CNES, LAM, Marseille, F-13013 France
E-mail: alessandro.boselli@lam.fr

M. Fossati
Università di Milano-Bicocca, Piazza della Scienza 3, I-20100 Milano, Italy
INAF-Osservatorio Astronomico di Brera, via Brera 28, I-20121 Milano, Italy
E-mail: matteo.fossati@unimib.it

M. Sun
Department of Physics & Astronomy, University of Alabama in Huntsville, 301 Sparkman Drive, Huntsville, AL 35899, USA
E-mail: ms0071@uah.edu

Keywords Galaxies: evolution; Galaxies: interactions; Galaxies: interstellar medium; Galaxies: star formation; Galaxies: cluster: general; Galaxies: cluster: intracluster medium

Contents

1	Introduction	3
2	The physical process	6
2.1	Properties of high-density regions	8
2.2	Galaxies physical parameters	12
2.3	Region of action	15
3	Observational evidence	18
3.1	Identification of the dominant perturbing mechanism	18
3.2	The presence of RPS tails	20
3.2.1	Radio continuum	22
3.2.2	Atomic gas	25
3.2.3	Molecular gas	27
3.2.4	Ionised gas	28
3.2.5	Hot gas	32
3.2.6	Dust	35
3.3	Indirect effects on the stellar spatial distribution	36
3.4	Truncated discs	40
3.5	Asymmetries	43
3.6	Integrated properties	45
3.7	Galaxy distribution within high-density regions	48
3.7.1	Galaxy distribution as a function the angular distance	48
3.7.2	Galaxy distribution within the phase-space diagram	49
4	The impact of RPS on galaxy evolution	51
4.1	Induced effects on the star formation process	51
4.2	Timescales for stripping and quenching	54
4.3	Nuclear activity	56
4.4	Gas and stellar kinematics	59
5	The impact of RPS on the surrounding environment	62
5.1	The fate of the stripped gas	62
5.1.1	Gas evaporation	63
5.1.2	Gas cooling into giant molecular clouds	65
5.1.3	Star formation within the tail	66
5.2	ICM clumping	68
5.3	ICM metal enrichment	69
5.4	Intracluster light and dust contribution	70
6	The importance of RPS at different epochs and in different environments	72
6.1	Clusters vs. groups and other environments	72
6.2	Evolution with cosmic time	75
7	Comparison with other mechanisms	78
7.1	Effects on galaxies and timescales	78
7.2	Region of influence	80
7.3	Dependence on structure formation	81
7.4	Effects on the surrounding environment	83
8	Conclusions	84
A	Table of galaxies suffering RPS in nearby clusters	86

1 Introduction

The environment plays a major role in shaping galaxy evolution. Since the seminal work of Dressler (1980), it is now well established that galaxies in high density regions have undergone a different evolution than their counterparts in the field. Rich environments are indeed dominated by early-type galaxies (morphology-density relation, e.g., Dressler 1980; Postman & Geller 1984; Postman et al. 2005; Whitmore et al. 1993; Dressler et al. 1997) and quiescent systems (e.g., Lewis et al. 2002; Gómez et al. 2003; Peng et al. 2010). Systematic differences between cluster and field galaxies are also observed in the late-type population. Indeed, in high density environments spirals have, on average, a lower atomic (e.g., Haynes & Giovanelli 1984; Cayatte et al. 1990; Solanes et al. 2001; Gavazzi et al. 2005; Catinella et al. 2013) and molecular (e.g., Fumagalli et al. 2009; Boselli et al. 2014b) gas content than similar objects in the field. As a consequence, their star formation activity is also reduced, especially when the molecular gas reservoir needed to feed star formation is affected (e.g., Kennicutt 1983; Gavazzi et al. 1998; Boselli et al. 2014d, 2016a).

Various perturbing mechanisms have been proposed to explain the different evolution of galaxies in high density regions (e.g. Boselli & Gavazzi 2006, 2014). These can be divided into two main families, namely the gravitational perturbations with other group or cluster members (e.g. Merritt 1983), with the gravitational potential well of the high density region itself (e.g. Byrd & Valtonen 1990), or their combined effect in multiple fly-by encounters, generally called galaxy harassment (e.g. Moore et al. 1996, 1998), or the hydrodynamic interaction of galaxies moving at high velocity ($\sigma \simeq 500\text{-}1000 \text{ km s}^{-1}$) within the hot ($T_{\text{ICM}} \simeq 10^7\text{-}10^8 \text{ K}$) and dense ($\rho_{\text{ICM}} \simeq 10^{-3} \text{ cm}^{-3}$) intracluster medium (ICM) permeating high density regions (e.g. Sarazin 1986). The hydrodynamic interaction of galaxies with the hot surrounding ICM can make the cold interstellar medium (ISM) evaporate (thermal evaporation, e.g. Cowie & Songaila 1977), or simply remove it because of the external pressure exerted on the galaxy ISM by the surrounding medium (ram pressure, e.g., Gunn & Gott 1972). The hydrodynamic friction at the interface between the cold ISM and the hot ICM in galaxies moving at high velocities can create different physical instabilities in the gas (Rayleigh-Taylor, e.g., Roediger & Hensler 2008, and Kelvin-Helmholtz instabilities, e.g. Livio et al. 1980; Nulsen 1982; Mori & Burkert 2000) which contribute to the removal of gas from the galaxy disc. Finally, it has also been proposed that once galaxies become satellites of a larger halo, the gas infall is suppressed, thus reducing the supply of fresh material to the galaxy disc on longer timescales and thus reducing the rate of formation of new stars (starvation or strangulation, e.g., Larson et al. 1980; Bekki et al. 2002; van den Bosch et al. 2008; Peng et al. 2015). *The main difference between these two families of mechanisms is that while gravitational perturbations act indifferently on all the different galaxy components (dark matter, stars, gas, dust), hydrodynamic interactions affect only the diffuse interstellar medium (e.g. Boselli & Gavazzi 2006).* Although second order effects such as induced

star formation events in the compressed gas at the interface between the hot ICM and the cold ISM (see Sec. 4.1) or the perturbation of the wind produced during the mass loss of individual evolved stars (see Sec. 3.3) are possible, this remains the main difference between hydrodynamic and gravitational perturbations, and will be used throughout this work to identify galaxies undergoing an RPS process.

First proposed in the seventies to explain the peculiar morphology of head-tail radio galaxies (e.g. Gunn & Gott 1972), RPS is often considered as the dominant perturbing mechanism in nearby rich clusters (e.g. Vollmer et al. 2001b; Boselli & Gavazzi 2006; Gavazzi et al. 2013b; Boselli et al. 2014d) where the high velocity of satellite galaxies moving within the dense ICM make the ideal conditions for a stripping process to be effective. Tuned models and simulations indicate that this mechanism can remove the cold gas reservoir of galaxies of different mass depending on their local environment, from more massive galaxies in clusters down to dwarf systems orbiting within the halo of a more massive galaxy whenever combined with tidal forces (e.g. Mayer et al. 2006). It is, however, still unclear whether ram pressure, or more in general the hydrodynamic interaction of the cold galaxy ISM with the hot surrounding ICM, is the most effective perturbing mechanism in lower mass structures such as loose (e.g. Catinella et al. 2013; Brown et al. 2017) and compact groups (e.g. Verdes-Montenegro et al. 2001), or in high redshift clusters still under formation through the assembly of smaller groups, where gravitational perturbations were probably present (pre-processing, e.g. Dressler 2004; Fujita 2004). The identification of the dominant perturbing mechanism in galaxies of different mass (from giant to dwarfs) and belonging to different environments (from massive clusters to loose groups) at different epochs is also made difficult by the fact that the different perturbing mechanisms described above, and now commonly included in hydrodynamic cosmological simulations or semi-analytic models, are all active at the same time with additive effects (e.g. Boselli & Gavazzi 2006; Weinmann et al. 2010; Bahé & McCarthy 2015; Marasco et al. 2016; Trayford et al. 2016; van de Voort et al. 2017; Henriques et al. 2015, 2017; Cortese et al. 2021). Furthermore, the fate of the stripped material once removed from the galaxy disc remains unclear. Observations and simulations indicate that this gas can either fall back on the disc once the galaxy reaches the outskirts of the cluster along its orbit (e.g. Vollmer et al. 2001b), or produce long cometary tails where, under some still unclear conditions, star formation can or not take place (e.g. Boissier et al. 2012; Jáchym et al. 2014; Fossati et al. 2016; Boselli et al. 2016a; Poggianti et al. 2019a).

The recent availability of increasingly sensitive ground- and space-based imaging and spectroscopic instruments allowed the completion of large and deep multifrequency surveys both of local clusters: Virgo (e.g. ACSVCS Côté et al. 2006, VIVA Chung et al. 2009a, HeViCS Davies et al. 2010, GUViCS Boselli et al. 2011, NGVS Ferrarese et al. 2012, VESTIGE Boselli et al. 2018c), Fornax (e.g. FCOS Mieske et al. 2004, ACSFCS Jordán et al. 2007, HeFoCS Davies et al. 2013, NGFS Muñoz et al. 2015, FDS Iodice et al. 2016, the MeerKAT Fornax Survey Serra et al. 2016, Fornax3D Sarzi et al. 2018, AIFoCS,

Zabel et al. 2019), Coma (Carter et al. 2008; Yagi et al. 2010; Smith et al. 2010; Chiboucas et al. 2011; Koda et al. 2015; van Dokkum et al. 2015; Yagi et al. 2016; Gavazzi et al. 2018b; Zaritsky et al. 2019; Chen et al. 2020; Lal 2020), A1367 (Yagi et al. 2017; Scott et al. 2018), and of higher redshift clusters (e.g. Muzzin et al. 2012; van der Burg et al. 2013, 2018; Balogh et al. 2014, 2017; Nantais et al. 2016; Rudnick et al. 2017; Galametz et al. 2018). These large observational efforts aimed at building statistical samples have been ideally complemented with targeted observations at extraordinary angular resolution of representative objects (e.g. Sun et al. 2010; Fumagalli et al. 2014; Poggianti et al. 2017b; Fossati et al. 2018) where the role of the environment on their evolution can be studied in great detail. The increasing level of detail and complexity of these observational datasets required a similar advancement of theoretical and numerical models needed for their interpretation. This led to a new class of hydrodynamic simulations (e.g. Vogelsberger et al. 2014; Schaye et al. 2015) and semi-analytic models of galaxy formation (e.g. Weinmann et al. 2010; De Lucia et al. 2012; Guo et al. 2013; Henriques et al. 2015, 2017; Hirschmann et al. 2016) which are now able to reproduce with exquisite resolution the dark matter and baryonic components (stars, dust, cold, ionised, and hot gas) of galaxies in different density regions (e.g. Luo et al. 2016; Xie et al. 2018; Stevens et al. 2019; Yun et al. 2019; Troncoso-Iribarren et al. 2020), offering the community with a unique set of tools to significantly advance in the study of the role of the environment on galaxy evolution. The synergy of the multifrequency data and of the simulations allow us to quantify the importance of the different perturbing mechanisms on large statistical samples and at the same time to study the detailed physical process down to the scale of giant molecular clouds and star forming H II regions. For these several reasons, significant improvements have been done in the recent years in the study of the RPS process. In particular, a growing interest on this mechanism comes from the discovery of spectacular tails of gas associated to some nearby cluster galaxies seen in cold atomic (e.g. Chung et al. 2007), ionised (e.g. Gavazzi et al. 2001a; Yagi et al. 2010; Boselli et al. 2016a), and hot (e.g. Sun et al. 2006, 2007a) gas, which identified with no ambiguity several objects now undergoing a stripping event. These observational results have been mirrored by high resolution hydrodynamic simulations now able to reproduce the different gas phases and the star formation process in the stripped material down to the scale of individual H II regions (e.g. Roediger & Hensler 2005; Tonnesen & Bryan 2009, 2012; Roediger et al. 2015).

It is thus time to summarise these important results reached by the astrophysical community in a review entirely dedicated to the RPS process. The purpose of this work is giving a general view of this major perturbing mechanism, summarising the properties of the physical process by means of simple analytical prescriptions, models, and more complex simulations and explain how multifrequency data can be used to identify galaxies undergoing an RPS event. The same data can be used to derive important physical parameters necessary to describe the process and to constrain tuned models and simulations. Within this review we also try to explain which are the major effects

of the perturbation on the evolution of galaxies and study the fate of the stripped gas. And finally, we try to combine all this information to derive the relationship between ram pressure and galaxy mass, halo mass, and redshift to understand and quantify which is the statistical importance and contribution of this mechanism on the evolution of galaxies. We try to do this exercise by summarising and combining the results of the growing number of papers dedicated to this interesting process, and combine their results in a coherent and self consistent picture on galaxy evolution in dense environments.

The paper is structured as follows: in Sec. 2 we describe the physical process and its relations to the properties of galaxies (mass and morphological type) and of the high density regions (mass, velocity dispersion, gas density and temperature). In Sec. 3 we summarise the multifrequency observational evidence indicating that RPS is now at place or it has contributed to modify the evolution of galaxies in dense regions. In Sec. 4 we discuss the impact of RPS on galaxy evolution, while in Sec. 5 the impact of the process on the surrounding environment. Finally, in Sec. 6 we try to derive the statistical importance of this mechanism in shaping the evolution of galaxies of different mass, in different density regions, and at different epochs. The final discussion and the conclusions are given in Sec. 7 and 8, where we compare the effects of RPS to those induced by other main perturbing mechanisms in high density regions.

2 The physical process

High density regions are generally characterised by a hot ($T \sim 10^7 - 10^8$ K) and dense ($n_{\text{ICM}} \sim 10^{-4} - 10^{-2} \text{ cm}^{-3}$) ICM trapped within their gravitational potential well (e.g. Sarazin 1986). Given its temperature, the ICM emits X-ray emission with a distribution roughly corresponding to the density square projected along the line of sight, extending up to the virial shock. A gas cloud (e.g., a galaxy with the ISM remained) moving with a velocity V relative to the ICM suffers a drag force. The drag force (by the ions in the ICM) exerts the ram pressure on the cloud that can be written as (when the relative velocity is normal to the cloud surface)¹:

$$P = \rho_{\text{ICM}} V^2 \quad (1)$$

which is able to remove the gaseous component of its ISM whenever it overcomes the gravitational forces keeping the gas anchored to the stellar disc of the galaxy. According to Kuzmin (1956) the gravitational potential Φ of an infinitely thin stellar disc of radius R at a distance z perpendicular to the disc is:

$$\Phi(R, z) = -\frac{GM_{\text{star}}}{\sqrt{R^2 + (a + z)^2}} \quad (2)$$

¹ Ram pressure of the ICM comes from ions in the ICM (mainly protons), while the contribution from electrons is tiny (similar to the ICM viscosity). On the other hand, the thermal pressure of the ICM has roughly the equal contribution from free electrons and ions.

where $a \geq 0$ is the radial scale-length. The condition for stripping the gas at a given radius R are satisfied whenever (Köppen et al. 2018):

$$P \geq \Sigma_{\text{gas}} \left| \frac{\partial \Phi(R, z)}{\partial z} \right|_{\text{max}} = G \Sigma_{\text{gas}} M_{\text{star}} \left| \frac{(a+z)}{(R^2 + (a+z)^2)^{3/2}} \right|_{\text{max}} \quad (3)$$

which occurs at a height z_{max} from the disc given by $\partial^2 \Phi / \partial z^2 = 0$. Roediger & Hensler (2005) analysed the variation of z_{max} as a function of radius showing that for increasing R the maximum gravitational resistance occurs at larger distances from the disc. Assuming an exponential profile for the disc density, and defining the maximum restoring force above the disc (at given R) as a threshold gives the traditional Gunn & Gott (1972) criterion for instantaneous stripping (see also Fujita et al. 1999; Yamagami & Fujita 2011):

$$\rho_{\text{ICM}} V_{\perp}^2 > 2\pi G \Sigma_{\text{star}} \Sigma_{\text{gas}} = \frac{v_{\text{rot}}^2 \Sigma_{\text{gas}}}{R_{\text{gal}}} \quad (4)$$

where $\Sigma_{\text{star}} = v_{\text{rot}}^2 / 2\pi G R_{\text{gal}}$ (from Virial equilibrium), and Σ_{gas} are the stellar and total gas surface densities, v_{rot} the rotational velocity of the galaxy, and R_{gal} is the disc scale radius. The RPS thus depends on both the properties of the high density region (ρ_{ICM}), on the motion of the galaxy within it (V , where V_{\perp} indicate the component perpendicular to the galaxy disc plane), and on the physical properties of the galaxies themselves (Σ_{star} , Σ_{gas} , v_{rot} , and R_{gal}). It is important to underline that ram pressure is an hydrodynamic interaction between two different gas phases, the (mainly cold) ISM of the perturbed galaxy with the (mainly hot) ICM. For this reason stars, which have a very small cross section to the gas flow and much higher internal pressure than the external ram pressure, are unperturbed during the interaction. Second order effects, due to the heating of the stellar disc after the stripping of the gaseous disc, can be present (see Sec. 4.4). They can induce a mild change of the orbits of the stars which produces ultra diffuse discs (Safarzadeh & Scannapieco 2017). These effects on the structure of the stellar disc are expected to be more important in dwarf systems, where the gravitational potential well of the galaxy is the shallower.

RPS is a general process in astronomy whenever there is a relative bulk motion between a moving object and its surroundings, e.g., mergers of galaxy clusters and groups (elongation and trails on the X-ray morphology), bent radio jets and the stripped ISM at the scale of galaxies, pulsar wind nebulae, stellar wind (including the heliosphere) at the scale of stars and compact objects. RPS can also work on individual stars, especially on those with strong winds. One of the best examples at the scale of stars is the Mira star with a 4 pc tail (Martin et al. 2007) that is believed to be mainly composed of H_2 gas². In this review, however, we focus on the RPS process occurring on galaxy scales.

² The ram pressure Mira experiences is only $\sim 1.3 \times 10^{-11}$ dyn (assuming H I gas), which is only typical for the RP experienced by cluster galaxies at the cluster outskirts. Thus, an AGB star like Mira soaring in the ICM with a velocity of ~ 2000 km s⁻¹ can have a tail of ~ 0.06 kpc.

2.1 Properties of high-density regions

The external pressure acting on the disc of spiral galaxies inhabiting clusters depends on two main parameters, the ICM density ρ_{ICM} that is tied to the ICM gas fraction of the cluster and the velocity of the galaxy with respect to the ICM V that is tied to the cluster mass. We thus summarize some cluster properties and relations useful for this work, while readers are referred to dedicated cluster review papers (e.g. Sarazin 1986; Voit 2005; Kravtsov & Borgani 2012) for more detail. Two fundamental properties of clusters are mass and size, which are often connected. While new characteristic sizes of clusters like the mean matter density radius and splashback radius have been proposed (e.g. Kravtsov & Borgani 2012), we still use the virial radius in this work. Particularly, the virial radius adopted in this work is r_{200} (r_{Δ} as the radius enclosing an overdensity of Δ times the critical density of the Universe at that redshift). r_{500} and r_{101} are also widely used in cluster studies. Typically $r_{500}/r_{200} \sim 2/3$ and $r_{500}/r_{101} \sim 1/2$ for clusters.³ The relation between any two over-density radii can be derived by assuming a total mass model. For the NFW model, $r_{2500}/r_{500} = 0.405$, $r_{500}/r_{200} = 0.638$ and $r_{200}/r_{101} = 0.730$ for $c_{200} = 3$, where $c_{200} = r_{200}/r_s$, with r_s as the characteristic radius in the NFW profile. $r_{2500}/r_{500} = 0.479$, $r_{500}/r_{200} = 0.677$ and $r_{200}/r_{101} = 0.755$ for $c_{200} = 8$.

By definition:

$$M_{\Delta} = \Delta \frac{4}{3} \pi r_{\Delta}^3 \rho_{\text{crit}}(z) \quad (5)$$

where $\rho_{\text{crit}}(z)$ is the critical density of the Universe at redshift z . For example, $M_{200} = 1.14 \times 10^{14} M_{\odot} (r_{200}/\text{Mpc})^3 E(z)^2$, where:

$$E(z)^2 = \Omega_M(1+z)^3 + \Omega_{\Lambda} \quad (6)$$

In this work, we use several systems with different mass as examples (see Table 1). The dominant mass component in clusters is dark matter ($\sim 85\%$ of the total mass). The dark matter distribution in clusters is often approximated with a NFW radial profile (Navarro et al. 1997) of the form:

$$\rho(r) = \rho_{\text{crit}} \frac{\delta_c}{r/r_s(1+r/r_s)^2} \quad (7)$$

with

$$\delta_c = \frac{200}{3} \frac{c^3}{\ln(1+c) - c/(1+c)} \quad (8)$$

where $c = r_{200}/r_s$ is the concentration parameter (or c_{200} here as r_{200} is adopted), r_s the scale radius of the density distribution and ρ_{crit} is again

³ Different definitions of the virial radius were used in different works, e.g., r_{200} , r_{180} and r_{101} (see e.g., Bryan & Norman 1998 for detail).

Table 1 Cluster parameters used in this work

Cluster	Luminosity distance (Mpc)	r_{200} (Mpc)	M_{200} ($10^{14} M_{\odot}$)	Ref
Virgo	16.5	0.974	1.06	1, 2
Norma	69.6	1.80	6.75	3, 4
Coma	100	1.97	8.90	5, 6
A1367	92.2	1.41	3.26	7, 4
Group	-	0.70	0.39	8

References: 1) [Gavazzi et al. \(1999\)](#) and [Mei et al. \(2007\)](#) 2) Adapted from [Simionescu et al. \(2017\)](#) using a distance of 16.5 Mpc; 3) [Woudt et al. \(2008\)](#); 4) The mass values of the Norma cluster and A1367 are estimated with the $M - T$ relation from [Sun et al. \(2009\)](#) with T of 5.6 keV and 3.6 keV respectively. 5) [Colless & Dunn \(1996\)](#); 6) [Planck Collaboration et al. \(2013\)](#) and [Churazov et al. \(2021\)](#); 7) [Cortese et al. \(2004b\)](#); 8) [Sun et al. \(2009\)](#), galaxy group with a mass similar to Fornax. Notes: all values are measured using $H_0 = 70 \text{ km s}^{-1} \text{ Mpc}^{-1}$, $\Omega_M = 0.3$, $\Omega_{\Lambda} = 0.7$.

the critical density of the Universe. For this analytic density distribution, the total mass within a radius r is given by the relation:

$$M(< r) = M_0 \left[\ln \left(1 + \frac{r}{r_s} \right) - \frac{r/r_s}{1 + r/r_s} \right] \quad \text{for } r \leq r_s c \quad (9)$$

with

$$M_0 = 4\pi \frac{3H_0^2}{8\pi G} E(z)^2 \frac{200c^3 r_s^3}{3 [\ln(1+c) - c/(1+c)]} \quad (10)$$

Other forms of mass distribution for dark matter halos have also been suggested (see e.g., [Merritt et al. 2006](#) for details).

Most baryons in clusters are in the hot ICM emitting X-rays. The classical model on the ICM density profile is the β -model (see e.g., [Sarazin 1986](#) for details), with the ICM density proportional to $r^{-3\beta}$ asymptotically beyond the central core. However, a single β -model (or even a double β -model) has been shown to be too simple to describe the ICM density profile, with β typically increasing with radius at the cluster outskirts (e.g., [Croston et al. 2008](#); [Morandi et al. 2015](#)). A typical ICM density profiles is shown in Fig. 1, from stacking the Chandra data of 320 clusters. This median density profile can be approximated with a form first introduced by [Patej & Loeb \(2015\)](#):

$$E(z)^{-2} n_e(x) = 0.00577 \left(\frac{x}{0.201} \right)^{-0.150} \left(\frac{x}{0.265} \right)^{-0.0638} [1 + 0.759 \left(\frac{x}{0.201} \right)^{0.949}]^{-2.936} \quad (11)$$

where $x = \frac{r}{r_{200}}$. This fit is good at $x = 0.02 - 1.3$ and β increases to 1 at the cluster outskirts ($n_e \propto r^{-3\beta}$), same as the asymptotic behaviour of the NFW profile. ⁴ There is significant scatter on the ICM density profiles (as well

⁴ Note that many recent cluster works adopted the ICM density profile first proposed by [Vikhlinin et al. \(2006\)](#) (their equation 3). However, unlike the model proposed by [Patej & Loeb \(2015\)](#), this model is not physically motivated. Nevertheless, the best fit

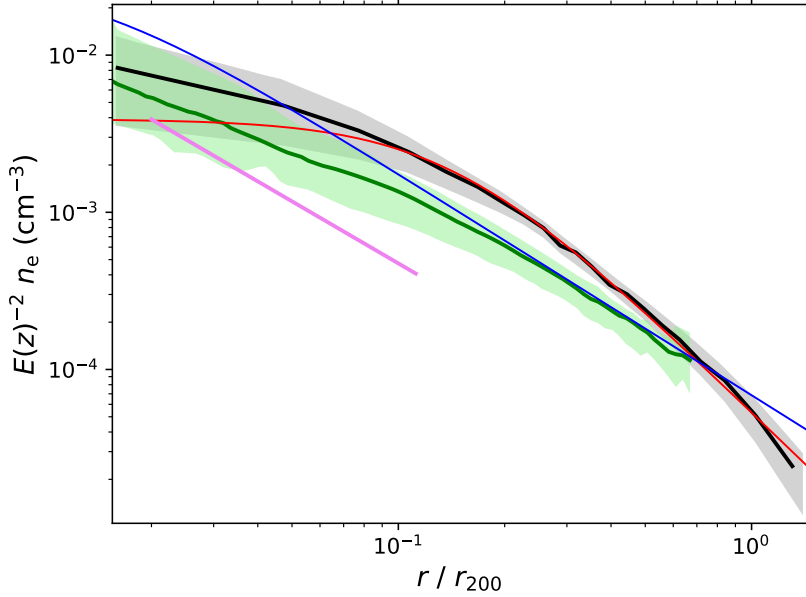


Fig. 1 The typical electron density radial profile of galaxy clusters, groups and massive spiral galaxies. The black profile and the grey shaded area show the median density and 1σ scatter for a sample of 320 galaxy clusters from [Morandi et al. \(2015\)](#). The red curve shows the electron density radial profile of the Coma cluster from the eRosita data ([Churazov et al. 2021](#)), as an example of clusters with a flat central core lacking a large, dense cool core. The blue curve shows the electron density radial profile of the Virgo cluster from the ROSAT data ([Schindler et al. 1999](#)), as an example of clusters hosting a dense, peaked cool core. The green profile and the lightgreen shaded area show the median density and 1σ scatter for a sample of 43 galaxy groups from [Sun et al. \(2009\)](#). The magenta profile shows the the electron density radial profile of a massive spiral galaxy NGC 6753 from [Bogdán et al. \(2017\)](#). The hot gas content in the inner regions generally decreases with the decreasing mass, likely demonstrating the increasing impact of baryon physics with decreasing mass.

as azimuthal variations not shown here), especially around the cluster centre (e.g., cool core as in the Virgo cluster vs. non-cool core as in the Coma cluster). With the relations presented above we can write:

$$\rho_{\text{ICM}} = 1.92 \mu n_e m_p = 1.15 n_e m_p \quad (12)$$

where $\mu = 0.60$ is the mean molecular weight for a metallicity of 0.3 - 1.0 Z_{\odot} with the solar abundance table from [Asplund et al. \(2009\)](#).

is also given here: $E(z)^{-2} n_e(x) = 0.00472 \left(0.0818 \left(\frac{x}{0.0735} \right)^{-0.769} \left[1 + \left(\frac{x}{0.0735} \right)^2 \right]^{-0.897} \left[1 + \left(\frac{x}{0.280} \right)^3 \right]^{-0.570} \right)^{1/2}$, good for $x = 0.02 - 1.1$. Note that the central component of the [Vikhlinin et al. \(2006\)](#) model is not included as the density profile does not include the very central core.

The self-similar relations for properties of galaxy clusters, originally proposed by Kaiser (1986) (also see reviews in e.g., Böhringer et al. 2012; Kravtsov & Borgani 2012), treat galaxy groups and clusters of different masses as identical objects after scaled by their mass. The useful self-similar relations for this work are summarized here (at a fixed over-density Δ).

Total mass and the ICM mass:

$$M_{\Delta} \text{ (or } M_{\text{ICM},\Delta}) \propto E(z)^{-1} \quad (13)$$

However, this evolution solely comes from the definition of M_{Δ} while observations suggest stronger evolution than $E(z)^{-1}$ from the cluster growth (e.g., Kravtsov & Borgani 2012). The ICM properties typically depend on both mass and redshift.⁵

Radius:

$$r_{\Delta} \propto M_{\Delta}^{1/3} E(z)^{-2/3} \quad (14)$$

ICM density:

$$n_e \propto E(z)^2 \quad (15)$$

ICM temperature:

$$T \propto M_{\Delta}^{2/3} E(z)^{2/3} \quad (16)$$

ICM pressure:

$$P \propto n_e T \propto M_{\Delta}^{2/3} E(z)^{8/3} \quad (17)$$

Note that the ICM density is independent of mass with the self-similar assumption. Assuming dark matter particles, ICM and cluster galaxies are all virialized in the same potential,

Galaxy velocity dispersion:

$$\sigma_v \propto T^{1/2} \propto M_{\Delta}^{1/3} E(z)^{1/3} \quad (18)$$

The galaxy velocity dispersion is a robust measure of the cluster mass, with the expected self-similar relation (e.g., Armitage et al. 2018). On the other hand, the observed $\sigma_v - T$ correlation is typically steeper than the self-similar relation with an average slope of 0.6 - 0.7 (e.g., Lovisari et al. 2021). Using σ_v as the typical velocity of cluster galaxies, ram pressure should follow the same relation as the ICM pressure. The above relation would also suggest the crossing time in the cluster, $2R_{\Delta}/\sigma_v \propto E(z)^{-1}$, and is independent of the mass. However, the $E(z)^{-1}$ factor simply comes from the definition of the cluster size (r_{Δ}), also as the free-fall time of the cluster has the same $E(z)^{-1}$ dependency.

The above self-similar relations serve as the simplest model for the ICM mass scaling and evolution, while the actual ICM scaling and evolution can be different from scale-dependent physical processes (e.g., baryonic processes like radiative cooling, AGN feedback and galactic wind) and the fact that some assumptions for the self-similar model are not accurate (e.g., Kravtsov

⁵ We did not use the equation 13 in the following equations as we want to keep the mass dependency and the equation 13 is not correct for real clusters.

& Borgani 2012). Observations have shown the importance of baryon physics, most significant in low-mass systems, e.g., elevated hot gas entropy in low-mass systems, a significant mass dependency on the hot gas fraction from massive galaxies, to galaxy groups and clusters and an observed $L_X - M$ relation steeper than the self-similar relation (e.g., Sun 2012; Lovisari et al. 2021; Eckert et al. 2021). We also plot the median density profile of local galaxy groups from Sun et al. (2009) in Fig. 1, as well as the density profile of a massive spiral. One can clearly see the mass dependency of the density profile, unlike the simple self-similar relation. The mass dependency of the ICM density likely varies with radius (e.g., Sun 2012). If we assume $n_e \propto M^{\sim 0.3}$ from Sun (2012) at $r \sim r_{2500}$ and $\sigma_V \propto M^{1/3}$ (still follow the self-similar relation), $P_{RP} \propto M^{\sim 1.0}$, steeper than the expected relation from the self-similar relations. The observed $T - M$ relations typically have a slope of ~ 0.6 , somewhat smaller than $2/3$ (e.g., Sun 2012; Lovisari et al. 2021). Thus, observations reveal departure from the self-similar relations of equations 15 - 18, as the ICM properties are not only determined by gravitational processes.

The redshift evolution of the ICM and cluster properties demonstrates the roles of RPS with redshift. Recent sample studies suggested self-similar evolution for the ICM density at $r > 0.2 r_{500}$, but weak to no evolution within $0.2 r_{500}$ (McDonald et al. 2017; Ghirardini et al. 2021), which only occupies 0.24% of the cluster volume within r_{200} . Simulations also suggest self-similar evolution to $z \sim 2.5$ (e.g., Mostoghiu et al. 2019). The evolution is significant, $E(z)^2 = 3.1$ and 8.8 at $z = 1$ and $z = 2$ respectively (for $\Omega_M = 0.3$ and $\Omega_\Lambda = 0.7$). This suggests a stronger role of RPS at higher z , at fixed cluster mass, although the abundance of massive clusters decreases with z .

Besides the relations of global properties of the ICM, the efficiency of the micro transport processes in the ICM is also important in the studies of RPS and the associated tails. Giving the low ICM density, the mean free path of particles in the ICM is large (Sarazin 1986):

$$\lambda = 23 \left(\frac{kT_{\text{ICM}}}{10^8 \text{ K}} \right)^2 \left(\frac{n_e}{10^{-3} \text{ cm}^{-3}} \right)^{-1} \text{ kpc} \quad (19)$$

This is comparable to the sizes of galaxies. However, magnetic field in the ICM significantly affects the micro transport processes in the ICM (e.g., Donner et al. 2018). While studies with the Chandra and XMM data on the ICM suggest suppression of heat conductivity and viscosity in the ICM (e.g., Markevitch & Vikhlinin 2007; Simionescu et al. 2019), the most definite constraints require high energy resolution X-ray spectroscopy at arcsec scales, coupled with the high-angular resolution X-ray morphological studies. On the other hand, potentially kinematic and morphological studies of RPS tails can also put constraints on the efficiency of the micro transport processes in the ICM.

2.2 Galaxies physical parameters

The gravitational forces keeping the ISM anchored to the stellar disc of the galaxies can be derived from the observed radial variation of gas and stellar

surface density or of the rotation curve. The radial variation of these three variables in unperturbed late-type systems is well known, and can be derived from observational data or analytically predicted using simple relations. The stellar and total gas components can be well represented by an exponentially declining disc, in particular in the outer regions, those most easily perturbed by an RPS event (Freeman 1970; Bigiel & Blitz 2012; Wang et al. 2014). For these distributions the gas and stellar density profiles (Domainko et al. 2006; Cortese et al. 2007) are:

$$\Sigma_{gas,star}(r) = \frac{M_{gas,star}}{2\pi R_{0gas,star}^2} \exp\left(-\frac{R}{R_{0gas,star}}\right) \quad (20)$$

where $R_{0gas,star}$ is the scale-length of the exponential profile of the gas and stellar distribution (for alternative scaling relations, see Wang et al. 2016; Stevens et al. 2019). Similarly, the radial variation of the rotational velocity of galaxies of different mass or luminosity can be parametrised using the Polyex function (Catinella et al. 2006) or the universal rotation curve function (Persic & Salucci 1991). From the above relations Domainko et al. (2006) also derived the radius outside which gas can be stripped r_{strip} :

$$R_{strip} \geq \left(1 + \frac{R_{0,star}}{R_{0,gas}}\right)^{-1} \ln\left(\frac{GM_{star}M_{gas}}{2\pi\rho_{ICM}V_{perp}^2 R_{0,star}^2 R_{0,gas}^2}\right) \quad (21)$$

By analysing a sample of 33 nearby galaxies with available HI and CO resolved maps from the THINGS and HERACLES surveys, Bigiel & Blitz (2012) have shown that the total gas surface density (total gas = 1.36(HI+H₂) to account for Helium) radial profile has a fairly universal form given by the relation:

$$\Sigma_{gas}(R) = 2.1\Sigma_{trans} \exp\left(-\frac{1.65r}{R_{25}}\right) \quad (22)$$

where Σ_{trans} is the surface density of the total gas when $\Sigma_{HI} = \Sigma_{H_2}$ and r_{25} is the isophotal radius measured in the *B*-band at 25 mag arcsec⁻². Given the shape of the radial profile, they have also derived that the total gas mass is given by the relation (Bigiel & Blitz 2012):

$$M_{gas} = 2\pi \times 2.1 \times \Sigma_{trans} \times R_{25}^2 \times X \quad (23)$$

with X changing with radius ($X = 0.31$ at $2 \times R_{25}$). They have also shown that Σ_{trans} is fairly constant in galaxies of different morphological type:

$$\Sigma_{trans} \simeq 14 \text{ M}_{\odot}\text{pc}^{-2} \quad (24)$$

Using standard scaling relations such as those reported in Boselli et al. (2014b) we can also estimate the total gas mass for a galaxy of given stellar mass M_{star} :

$$M_{gas} = 10^{(0.26 \log M_{star} + 7.03)} \quad (25)$$

with both entities expressed in solar units, when M_{gas} has been derived using the luminosity dependent X_{CO} conversion factor given in Boselli et al. (2002).

Using the relations above and considering that in an exponentially declining stellar disc with a typical central surface brightness of $\mu_0(B) = 21.65$ mag arcsec $^{-2}$ (Freeman 1970) $r_{25} = 3.1 R_{0,\text{star}}$, we can derive the typical scalelength of the stellar disc expressed as a function of the total gas mass:

$$R_{0,\text{star}}[\text{pc}] = \left(\frac{M_{\text{gas}}}{550} \right)^{0.5} \quad (26)$$

with M_{gas} in solar units. These leads to:

$$\Sigma_{\text{gas}}[\text{M}_{\odot} \text{ pc}^{-2}] = 29.4 \exp\left(-\frac{R}{R_{0,\text{gas}}}\right) \quad (27)$$

with $R_{0,\text{gas}} = 1.89 R_{0,\text{star}}$ ⁶, consistent with the assumption made by Cortese et al. (2007) based on the observed relation between isophotal optical and H I radii derived by Cayatte et al. (1994) ($R_{25}/r_{\text{HI}} \simeq 1.8$ measured at a column density of 10^{20} cm $^{-2}$, corresponding to $0.8 \text{ M}_{\odot} \text{ pc}^{-2}$). As an example, Fig. 2 shows the relation between the gravitational forces derived using resolved stellar mass surface densities (from Cortese et al. (2012)) and H I column densities (from the VIVA survey, Chung et al. (2009a)) and the ram pressure measured at the cluster projected distance for the sample of Virgo cluster late-type galaxies undergoing an RPS event listed in Table 2. The left panel shows the relation derived within the effective radius, while the right panel within the 25 mag arcsec $^{-2}$ isophotal radius. Figure 2 clearly shows that the external pressure is sufficient to remove the diffuse ISM in the outer disc in all galaxies, but also within the effective radius in most of the objects (NGC 4294, 4330, 4388, 4396, 4402, 4522).

All these scaling relations allow us to express R_{strip} , M_{strip} (mass of gas stripped during the interaction):

$$M_{\text{strip}} = M_{\text{gas}} \left[\left(\frac{R_{\text{strip}}}{R_{0,\text{gas}}} + 1 \right) \exp\left(-\frac{R_{\text{strip}}}{R_{0,\text{gas}}}\right) \right] \quad (28)$$

and M_{retain} (mass of gas retained on the galaxy disc):

$$M_{\text{retain}} = M_{\text{gas}} \left[1 - \left(\frac{R_{\text{strip}}}{R_{0,\text{gas}}} + 1 \right) \exp\left(-\frac{R_{\text{strip}}}{R_{0,\text{gas}}}\right) \right] \quad (29)$$

as a function of a single galaxy parameter M_{star} . Despite being a simplification of a more complex reality (galaxy discs are not infinitely thin and stable and we neglected the role of bulges), these relations are successful in reproducing the stripping radius of objects which are clearly undergoing RPS (see e.g. Arrigoni Battaia et al. 2012; Fossati et al. 2012).

⁶ We recall that in such a configuration $R_{0,\text{star}} = 0.32 R_{25}$, the effective radius (radius including half of the total galaxy luminosity), $R_{\text{eff}} = 0.59 R_{25}$, and $R_{0,\text{gas}} = 0.61 R_{25}$.

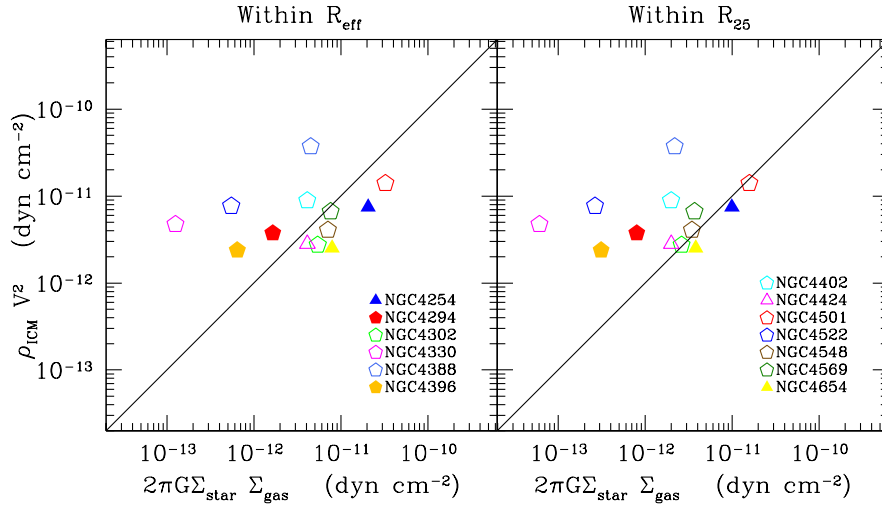


Fig. 2 Comparison between the external pressure exerted on different Virgo cluster galaxies suffering an RPS event (listed in Table 2) and moving at a velocity V within the ICM ($\rho_{\text{ICM}}V^2$, where ρ_{ICM} is the density of the ICM from Equation 12 here measured at the projected distance of the galaxy from the cluster centre) and the gravitational forces keeping the gas anchored to the stellar disc $2\pi G\Sigma_{\text{star}}\Sigma_{\text{gas}}$, in units of dyn cm^{-2} . V is the 3D velocity of galaxies within the cluster, and it is here defined as $V = \sqrt{3} \times |v_{\text{Galaxy}} - v_{\text{Virgo}}|$, where v_{Galaxy} and v_{Virgo} are the observed heliocentric velocities of the galaxies and of the Virgo cluster (955 km s^{-1}), whenever $|v_{\text{Galaxy}} - v_{\text{Virgo}}| > \sigma_{\text{Virgo}} = 799 \text{ km s}^{-1}$, otherwise $V = \sqrt{3} \times \sigma_{\text{Virgo}}$.

In the left panel the gravitational forces are measured within the effective radius, in the right panel within the 25 mag arcsec $^{-2}$ radius. Empty symbols are for HI-deficient galaxies, filled ones for HI-normal objects. Pentagons indicate galaxies undergoing an RPS event, triangles objects suffering RPS combined with a gravitational perturbation.

2.3 Region of action

Taking advantage of the galaxy scaling relations and properties shown in Sections 2.2 and 2.1 and of the typical density profiles of the ICM in clusters we can now study the impact of RPS on galaxies as a function of their position and orbit within the cluster, of their stellar mass, and of the mass of the host halo.

Figure 3 shows the expected variation of the stripping radius as a function of the stellar mass for galaxies in three different environments, the Coma cluster, the Virgo cluster, and a representative group of total mass $M_{\text{group}} \simeq 4 \times 10^{13} M_{\odot}$ comparable to the Fornax cluster (whose parameters are given in Table 1) derived using the scaling relations given above. The expected variations are measured at $0.2 \times r_{200}$, $0.5 \times r_{200}$, and r_{200} , where the density of the ICM, ρ_{ICM} , is derived from the X-rays radial profile given in Fig. 1 assuming eq. 12 and a velocity within the cluster $V = \sqrt{3} \times \sigma_{LT}$, where σ_{LT} is the line of sight velocity dispersion of the high density region for the late-type galaxy population.

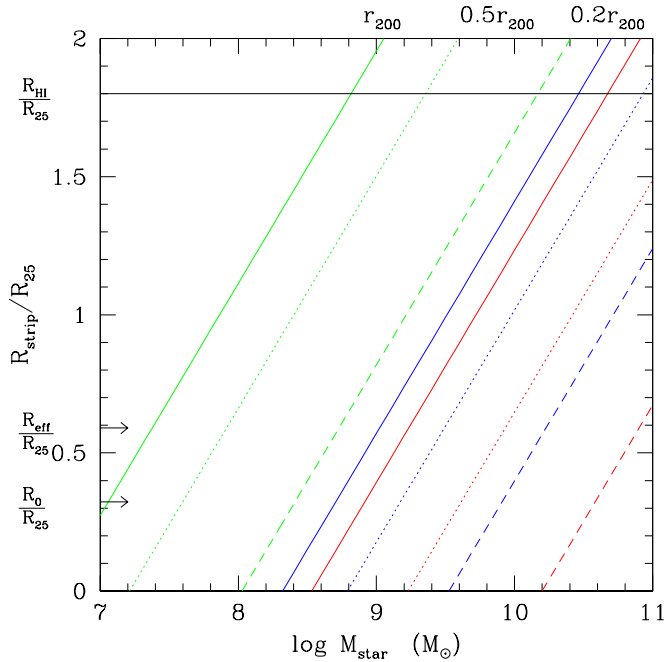


Fig. 3 Expected variation of the stripping radius R_{strip} normalised to the B -band isophotal radius at 25 mag arcsec $^{-2}$ as a function of the stellar mass M_{star} for galaxies in the Coma cluster (red), in the Virgo cluster (blue), and in a representative group of total mass $M_{\text{tot}} \simeq 4 \times 10^{13} M_{\odot}$ (green) derived using the scaling relations given above. The external pressure is estimated assuming as typical velocity of galaxies within the different clusters $V = \sqrt{3} \times \sigma_{LT}$, with σ_{LT} the mean velocity dispersion of late-type systems. The expected variations are measured at $0.2 \times r_{200}$ (dashed), $0.5 \times r_{200}$ (dotted), and r_{200} (solid). All gas outside the predicted lines can be potentially removed during an RPS event. The arrows on the Y-axis indicate the effective radius-to-isophotal radius R_{eff}/R_{25} and the exponential scalelength-to-isophotal radius $R_{0,\text{star}}/R_{25}$ for an exponentially declining stellar profile of central surface brightness $\mu_0(B) = 21.65$ mag arcsec $^{-2}$. The black horizontal solid line indicates the typical HI-to-isophotal radius $R_{\text{HI}}/R_{25} = 1.8$ measured at a column density of $\Sigma_{\text{HI}} = 10^{20}$ cm $^{-3}$ ($0.8 M_{\odot}$ pc $^{-2}$) by Cayatte et al. (1990)

Figure 3 clearly shows that, in a massive cluster such as Coma, all star forming galaxies of stellar mass $M_{\text{star}} \leq 10^{8.3} M_{\odot}$ can be completely stripped of their total gas content up to the virial radius of the cluster r_{200} , those of stellar mass $M_{\text{star}} \leq 10^{10.2} M_{\odot}$ only if they cross the cluster in the inner regions ($r \leq 0.2 \times r_{200}$). In the same cluster stripping is also able to remove all the gas located outside the optical disc ($\simeq 50\%$ of the total gas content) in galaxies of stellar mass $M_{\text{star}} \leq 10^{9.5} M_{\odot}$ up to the cluster virial radius. As expected, the gas stripping efficiency decreases in lower-density environments but it is still dominant in clusters of the mass of Virgo ($M_{\text{cluster}} \simeq 10^{14} M_{\odot}$), and can be important in groups in low mass galaxies crossing the ICM in the inner regions. In this configuration ($r \leq 0.2 \times r_{200}$), all galaxies of stellar mass $M_{\text{star}} \leq 10^{8.0} M_{\odot}$ can be completely stripped of their gas, while those with

$M_{\text{star}} \leq 10^{9.1} M_{\odot}$ stripped of their gas located outside the optical radius. For a more accurate analytical description of the process, we refer the reader to [Hester \(2006\)](#).

In [Fig. 3](#) the truncation radius has been determined assuming as typical velocity of cluster galaxies the 3D projection of the line of sight velocity dispersion of late-type systems. This is a good approximation which takes into account the fact that late-type galaxies have, on average, a velocity dispersion which is $\sigma_{LT} \simeq \sqrt{2} \times \sigma_{ET}$ ([Colless & Dunn 1996](#); [Biviano & Poggianti 2009](#)) typical of an infalling population. Infalling systems have radial orbits which make RPS much more efficient than circular orbits typical of the virialised early-type component since they bring the gas rich systems in the inner cluster regions with higher velocities. To take into account this effect, we can derive a more realistic distribution of ram pressure forces acting on a mix of star-forming galaxies using the orbital velocity parameters and positions obtained for $z = 0$ clusters in the simulated framework of semi-analytic models of galaxy formation. We use the model presented in [Henriques et al. \(2015\)](#) and based on the Millennium simulation ([Springel et al. 2005](#)). We select as clusters all haloes more massive than $M_{\text{cluster}} > 10^{14} M_{\odot}$ and the galaxy sample is made by satellites of these haloes with $M_{\text{star}} > 10^9 M_{\odot}$. The left panel of [Figure 4](#) shows the ram pressure force profile as a function of the three dimensional distance of each galaxy from the cluster centre (r) normalized to r_{200} . The median ram pressure force can increase by two orders of magnitude going from the virial radius to the inner core of the clusters, mostly due to the increase in local ICM density. When these profiles are compared to the typical gravitational restoring force at the effective radius for more ($M_{\text{star}} > 10^{10} M_{\odot}$, red lines) and less massive ($10^9 < M_{\text{star}} < 10^{10} M_{\odot}$, blue lines) galaxies, we find that on average only 1% of the massive galaxies are subject to a force barely able to strip them at the virial radius, while this fraction increases above 50% within $0.5 \times r_{200}$. Conversely, lower mass galaxies are efficiently stripped when they cross the virial radius and the stripping force is greater than the restoring force for more than 90% of them within half of the virial radius. We stress that these values are to be considered only as average quantities as they do not take into account local variations in the ICM density, the stellar and dark matter profile of galaxy discs, the presence of bulges, and the clumpiness of the cold gas components. The right panel of [Figure 4](#) shows the same ram pressure force but as a function of the projected distance of galaxies from the cluster centre on the plane of the sky (R_{proj}). This figure can thus directly be compared to the observations. With projected positions we notice a mild increase in the scatter of the ram pressure force distribution and a slightly steeper profile but the main trend remains unchanged.

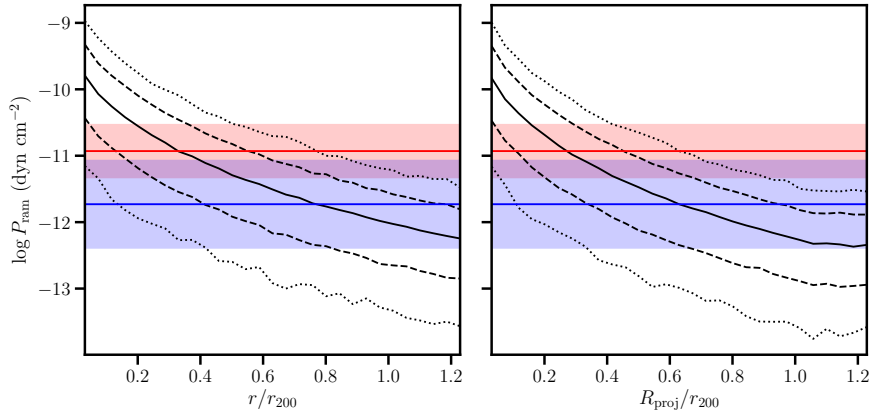


Fig. 4 The ram pressure force profile as a function of the 3D distance of each galaxy from the cluster centre normalized to r_{200} (Left panel) and as a function of the projected distance on the plane of the sky normalized to the same quantity (Right panel). The RPS force is obtained from the 3D peculiar velocity of each galaxy in the cluster multiplied by the ICM density at its position as derived from the equation given in the caption of Fig. 1. The solid black line marks the median ram pressure force profile, while the dashed and dotted lines mark the 10th, 90th and 1st, 99th percentiles, respectively. The red (blue) solid lines and the associated shaded areas show the average and 1σ dispersion of the gravitational restoring force (at the stellar effective radius) for galaxies with $M_{\text{star}} > 10^{10}M_{\odot}$ ($10^9 < M_{\text{star}} < 10^{10}M_{\odot}$), where $\langle \Sigma_{\text{star}} \rangle$ is derived using galaxies extracted from the Herschel Reference Survey as described in Boselli et al. (2014c) and $\langle \Sigma_{\text{gas}} \rangle$ from the VIVA sample (Chung et al. 2009a) both limited to those objects with a normal H I content. The gas surface density is derived assuming that $M_{\text{H}_2} = M_{\text{H I}}$ within the H I effective radius.

3 Observational evidence

3.1 Identification of the dominant perturbing mechanism

A critical aspect in environmental studies is the identification of the dominant perturbing mechanism on galaxies of different mass, in different high-density regions, and at different epochs. The main difference between gravitational perturbations and hydrodynamic interactions between the cold ISM of galaxies and the hot ICM of high-density regions is that while the former acts indistinctly on all galaxy components (gas, stars, dark matter...), the latter affects only the diffuse ISM (gas in all its phases, dust). Gravitational interactions are thus able to produce low surface brightness tidal tails in the stellar component, truncate stellar discs and induce gas infall in the nuclear regions because of their effect on the gravitational potential well of the perturbed galaxy, for instance through the formation of dynamical instabilities such as bars or spiral arms (see Fig. 5, e.g. Valluri 1993; Miwa & Noguchi 1998; Ellison et al. 2011; Skibba et al. 2012; Sellwood 2014). The stellar component is insensitive to hydrodynamic interactions which act only on the diffuse ISM. Asymmetries in the old smooth and diffuse stellar component such as tidal tails, shells, etc are

undoubted signs of an ongoing or a recent gravitational perturbation, while marked asymmetries only present in the different components of the ISM are clearly witnessing an hydrodynamic interaction (Fig. 5). Second order (minor) effects on the gravitational potential well of the perturbed galaxies can be produced once most of the ISM is displaced from the stellar disc, in particular in dwarf systems characterised by a shallow potential well and a large fraction of gas (e.g. [Boselli & Gavazzi 2014](#)). At the same time, new stars can be formed in the stripped gas, producing asymmetric, clumpy structures in the youngest stellar component.

It is harder to discriminate among the different hydrodynamic mechanisms since all of them act indiscriminately on the different diffuse phases of the ISM of galaxies⁷. RPS, laminar viscous and turbulent stripping via Kelvin-Helmholtz instabilities have very similar observational effects on the gaseous component of the ISM, removing it from the outer parts of the galactic disc where the gravitational potential well is not sufficient to overcome the external pressure exerted by the ICM on the galaxy moving at high velocity. The ISM is removed either by the external pressure or by the friction between the two media (ICM-ISM) once they get in contact during the crossing of the galaxy within the cluster. All these hydrodynamic mechanisms are related to the motion the galaxies within the ICM, and can thus be identified with dynamical signatures such as cometary tails in the gaseous component. Thermal evaporation occurs once the cold ISM ($T \leq 10^4$ K) gets in contact with the hot ICM ($T \sim 10^7$ - 10^8 K) ([Cowie & Songaila 1977](#)). The transfer of energy via electron heat conduction is able to make the cold gas evaporate and change to phases of higher temperatures. This mechanism is thus independent from the dynamic of the galaxy within the cluster, although its motion within the ICM grants a continuum supply of external energy. The identification of this mechanism is challenging since it would imply the direct observation of a changing of phase of the ISM along the disc and in the surrounding regions of the perturbed galaxies. Starvation or strangulation occurs once a galaxy enters within the halo of the high-density structure. As satellite of a larger halo, gas infall supplying fresh material to support star formation is stopped (e.g. [Larson et al. 1980](#)). The perturbed galaxies thus consume the available cold gas reservoir gradually and uniformly reducing on long timescales ($\tau \simeq 3$ - 4 Gyr; [Boselli et al. 2014c](#)) their star formation activity on the disc. Their stellar and gas radial profiles are very symmetric but systematically reduced with respect to those of similar unperturbed objects in the field, where the gas infall continue to sustain star formation at all galactocentric distances up to the present epoch (e.g. [Boselli et al. 2006](#)). Starvation is thus not able to produce the typical truncated gaseous discs observed in RPS galaxies (see Sec. 3.4). To summarise, the identification between gravitational and hydrodynamic perturbing mechanisms in high-density regions through the observation of individual objects is possible provided that high-quality, high-sensitivity multifrequency data are available.

⁷ As specified in Sec. 3.2.3, there are indications that clumpy structures such as giant molecular clouds decouple from the ram pressure wind

Hydrodynamic phenomena (RPS, Kelvin-Helmholtz and Rayleigh-Taylor instabilities, and viscous stripping) have very similar large scale observational signatures, and can only be disentangled whenever the perturbed regions at the interface between the cold ISM and the hot ICM are fully resolved with sufficient sensitivity (Roediger & Brüggen 2008; Roediger et al. 2013) as in Milky Way streams (Barger et al. 2020) or in a few large nearby galaxies⁸. We thus consider these different mechanism as different flavors of an hydrodynamic stripping process through this work, unless otherwise stated. They can be easily distinguished from starvation and thermal evaporation as mentioned above.

We recall, however, that all these mechanisms, gravitational and hydrodynamic, can act simultaneously on the gas-rich galaxies entering the cluster (e.g. Cortese et al. 2021). Their effect is additive, and can thus increase the efficiency in removing the gas and quenching the activity of star formation of the perturbed systems. What is interesting in this context is understanding which, among these mechanisms, is dominant in different environments, on different galaxy populations, and at different epochs, in order to pose strong observational constraints to models of galaxy evolution and cosmological simulations.

3.2 The presence of RPS tails

RPS has been first proposed to explain the nature of head-tail radio galaxies in nearby clusters (e.g. Miley et al. 1972; Miley 1980). In these peculiar objects, generally associated to the massive dominant early-type galaxies located deeply within the gravitational potential well of massive clusters, the radio jet is bent because of the pressure exerted by the ICM on the relativistic electrons escaping from the active nucleus during the motion of the parent galaxy within the cluster. Since then, several morphological features peculiar of an ongoing RPS event have been discovered at different wavelengths in a large variety of galaxies populating nearby clusters. Among these, the first evidence of an hydrodynamic interaction between the hot ICM and the cold ISM of late-type galaxies in rich environments has been gathered by Gavazzi (1978) in the radio continuum and claimed by Shostak et al. (1982) in HI. In RPS objects, the most unique and peculiar feature of the interaction are one-sided cometary tails of stripped ISM material combined with a normal and non-displaced stellar component, as now routinely observed in several nearby cluster galaxies. Since the first discoveries in radio observations, cometary tails without an associated evolved stellar component have been detected in the different gas phases (atomic, molecular, ionised, hot) and in the dust. It is worth

⁸ Kelvin-Helmholtz instabilities are due to the velocity difference across the interface between two fluids (e.g., Livio et al. 1980; Nulsen 1982; Mori & Burkert 2000). They manifest as small scales waves and vortexes as those observed in the atmosphere of Jupiter. Rayleigh-Taylor instabilities are due to the pressure of a light fluid pushing a heavy fluid, forming small scale spikes and bubbles at their interface (e.g., Roediger & Brüggen 2008)



Fig. 5 Upper panel: The pseudo-colour image of part of the Markarian chain in the Virgo cluster (from right to left NGC 4402 (top), M86 (bottom), NGC 4435 (top), and NGC 4438 (bottom)) obtained combining the CFHT MegaCam NGVS (Ferrarese et al. 2012) optical images with the VESTIGE (Boselli et al. 2018c) $H\alpha+[N II]$ narrow-band image. North is up, east left. The size of the image is of $\simeq 40' \times 20'$, corresponding to $190 \text{ kpc} \times 95 \text{ kpc}$ (projected scale) at the distance of the Virgo cluster. The diffuse red filamentary structures escaping from the galaxies is ionised gas (adapted from Boselli et al. (2018c)). The galaxy NGC 4438 in the upper left corner of the image shows extended filaments of ionised gas but also asymmetric extended features in the stellar continuum. These features are tidal tails formed after the gravitational interaction of the galaxy with M86 and NGC 4435 (e.g. Combes et al. 1988; Boselli et al. 2005; Kenney et al. 2008). Although the gas can be partly removed by ram pressure (Vollmer et al. 2009), the dominant perturbing mechanism is gravitational since able to act on the stellar component. Lower panel: The pseudo-colour image of NGC 4569 and IC 3583 in the Virgo cluster. The size of the image is of $\simeq 50' \times 25'$, corresponding to $250 \text{ kpc} \times 125 \text{ kpc}$ (projected scale) at the distance of the Virgo cluster. The diffuse red emission escaping from the galaxy in the western direction is ionised gas extending up to $\simeq 150 \text{ kpc}$ (projected distance from the stellar disc). The cometary shape of the gaseous component and the lack of any stellar counterpart indicate that the galaxy NGC 4569 is undergoing an RPS event (adapted from Boselli et al. (2016a)).

noting that galaxies with a tail but first identified by young and blue extraplanar asymmetric features outside their discs are sometimes called “jellyfish” galaxies, after this name has been first introduced by [Chung et al. \(2009a\)](#), [Bekki \(2009\)](#) and extensively used by [Smith et al. \(2010\)](#), [Ebeling et al. \(2014\)](#), and [Poggianti et al. \(2017b\)](#) (extraplanar features are sometimes also called “fireballs”, [Yoshida et al. 2008](#)). As described in more details in Sec. 3.3, this nomenclature can be misleading to indicate galaxies undergoing an RPS event. Indeed, asymmetric features observed in broad-band optical images are tracing the distribution of stars and it cannot be ruled out they are produced by gravitational perturbations rather than RPS. We thus caution in using these ambiguous definitions to identify galaxies clearly undergoing an RPS event, and rather encourage the reader to call these objects ram pressure stripped galaxies. When these terms are used hereafter we only report the identification given in the original papers, without solving the ambiguity raised above and therefore not necessarily referring to galaxies purely undergoing RPS.

3.2.1 Radio continuum

Tails in radio continuum are due to the synchrotron emission of the relativistic electrons of the cosmic rays spinning in weak magnetic field. In early-type galaxies these relativistic electrons are accelerated by the radio jet. In late-types they are accelerated in the supernovae remnants present within the star forming disc of the perturbed objects. They are swept away from the disc with the ISM during the interaction. Presence of radio continuum tails in late-type galaxies have been observed in the centimetre spectral domain in the nearby clusters A1367 ([Gavazzi 1978](#); [Gavazzi & Jaffe 1985, 1987](#); [Gavazzi et al. 1995](#)), Coma ([Miller et al. 2009](#); [Chen et al. 2020](#); [Lal 2020](#)), Virgo ([Vollmer et al. 2004a, 2007, 2010, 2013](#); [Crowl et al. 2005](#); [Chyży et al. 2007](#); [Kantharia et al. 2008](#)), Perseus ([Roberts et al. 2022](#)) and in other nearby clusters ([Poggianti et al. 2019b](#)) They are located within the inner regions of the cluster, up to $R/r_{200} \simeq 1.4$ in Coma ([Chen et al. 2020](#); [Roberts et al. 2021a](#)) and $R/r_{200} \simeq 0.6$ in A1367 ([Gavazzi et al. 1995](#)). There is also evidence of a radio continuum tail in a galaxy suffering an RPS episode within a nearby group ([Rasmussen et al. 2006](#)). Recently similar tails have been also observed in the metre spectral domain (144 MHz LOFAR data taken during the LoTSS survey) in a significant fraction of late type galaxies in several nearby clusters (including Coma and A1367) and in groups of mass $10^{12.5} < M_{\text{group}} < 10^{14} M_{\odot}$ up to one virial radius ([Botteon et al. 2020](#); [Roberts et al. 2021a,b](#)). It has been also observed that these objects have a radio-to-FIR ratio higher than similar objects in the field ([Gavazzi & Jaffe 1986](#); [Gavazzi et al. 1991](#); [Niklas et al. 1995](#); [Andersen & Owen 1995](#); [Rengarajan et al. 1997](#); [Gavazzi & Boselli 1999](#); [Miller & Owen 2001](#); [Reddy & Yun 2004](#); [Boselli & Gavazzi 2006](#); [Murphy et al. 2009](#); [Vollmer et al. 2010, 2013](#); [Chen et al. 2020](#)). This evidence, statistically shared also by the other late-type galaxies populating nearby clusters, has been first interpreted as due to the compression of the magnetic field frozen within the ISM during its hydrodynamic interaction with the ICM ([Gavazzi](#)

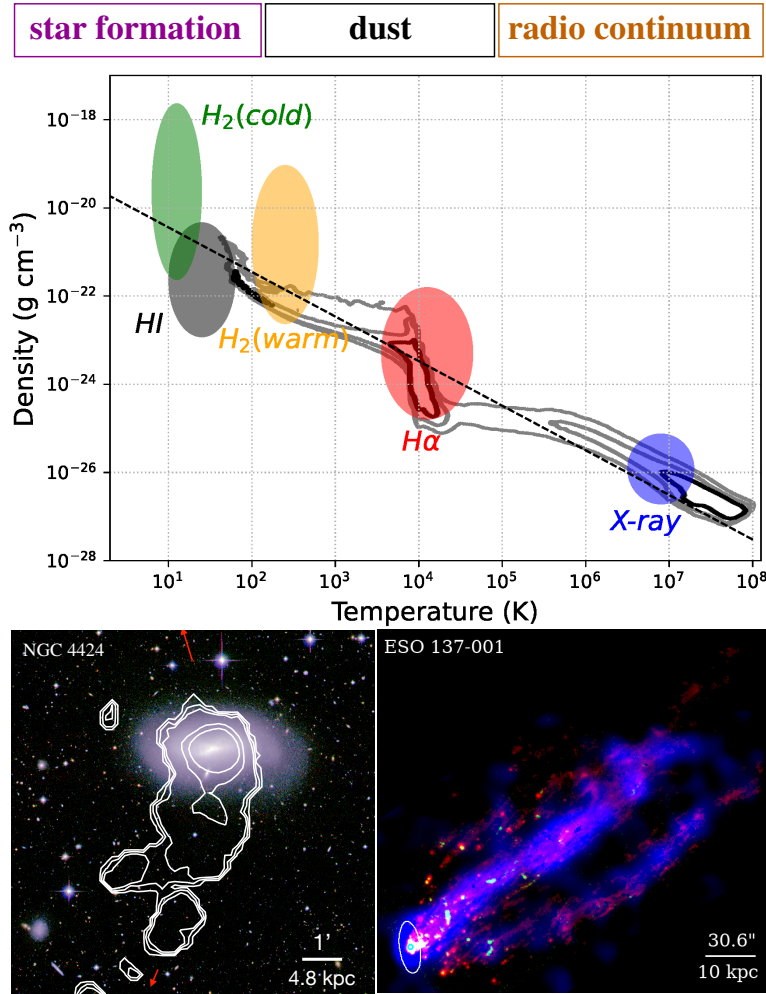


Fig. 6 Phase diagram for the gas in the stripped tails. Current data have revealed the existence of cold molecular gas (traced by CO), warm molecular gas (traced by H₂ lines and other lines with the NIR/MIR spectroscopy), cold atomic gas (H I), warm and ionized gas (H α and other optical emission lines) and hot gas traced by the X-ray emission. The grey contours are the gas phase diagram from simulations by Stephanie Tonnesen. The black dashed line shows the isobaric condition. While cold molecular and atomic gas are not included, the distribution peaks around $T \sim 10^{7.5}$ K and 10^4 K are clear, as well as the continuous distribution with temperature and density. Other potential tracers, already detected in X-ray cool cores and/or galactic winds, include coronal lines like [C IV] and [O VI] to trace $T = 10^5 - 10^6$ K gas, ro-vibrational H₂ lines at the NIR to trace hot molecular gas at $T \sim 10^3$ K and FIR lines like [C II] to trace cold gas. We include examples for most gas phases: ESO 137-001 for CO from ALMA (green), H α from MUSE (red) and X-ray from Chandra (blue) (from Sun et al. 2022), and NGC 4424 for H I (white contours, from Chung et al. 2009a) on the optical image. Warm molecular gas was also detected in ESO 137-001 (Sivanandam et al. 2010), as well as H I from MeerKAT (Ramatsoku, private communication). We also list other components detected in stripped tails, young stars recently formed, dust and radio continuum indicative of the existence of relativistic electrons and likely CRs.

et al. 1991; Völk & Xu 1994; Boselli & Gavazzi 2006). The synchrotron radio emissivity $\epsilon_{\text{syn}}(\nu)$ at a frequency ν is proportional to the magnetic field B as (Rybicki & Lightman 1979):

$$\epsilon_{\text{syn}}(\nu) \propto n_e B^{\alpha_{\text{syn}}+1} \nu^{-\alpha_{\text{syn}}} \quad [\text{erg s}^{-1} \text{cm}^{-3} \text{sr}^{-1} \text{Hz}^{-1}] \quad (30)$$

where n_e is the density of relativistic electrons accelerated in the supernovae remnants and α_{syn} the nonthermal synchrotron spectral index, which in late-type galaxies has a typical value of $\alpha_{\text{syn}} \simeq 0.8$ at ~ 1.4 GHz (Gioia et al. 1982; Tabatabaei et al. 2017; Chyży et al. 2018). Since both the density of relativistic electrons and the far-IR emission are tightly related to the star formation activity of galaxies, as suggested by the very low dispersion observed in the FIR-radio correlation of unperturbed systems (de Jong et al. 1985; Helou et al. 1985), the observed increase in the radio-to-FIR ratio of cluster galaxies ($\simeq 4$ -10) can be explained by an increase of the magnetic field of a factor of ~ 2 -3. More recently, tuned modifications of this mechanism have been proposed to explain the increased radio continuum emissivity of cluster galaxies (enhancement of the magnetic field strength caused by the ISM shear motion (Murphy et al. 2009), compression of the ISM/magnetic field by the external ICM hydrodynamical and/or thermal pressure (Murphy et al. 2009), and turbulence and ICM shocks caused by ram pressure (Völk & Xu 1994; Kang & Ryu 2011)). A local compression of the magnetic field in the leading edge of ram pressure stripped galaxies has been observed thanks to polarised data in a few galaxies in the Virgo cluster (Vollmer et al. 2010, 2013).

Comparing resolved far-IR Spitzer and radio continuum VLA images of Virgo cluster galaxies, Murphy et al. (2009) discovered the presence of radio deficient regions in the outer discs or RPS galaxies. These radio-deficient regions seem to be situated just outside regions with an high radio polarisation and a flat spectral index, at the leading edge of the galaxy disc interacting with the surrounding ICM. This signature has been explained as due to a sweeping of the cosmic ray electrons and of the associated magnetic field on the leading side of the disc where gas has been removed during the interaction, a compression of the magnetic field at the edges of the ISM-ICM interface, with a re-acceleration of the cosmic rays able to enhance the global radio emissivity of the perturbed galaxies Murphy et al. (2009).

The properties of these radio continuum tails can be used to derive interesting parameters necessary to constrain models and simulations. The synchrotron emission timescale is given by the relation (Feretti & Giovannini 2008):

$$\tau_{\text{syn}} = 4.5 \times 10^7 \left(\frac{B}{10 \mu\text{G}} \right)^{-3/2} \nu_{\text{GHz}}^{-1/2} \quad [\text{yr}] \quad (31)$$

The deprojected physical length of the radio continuum tail measured from the observations can be used to derive a typical timescale for the motion of the galaxy within the cluster and thus infer an estimate of the magnetic field intensity within the tail (e.g. Vollmer et al. 2021; Chen et al. 2020). This number can

be used as input to models and simulations now able to quantify the impact of magnetic fields on the stripped material (Tonnesen & Stone 2014; Ruszkowski et al. 2014; Shin & Ruszkowski 2014). This estimate of the magnetic field in the radio continuum tail, however, can be done only in the hypothesis that the stripped electrons are neither re-accelerated nor produced within the tail. This might indeed be the case. Regions of recent star formation in the stripped gas, although not ubiquitous (see Sec. 5.1.3), have been observed in several galaxies with tails in the ionised gas component such as ESO137-001 in the Norma cluster (Sun et al. 2007a, 2010; Fossati et al. 2016), in most of the jellyfish galaxies of the GASP survey (Poggianti et al. 2017b) the contribution of star forming regions can be roughly quantified by comparing the star formation rate derived from the radio continuum emission to that determined using the ionised gas emission by means of standard calibrators such as those proposed by Kennicutt (1998) (see Chen et al. 2020 for an example). At the same time, the electrons can be re-accelerated within the tail by turbulence and shocks produced during the RPS phenomenon (Kang & Ryu 2011; Pinzke et al. 2013). If the radio spectral index and the volume of the emitting tail are known, the strength of the magnetic field within the tail of stripped gas can be inferred using the classical equipartition or minimum-energy estimates as suggested by Beck & Krause (2005). A recent example of magnetic field estimated in a single RPS tail can be found in Ignesti et al. (2022).

It is also worth mentioning that the spectral slope of the radio continuum spectrum steepens with the age of the cosmic ray electrons. As indicated by Vollmer et al. (2021), for a purely aging population of cosmic ray electrons the evolution of flux density is given by:

$$f(t) = f_0 \times e^{-t/\tau_{\text{syn}}} \quad (32)$$

If we define the spectral index α as:

$$\alpha = \frac{\ln(f_1/f_2)}{\ln(\nu_1/\nu_2)} \quad (33)$$

where f_1 , f_2 , ν_1 , and ν_2 are the flux densities (or surface brightnesses) and the frequencies in the two bands, the timescale needed to steepen the spectra index from an initial value α_{in} to a final value α_{end} is given by the relation:

$$\tau_{\text{SI}} = \frac{(\alpha_{\text{in}} - \alpha_{\text{end}}) \ln(\nu_1/\nu_2)}{1/\tau_{\text{syn},1} - 1/\tau_{\text{syn},2}} \quad (34)$$

A steepening of the spectrum should thus be observed with increasing distance from the galaxy (e.g. NGC 4522, Vollmer et al. 2004b).

3.2.2 Atomic gas

The first observation of a nearby galaxy with a HI cometary tail is probably NGC 1961 in a nearby group (Shostak et al. 1982). The asymmetric HI gas distribution of this galaxy was explained as due to an ongoing RPS event, but

this interpretation has been later questioned given the lack of hot X-ray emitting gas in the associate group environment (Combes et al. 2009; Anderson & Sunyaev 2016). Since then, targeted or blind surveys done using interferometric observations revealed the presence of several galaxies with long tails of cold atomic hydrogen without any associated optical counterpart up to $R/r_{200} \simeq 1$ in the Virgo cluster (Kenney et al. 2004; Chung et al. 2007; Sorgho et al. 2017; Minchin et al. 2019), $R/r_{200} \simeq 0.5$ in the Coma cluster (Gavazzi 1989; Bravo-Alfaro et al. 2001; Healy et al. 2021), $R/r_{200} \simeq 0.6$ in A1367 (Gavazzi 1989; Dickey & Gavazzi 1991; Scott et al. 2010), where also a couple of objects suffering the joint effect of ram pressure and harassment have been detected well outside the virial radius ($R/r_{200} \simeq 1.6-2.2$; Scott et al. (2012)), and in a few other nearby clusters and groups (e.g. Dickey 1997; Serra et al. 2013; Lee & Chung 2018; Ramatsoku et al. 2019; Deb et al. 2020; Ramatsoku et al. 2020; Reynolds et al. 2020; Loni et al. 2021; Wang et al. 2021). The number of objects with tails of H I gas, however, is still relatively limited. In Virgo, for instance, where the proximity of the cluster (16.5 Mpc) ideally combines the sensitivity and the angular resolution needed to detect these low column density features, they are detected in only seven galaxies out of the 53 mapped during the VIVA survey (Chung et al. 2007, 2009a). This relatively low fraction ($\sim 15\%$) can be due to different factors: i) a still limited sensitivity of radio observations of low column density extended structures, ii) RPS being not dominant in the Virgo cluster, and iii) a change in the gas phase once stripped from the galaxy, making the H I cometary tails as short lived structures. Point i) is probably the case for clusters located at distances of ≥ 100 Mpc, where the required sensitivity is only reached in detriment of the angular resolution. Hopefully, the most recent generation of instruments such as ASKAP and MeerKAT, or the future ambitious projects such as SKA, will further extend our capability to detect these low column density features in clusters other than Virgo and Fornax. Very promising results, although based on stacking of large samples, are coming from the H I survey of the Coma cluster done with the WSRT (Healy et al. 2021), while direct detections of several late-type systems with extended H I tails at column densities of $\Sigma_{\text{HI}} \sim 10^{18} \text{ cm}^{-2}$ have been obtained in Fornax with the sensitive MeerKAT telescope (Serra, private communication). Concerning point ii), there is indeed evidence that a few galaxies with extended tails of H I gas have also suffered gravitational perturbations (e.g. NGC 4254, Haynes et al. 2007; Duc & Bournaud 2008; Vollmer et al. 2005b; Boselli et al. 2018b; NGC 4424, Sorgho et al. 2017; Boselli et al. 2018a; NGC 4654, Vollmer 2003; Lizée et al. 2021). This is also the case for the newly detected galaxies with tails in H I, which often have perturbed morphologies suggesting a combined effect of ram pressure and harassment as discussed in more details in Section 3.3. iii) Similarly, we cannot rule out the heating of the cold gas, since a growing number of tails are being detected in multiple gas phases as described in Section 5. This indicates that H I tails are a short lived phenomenon witnessing an ongoing process (while the presence of truncated H I discs are rather a proof of a past RPS event, see Sec. 3.4).

3.2.3 Molecular gas

The hydrodynamic pressure exerted by the hot ICM acts regardless on all the different components of the ISM of galaxies moving at high velocity within the gravitational potential well of the high density structure. Models and simulations consistently suggests that the stripping efficiency is less severe on the molecular gas than on the diffuse H I since H₂ is mainly located within dense giant molecular clouds which have a relatively small cross-section (10 pc) with respect to the diffuse atomic gas ($\simeq 100\text{-}500$ pc), they are much denser ($n(\text{H}_2) \simeq 50\text{-}500 \text{ cm}^{-3}$, Solomon et al. (e.g. 1987); Engargiola et al. (e.g. 2003); Bolatto et al. (e.g. 2008), vs. $n(\text{HI}) \simeq 0.1\text{-}1 \text{ cm}^{-3}$), and are located deeper within the stellar disc where gravitational forces are strong (e.g. Yamagami & Fujita 2011). However, the ISM is turbulent and clumpy, and overdensities are constantly created and destroyed. It is thus conceivable that the diffuse molecular gas can be stripped during the interaction, and thus that the dense molecular gas within giant molecular cloud also decreases because not replenished by the diffuse component (Tonnesen & Bryan 2009). Simulations indicate that most of the molecular gas is removed from the outer disc (Lee et al. 2020).

Direct observational evidence of molecular gas stripping via ram pressure is still very limited not only because of the reasons mentioned above, but also because of the lack of high sensitivity panoramic detectors with a wide field of view in the mm and sub-mm spectral domain, where molecular gas is generally looked for through the detection of the main ¹²CO(1-0) (2.6 mm, 115 GHz) and ¹²CO(2-1) (1.3 mm, 230 GHz) emission lines. CO observations of late-type cluster galaxies characterised by extended tails at other frequencies revealed molecular gas to be present in the tails. The first of these evidences have been found in ESO137-001 in the Norma cluster (Jáchym et al. 2014), in NGC 4388 in Virgo by (Verdugo et al. 2015), and in D100 in the Coma cluster Jáchym et al. (2017). While in ESO137-001 and in D100 very large amounts of molecular gas ($\simeq 10^9 M_\odot$) have been detected up to $\sim 40\text{-}60$ kpc from the galaxy disc, in NGC 4388 a small amount of gas ($\simeq 10^6 M_\odot$) has been detected in well defined regions associated with star forming blobs. More recently, clearer evidences of molecular gas stripping come from the detection of extended tails in CO observed in several late-type galaxies in the Fornax cluster (Zabel et al. 2019), a high spatial resolution map of ESO137-001 with ALMA (Jáchym et al. 2019), and an extraplanar plume of molecular gas ~ 1 kpc wide and ~ 2 kpc above the stellar disc of NGC 4402 in Virgo associated to dusty filaments seen in absorption in the HST images, kinematically dissociated from the disc (Cramer et al. 2020). A further example in the Virgo cluster is NGC 4438, where molecular gas has been removed from the inner regions (Combes et al. 1988), although this galaxy is mainly suffering a gravitational perturbation (Vollmer et al. 2005a, 2009). A few other cases of CO detections are galaxies from the GASP sample located in clusters further away (Moretti et al. 2018, 2020b). While in the case of ESO137-001 and D100 the molecular gas is dominant in mass in the stripped tails the Virgo examples show a smaller molecular fraction. Moreover many ionised gas tails in Virgo

galaxies have not been detected in CO. It is therefore still unclear what drives the fraction of molecular gas in the stripped ISM and if these variations are due to molecular cloud formation in-situ, to the stripping conditions near the galaxy disc, or to the ICM pressure as suggested by [Tonnesen & Bryan \(2012\)](#). Milder evidence such as asymmetric molecular line profiles or CO gas distributions in the outer regions of known perturbed galaxies or other kinematical disturbances has been also searched for in several galaxies in the Virgo ([Kennedy et al. 1990](#); [Vollmer et al. 1999, 2001a, 2008a, 2012](#); [Cortés et al. 2006](#); [Jáchym et al. 2013](#); [Lee et al. 2017](#)) and A1367 ([Boselli et al. 1995](#); [Scott et al. 2013, 2015](#)) clusters. Among these, it is worth noticing the galaxy NGC 4522 in Virgo, where $^{13}\text{CO}(1-0)$ has been detected in a few H II regions located outside the stellar disc, suggesting that heavy elements produced in evolved stars at the origin of the ^{13}C of the ISM can be stripped from the stellar disc during a ram pressure episode ([Lee & Chung 2018](#)).

The tails of a few galaxies in RPS have been observed with *Spitzer* in imaging and spectroscopic mode. These observations revealed the presence of large amounts ($M_{\text{H}_2} = 10^6\text{-}10^8 M_{\odot}$ and column densities $\Sigma_{\text{H}_2} = 10^{19}\text{-}10^{20} \text{ cm}^{-3}$) of warm ($T = 115\text{-}160 \text{ K}$) and smaller amounts ($\simeq 1\%$ of the warm component) of hot ($T = 400\text{-}600 \text{ K}$) molecular gas ([Sivanandam et al. 2010, 2014](#)). The large amount of warm molecular gas observed in these tails with respect to what generally observed in star forming regions has been interpreted as due to the presence of gas shock-heated during the hydrodynamic interaction with the ICM, consistently with a picture where the cold stripped gas is heated and changes phase once stripped from the galaxy. Similar *Spitzer* observations of the leading side of galaxies suffering an RPS event revealed an excess of the warm H_2/PAH ratio with respect to what observed in the disc of unperturbed star forming systems. This excess of warm H_2 emission has been attributed to the contribution of shock-excited molecular hydrogen triggered during the interaction ([Wong et al. 2014](#)).

3.2.4 Ionised gas

The first evidence of diffuse tails of ionised gas in ram pressure stripped galaxies has been gathered after the observations of two peculiar objects in the cluster A1367 with extended tails in radio continuum ([Gavazzi et al. 2001a](#)). These observations have been carried out through very deep exposures on 2m class telescopes using narrow-band (NB, $\sim 100 \text{ \AA}$ wide) interferential filters centered on the emission of the redshifted $\text{H}\alpha$ Balmer line. The advent of large panoramic detectors coupled with high-transmissivity NB filters at larger 4m and 8m class telescopes opened a new era in the observation of nearby clusters. Since the discovery of ([Gavazzi et al. 2001a](#)), the detection of diffuse tails of ionised gas without any associated stellar component witnessing ongoing RPS events significantly increased. These tails are now commonly detected in most of the nearby clusters such as Virgo ([Yoshida et al. 2002](#); [Boselli et al. 2016a, 2018a](#); [Fossati et al. 2018](#)), Coma ([Yagi et al. 2007, 2010](#); [Fossati et al. 2012](#); [Yoshida et al. 2012](#); [Gavazzi et al. 2018b](#)), A1367 ([Gavazzi et al. 2001a](#); [Yagi](#)

et al. 2017), and Norma (Sun et al. 2007a, 2010) and have been detected using this technique in clusters up to $z \sim 0.4$ (Yagi et al. 2015). One of the most spectacular cases is NGC 4569 in the Virgo cluster, shown in Fig. 5. Ionised gas tails have been also observed in broad-band selected perturbed galaxies in $0.04 \lesssim z \lesssim 0.07$ clusters by Poggianti et al. (2017b) as part of the GASP survey. They have been also predicted by wind-tunnel hydrodynamic simulations, although their physical properties (density, size, clumpiness etc) significantly change according to the adopted simulation and the details of the radiative cooling recipes implemented (Kronberger et al. 2008a; Kapferer et al. 2009; Tonnesen & Bryan 2010). These ionised gas tails extend up to 100 kpc in projected distance from their parent galaxies, and have $H\alpha$ surface brightnesses of the order of $\Sigma_{H\alpha} \simeq 1\text{--}5 \times 10^{-18} \text{ erg s}^{-1} \text{ cm}^{-2} \text{ arcsec}^{-2}$. The blind surveys of nearby clusters carried out so far, unfortunately only partially homogeneous and complete, consistently suggest that the frequency of galaxies showing extended diffuse structures in ionised gas is very high, reaching $\simeq 50\%$ in the late-type systems (Boselli & Gavazzi 2014; Gavazzi et al. 2018b), making at present narrow-band imaging one of the most efficient observational techniques to identify galaxies undergoing a perturbation. The ongoing deep blind surveys of nearby clusters such as VESTIGE (A Virgo Environmental Survey Tracing Ionised Gas Emission, Boselli et al. 2018c), thanks to their excellent sensitivity and image quality, have been designed to accurately quantify on strong statistical basis the fraction of galaxies undergoing the different perturbing mechanisms in a typical cluster environment. The detailed study of the physical and kinematical properties of the stripped gas, which are necessary to understand the nature of the underlying perturbing mechanism, might however require targeted spectroscopic observations, mostly obtained with single- or multi-object slits (Yoshida et al. 2004, 2012; Yagi et al. 2013; Boselli et al. 2016b; Fossati et al. 2018). Most recently, however, new IFU spectrographs with large fields of view coupled with 4-8m class telescopes such as MUSE at the VLT have provided us with resolved spectroscopic observations. These datasets are by far the most information rich, allowing a detailed study of the metal content and ionisation conditions of the stripped gas (Merluzzi et al. 2013; Fumagalli et al. 2014; Fossati et al. 2016, 2019; Consolandi et al. 2017; Poggianti et al. 2017b, 2019a; Gullieuszik et al. 2017; Boselli et al. 2018a; Vulcani et al. 2018; Bellhouse et al. 2019; Liu et al. 2021). These instruments are also extremely efficient in detecting tails of ionised gas at higher redshift, where the field of view of the instrument ($\sim 1 \text{ arcmin}^2$) is sufficient to cover a large fraction of the cluster virial radius, while the large wavelength coverage allows a detection of at least one strong emission line over a wide redshift range. RPS tails of ionised gas have indeed been detected through the $[OII]\lambda 3727 \text{ \AA}$ emission line in two cluster galaxies at $z \sim 0.7$ by Boselli et al. (2019a).

The $H\alpha$ ($\lambda = 6563 \text{ \AA}$) emission line, which is mostly used to detect extended ionised gas features associated to perturbed cluster galaxies, is due to the recombination of hydrogen which has an ionisation energy of 13.6 eV and thus traces the distribution of gas at a typical temperature of $T \simeq 10^4 \text{ K}$ (Osterbrock & Ferland 2006). In the case that the tails are detected in other

emission lines, the ionised gas temperature can be estimated from the ionisation energy of these lines. However, a robust estimate of the gas temperature hinges on the detection of faint lines to build temperature sensitive line ratios (e.g. $[\text{NII}]\lambda\lambda 6584,6548/[\text{NII}]\lambda 5755$, [Fossati et al. 2016](#)).

Within the disc of late-type galaxies hydrogen is mainly ionised by the UV radiation emitted by young (age ≤ 10 Myr) and massive ($M_{\text{star}} \geq 10 M_{\odot}$) O-early B type stars and is thus an excellent tracer of star formation ([Kennicutt 1998](#); [Boselli et al. 2009](#)). In the diffuse tails, where star formation is not always present, the atomic hydrogen stripped during the interaction and mixed within the hot ICM can be ionised by several other mechanisms such as shocks in the turbulent gas, heat conduction, and magneto hydrodynamic waves (e.g. [Ferland et al. 2009](#); [Fossati et al. 2016](#); [Boselli et al. 2016a](#)). In massive galaxies which host an AGN, such as NGC 4388 in Virgo, the diffuse gas can also be ionised by the powerful nuclear source ([Yoshida et al. 2004](#)). Filamentary structures such as those seen in the tails NGC 4330 in Virgo ([Fossati et al. 2018](#)), reproduced by the most recent hydrodynamic simulations, suggests that magnetic field might also play an important role in keeping the stripped gas in unmixed filamentary structures in the tail ([Tonnesen & Stone 2014](#); [Ruszkowski et al. 2014](#)). The same simulations also indicate that magnetic fields contribute to keep the stripped gas confined within extended tails without significantly affecting the stripping rate from the disc. Large scale magnetic fields aligned along the tail of stripped gas have been measured using polarised radio observations in the jellyfish galaxy JO206 by [Müller et al. \(2021\)](#).

The large number of $\text{H}\alpha$ extended tails observed so far in nearby clusters allows us to have a clear view of the variety of possible configurations produced during the interaction between the cold ISM of freshly-infalling gas-rich galaxies with the surrounding ICM. In most of the observed cases, the diffuse tails include compact regions where star formation is taking place. Very deep narrow band imaging suggest that even in the most extreme cases dominated by compact H II regions such as IC 3418 (VCC 1217) in Virgo ([Hester et al. 2010](#); [Fumagalli et al. 2011](#); [Kenney et al. 2014](#)), a diffuse component is also present ([Sun et al. in prep.](#)). There are, however, a few galaxies such as NGC 4569 ([Boselli et al. 2016a](#)) in the Virgo cluster and CGCG 097-073 and 097-079 in A1367 ([Pedrini et al. 2022](#)) where star formation is not present in the stripped gas.

The data derived from narrow-band imaging observations, once corrected for $[\text{NII}]$ contamination ($[\text{NII}]/\text{H}\alpha \sim 0.5$, [Boselli et al. 2016a](#); [Poggianti et al. 2019a](#)) and dust attenuation (expected to be low in these environments), and IFU data can be used to derive several physical properties of the ionised gas tails. First of all $\text{H}\alpha$ luminosities can be used to estimate mean ionised gas densities as in [Fossati et al. \(2016\)](#) and [Boselli et al. \(2016a\)](#) making simple assumption on the geometrical distribution of the gas and on the filling factor. Indeed, the $\text{H}\alpha$ luminosity of the gas is given by the relation ([Osterbrock & Ferland 2006](#)):

$$L(\text{H}\alpha) = n_e n_p \alpha_{\text{H}\alpha}^{\text{eff}} V f h \nu_{\text{H}\alpha} \quad (35)$$

where n_e and n_p are the number density of electrons and protons ($n_e \simeq n_p$), $\alpha_{\text{H}\alpha}^{\text{eff}}$ is the H α effective recombination coefficient ($\alpha_{\text{H}\alpha}^{\text{eff}} = 1.17 \times 10^{-13} \text{ cm}^3 \text{ s}^{-1}$), V is the volume of the emitting region, f the filling factor, h the Planck's constant, and $\nu_{\text{H}\alpha}$ the frequency of the H α transition. This leads to:

$$n_e = \sqrt{\frac{L(\text{H}\alpha)}{\alpha_{\text{H}\alpha}^{\text{eff}} V f h \nu_{\text{H}\alpha}}} \quad (36)$$

with typical values of $n_e \simeq 10^{-2} \text{ cm}^{-3}$, and total masses of ionised gas in the tail of:

$$M_{\text{ionised}} = V f n_e \quad (37)$$

of several $10^8 M_{\odot}$ for $f = 0.1$ and tails ~ 100 kpc long, thus comparable to those of the cold atomic hydrogen which is lacking from the perturbed galaxies, as suggested by H I observations and tuned models or simulations (e.g. [Boselli et al. 2016a](#)). It is worth noticing that these gas densities, although very uncertain because of the huge uncertainties on the geometrical distribution of the gas and on the filling factor, are very low, and can be hardly compared to those derived using standard optical line ratio diagnostics ([SII] λ 6716/6731 Å, [OII] λ 3729/3726 Å) since these tracers are degenerate when $n_e \leq 10 \text{ cm}^{-3}$ ([Osterbrock & Ferland 2006](#)). Infrared line diagnostics such as [NII] λ 205/122 μm , sensitive to lower electron densities ([Kewley et al. 2019](#)), should be used to confirm the low gas density within the tail. The gas density can also be used to estimate the typical hydrogen recombination timescale:

$$\tau_{\text{rec}} = \frac{1}{n_e \alpha_A} \quad (38)$$

where α_A is the total recombination coefficient ($\alpha_A = 4.2 \times 10^{-13} \text{ cm}^3 \text{ s}^{-1}$; [Osterbrock & Ferland 2006](#)). For a typical density of $n_e \simeq 10^{-2} \text{ cm}^{-3}$, the recombination time is $\tau_{\text{rec}} \simeq 8$ Myr, a short time when compared to the galaxy travel time that can produce a tail $\simeq 50$ kpc long (30 Myr). Indeed, several observations (e.g. [Chung et al. 2007](#)) suggest that the gas can even be stripped as H I, being further heated up to the ionised phase when in the tail. While some of the energy input could come from the UV radiation produced by H II regions in the tail, at the edges of the stripped disc, or from a powerful AGN radiation field, the fact that we detect ionised gas also in poorly star forming galaxies suggests that additional energy sources are shocks, ICM heat conduction or MHD waves ([Merluzzi et al. 2013](#); [Fossati et al. 2016](#); [Boselli et al. 2016a](#)), once again supporting the scenario where cold gas can change phase once stripped from the galaxy disc.

3.2.5 Hot gas

Tails of ram pressure stripped gas have also been searched for and detected in the hot ($T \sim 10^7$ K) gas emitting in X-rays. As massive early-type galaxies are typically rich on X-ray gas, many examples of X-ray stripped tails behind cluster early-type galaxies have been found (e.g., Machacek et al. 2006; Sun et al. 2007b; Randall et al. 2008; Wood et al. 2017, and references/citations therein). Even cluster early-type galaxies are beyond the scope of this paper, the physical processes related to their X-ray tails are often the same as or similar to those related to X-ray tails of cluster late-type galaxies. Since X-ray emission from cluster early-type galaxies and their tails is typically more luminous than that of cluster late-type galaxies, their studies offer important clues to our understanding of the X-ray tails behind cluster late-type galaxies, including constraints on the ICM transport processes (i.e., viscous diffusion and heat conduction). It is now known that: 1) the most significant observational signature is the contact discontinuity (or cold front) separating the galactic medium and the ICM (e.g., Zuhone & Roediger 2016). While a shock front is expected ahead of the contact discontinuity for galaxies moving supersonically, such a shock front has never been robustly detected in X-rays for galactic halos as the Mach number is typically not large (e.g., less than 1% of cluster galaxies with a Mach number of > 3 , Faltenbacher et al. 2005) and the emission enhancement on the galaxy scale (~ 10 kpc) has to be projected on the ICM emission on the cluster scale (~ 1 Mpc) along the line of sight. 2) For cold fronts and X-ray halos of cluster early-type galaxies with the best data, it is concluded that both viscosity and heat conductivity have been suppressed by at least a factor of 20 - 100 relative to the isotropic Spitzer values (e.g., Markevitch & Vikhlinin 2007; Sun et al. 2007b; Su et al. 2017; Ichinohe et al. 2017; Kraft et al. 2017). Efficient mixing in stripped tails and at small scales of cold fronts, likely from Kelvin-Helmholtz instabilities, has been observed. 3) Magnetic field in both the ICM and the ISM can have a significant impact on the properties of the X-ray tails (e.g., Shin & Ruszkowski 2014; Vijayaraghavan & Ricker 2017). 4) The actual galaxy trajectory and the ICM wind history can play important roles to shape the properties of the X-ray tails (e.g., Sheardown et al. 2019).

Compared with X-ray tails behind cluster early-type galaxies, X-ray tails behind cluster late-type galaxies bear several important differences: 1) Their X-ray tails typically co-exist with cooler gas while the tails of cluster early-type galaxies are single phase, hot gas removed from the galaxy. 2) While X-ray tails have been found behind late-type galaxies as faint as $\sim 0.15 L_*$ galaxies (e.g., D100 and CGCG 097-079, Sun et al. 2022), X-ray tails of cluster early-type galaxies are only observed in massive galaxies (e.g., $L > L_*$) with abundant X-ray emitting gas in the galaxy. 3) While X-ray tails of cluster late-type galaxies are typically fainter than their counterparts behind cluster early-type galaxies, they are often more luminous than their host galaxies in X-rays (Sun et al. 2022), while that is seldom the case for cluster early-type galaxies. 4) With potentially abundant cold gas in the stripped tails of

cluster late-type galaxies, the full evaporation of the stripped ISM can be slow, especially if the stripped cold clouds can grow when the radiative cooling in the mixing layers is strong (e.g. Gronke & Oh 2018; Sparre et al. 2020). On the other hand, radiative cooling is never strong in the X-ray tails behind cluster early-type galaxies.⁹ Thus, one may expect fast evaporation in tails behind cluster early-type galaxies. This would result in longer X-ray tails (relative to the galaxy size) behind cluster late-type galaxies than those behind cluster early-type objects. 5) High-mass X-ray binaries and even ultraluminous X-ray sources can be found in tails of cluster late-type galaxies (Sun et al. 2006, 2010; Poggianti et al. 2019a), while only low-mass X-ray binaries are detected in early-type galaxies but none in their hot gaseous tails.

Detections of X-ray tails behind cluster late-type galaxies require the sensitivity of Chandra and XMM-Newton. The first possible candidate is the galaxy C153 in the cluster A2125 at $z=0.253$ (Wang et al. 2004). While its X-ray tail is faint (for its distance) and not unambiguous, the UV trail and the [O II] tail of the galaxy are significant (Owen et al. 2006). With the Chandra data, Sun & Vikhlinin (2005) presented the discovery of an X-ray tail behind UGC 6697, a starburst galaxy that was known to host tails in the radio continuum and H α (Gavazzi 1978; Gavazzi et al. 2001a) in A1367. The XMM-Newton data show that the X-ray tail extends to at least 120 kpc from the nucleus (Ge et al. 2019; Sun et al. 2022). An X-ray tail was also observed behind the giant spiral NGC 6872 in the 0.5 keV Pavo group (Machacek et al. 2005), but it is uncertain how it was formed as the tail terminates on the dominant early-type galaxy of the group and the tail appears hotter than the group gas. Evidence of a short X-ray tail formed after an RPS process has also been found for the starburst galaxy NGC 2276 in the NGC 2300 group (Rasmussen et al. 2006).

By far the brightest X-ray tail behind a cluster late-type galaxy is ESO 137-001 (Sun et al. 2006, 2010) in the Norma cluster (A3627). Its X-ray tail, revealed from both Chandra and XMM-Newton, is bifurcated and extended to at least 80 kpc in projected distance from the nucleus. Six X-ray point sources as candidates of intracluster ultra-luminous X-ray sources were also detected. ESO 137-001 has then become the RPS galaxy with the most extensive multi-wavelength coverage, with the stripped tail detected in X-rays, H α , FIR emission of dust, warm H $_2$ (from MIR), cold molecular gas, H I and radio continuum (Sun et al. 2010; Fumagalli et al. 2014; Fossati et al. 2016; Sivanandam et al. 2010; Jáchym et al. 2014, 2019, Ramatsoku et al. private communication). It is also the only RPS galaxy in the GTO program of JWST. The Norma cluster also hosts another narrow X-ray tail behind ESO 137-002 (Sun et al. 2010; Zhang et al. 2013), with the X-ray emission detected to at least 40 kpc from the nucleus.

Candidates of X-ray tails in the closest Virgo cluster were reported behind NGC 4388 and NGC 4501 (Weżgowiec et al. 2011), while the analysis by Gu et al. (2013) also suggested a soft X-ray tail behind NGC 4388, positionally

⁹ For example, the radiative cooling time is 1.3 - 7.2 Gyr for several tail regions in NGC 4552's X-ray tail beyond the galaxy, with the X-ray gas properties derived by Kraft et al. (2017).

coincident with its HI tail discovered by Oosterloo & van Gorkom (2005). Gu et al. (2013) also presented the evidence of excess X-ray absorption in the NGC 4388's tail on the background bright M86 emission, likely originated from the extra HI absorption column in NGC 4388's tail. A wide X-ray tail was also detected behind the most massive spiral in the Virgo cluster, NGC 4569 (Boselli et al. 2016a; Sun et al. 2022).

Another spectacular example of X-ray tails in a rich cluster is the galaxy D100 in Coma (Sanders et al. 2014), which was first discovered in H α (Yagi et al. 2007, 2010). It has quickly become another RPS tail with rich multi-wavelength data for detailed studies (Jáchym et al. 2017; Cramer et al. 2019). The GASP survey has reported two X-ray tails, IC 5337 in A2626 (Poggianti et al. 2019a) and KAZ 364 (or JO201) in A85 (Campitiello et al. 2021). IC 5337 is a massive RPS galaxy and its short X-ray tail is luminous, also with multi-phase medium and SF detected. The X-ray tail of KAZ 364 is however very short.

More X-ray tails behind cluster late-type galaxies were recently presented in Sun et al. (2022), including CGCG 097-079, 2MASX J11443212+2006238 and CGCG 097-092 in A1367, NGC 4848, GMP 3816 (or NGC 4858) and GMP 4555 in Coma, all benefiting from recent deep Chandra and XMM-Newton observations. Sun et al. (2022) also presented a tight, linear correlation between the X-ray surface brightness and the H α surface brightness in the RPS tails at scales of $\sim 10 - 40$ kpc.

From all the studies so far, we now know the following properties of X-ray tails behind cluster late-type galaxies: 1) The gas temperature is typically 0.8 - 1.2 keV, if fitted with a single thermal component (e.g., APEC). However, this should only be taken as an effective temperature as the tail is multi-phase with a broad temperature distribution (e.g., Sun et al. 2010). 2) the best-fit abundance is low (0.1 - 0.4 solar typically) from the single- T fits (Sun et al. 2022), which again suggests the multi- T components in the X-ray tails. This is similar to the “iron bias” first identified in X-ray cool cores. Non-equilibrium ionization may also play a role on the low abundance (Sun et al. 2010). 3) a strong H α - X-ray linear correlation for diffuse gas beyond the star-forming regions has been established in tails (Sun et al. 2022) at 10 - 40 kpc scales, which suggest mixing of the cold ISM and the hot ICM as the origin of multi-phase tails behind cluster late-type galaxies. Both X-ray and H α surface brightness may be tied to the external pressure of the surrounding ICM (Sun et al. 2010; Tonnesen et al. 2011). 4) star formation in stripped tails can produce high-mass X-ray binaries and even ultraluminous X-ray sources (Sun et al. 2010; Poggianti et al. 2019a).

Soft X-ray emission in the stripped tails provides an important constraint on mixing and serves as a key link between the external heat pool of the ICM and the stripped cold ISM. Looking forward, more X-ray tails should be discovered from the eRosita survey in 5 - 10 years and eventually future X-ray observatories like Athena and Lynx will allow X-ray kinematics and line diagnostics studies in the tails, besides adding many more detections. Trajectories of cluster galaxies can no longer be hidden in X-rays!

3.2.6 Dust

As a major constituent of the ISM, the dust component is also expected to be removed during the hydrodynamic interaction with the surrounding ICM. Stripping, however, should be less efficient than for the diffuse HI since dust is mainly associated to the molecular gas component deeply embedded into giant molecular clouds (see Sec. 3.2.3). Considering that the typical gas-to-dust ratio (G/D) in spiral galaxies is of the order of ~ 100 we can roughly estimate that for a gas loss of $M_{\text{gas}} \simeq 10^8 - 10^9 M_{\odot}$ in a typical late-type galaxy of stellar mass $M_{\text{star}} \simeq 10^8 - 10^9 M_{\odot}$ the amount of dust removed during the interaction is $M_{\text{dust}} \simeq 10^6 - 10^7 M_{\odot}$. If, once removed, this dust is distributed on a diffuse tail of ~ 50 kpc length and ~ 10 kpc width, its typical column density would be $\Sigma_{\text{dust}} \simeq 2 \times 10^3 - 2 \times 10^4 M_{\odot} \text{ kpc}^{-2}$. This estimate can be refined considering that the gas-to-dust ratio is metallicity dependent as (Rémy-Ruyer et al. 2014)¹⁰; see also Sandstrom et al. (2013):

$$\log(G/D) = 2.21 + (8.69 - 12 \log \text{O}/\text{H}) \quad (39)$$

where the solar metallicity is $12 + \log \text{O}/\text{H} = 8.69$ (Asplund et al. 2009), which leads to $G/D_{\odot} = 164$ (Zubko et al. 2004).

Dust masses and column densities can be transformed into flux densities S_{λ} and surface brightnesses in different photometric far-IR bands using the relation (e.g. Spitzer 1978; Boselli 2011):

$$M_{\text{dust}} = \frac{S_{\nu} D^2}{K_{\nu} B(\nu, T)} \quad (40)$$

where D is the distance of the galaxy, K_{ν} the grain opacity at a given frequency and $B(\nu, T)$ the Planck function for dust at a temperature T . Assuming a dust temperature of $T = 20$ K, a grain opacity of $K_{250} = 4.00 \text{ cm}^2 \text{ g}^{-1}$ (Draine 2003), the typical far-IR surface brightnesses of these tails would be $\Sigma S_{250\mu\text{m}} \simeq 5\text{-}50 \mu\text{Jy arcsec}^{-2}$. These surface brightness values are comparable to the confusion limit of SPIRE on Herschel (5.8, 6.3, 6.8 mJy/beam at 250, 350, and 500 μm respectively, which for a beam size of FWHM 18.1, 24.9, and 36.6 arcsec correspond to 22.6, 12.9, 6.5 $\mu\text{Jy arcsec}^{-2}$, Nguyen et al. (2010) and are thus hardly detectable with this instrument even using very deep observations. Thanks to their resolving power, interferometric observations such as those available with ALMA or NOEMA at the Plateau du Bure would thus be ideal to resolve the background point sources from the diffuse and extended emission of the dust tails possibly formed during an RPS event.

At present the only study dedicated to the detection of the diffuse dust component in the tail of ram pressure stripped galaxies is the work of Longobardi et al. (2020b). Using the far-IR data gathered during the Herschel Reference Survey (HRS; (Boselli et al. 2010), a complete survey of a K -band selected, volume-limited sample of nearby galaxies with available data in the SPIRE (250, 350, 500 μm , (Ciesla et al. 2012) and PACS (100, 160 μm , (Cortese et al.

¹⁰ Different recipes for gas-to-dust ratio vs. metallicity relation are given in this reference.

2014)) bands, Longobardi et al. (2020b) looked for and detected with a typical S/N of ~ 5 a diffuse dust component associated to the H I and H α tails of three Virgo cluster galaxies (NGC 4330, 4522, 4654) undergoing an RPS event (Chung et al. 2007). The gas-to-dust ratio derived in these tails for reasonable values of T are consistent with those observed in the outer disc of spiral galaxies, making the detection trustworthy, and confirming that during an RPS event dust is removed with the other components of the ISM (Longobardi et al. 2020b). This also indicates that dust stripped from gas-rich late-type systems can contribute to the pollution of the ICM (Domainko et al. 2006; Longobardi et al. 2020a). The results of Longobardi et al. (2020b) are in line with the evidence that cluster galaxies have, on average, a dust-to-stellar mass ratio lower than that of similar objects in the field, as observed by Bianconi et al. (2020) in the cluster A1758. They are also consistent with the presence of kpc scale dusty filaments partly decoupled from the surrounding ISM perpendicular to the plane of the disc seen in absorption in the spectacular HST images of a few ram pressure stripped galaxies in the Virgo cluster (Abramson et al. 2016). For completeness, it is also worth mentioning that dust has been detected in the tails of ram pressure stripped galaxies using absorption line measurements through the Balmer decrement (Fossati et al. 2016; Poggianti et al. 2019a). This dust, however, has a clumpy structure since it has been formed within the star forming regions present in some of the perturbed galaxies. This observational technique is hardly applicable to the diffuse ionised gas since it requires that the gas is photoionised by the young stellar component (case B), which is not always the case in these particular environments (see Sec. 3.2.4).

3.3 Indirect effects on the stellar spatial distribution

While the ICM ram pressure cannot move stars, it can affect the stellar distribution of the galaxy indirectly, if the stripped ISM can form stars. Star formation in the stripped ISM was suggested in the early simulations by Schulz & Struck (2001). Isolated star formation has been known in the Virgo cluster since 2002 (Gerhard et al. 2002; Cortese et al. 2004a) but lacked direct evidence to link with RPS (also see discussion in Yoshida et al. 2004). The first observational data to reveal star formation in the stripped ISM come from Owen et al. (2006) on C153 in Abell 2125, Cortese et al. (2007) on 235144-260358 in Abell 2667 and 131124-012040 in Abell 1689, Sun et al. (2006, 2007a) on ESO 137-001 in Norma, Yoshida et al. (2008) on RB199 and Smith et al. (2010), Hester et al. (2010), Yagi et al. (2010) in several other galaxies in Coma. As tidal effect always exists for cluster galaxies, it was important to have this “early burst” of observational evidence to firmly establish the action of star formation in the stripped ISM by ram pressure. Since then, many more examples have been revealed. At intermediate redshift, where the full extent of clusters has been easier to cover with deep UV¹¹ and optical imaging, galaxies

¹¹ Diffuse filaments in the FUV and NUV bands must be interpreted with care since the UV emission could be originating from hydrogen 2-photon continuum or resonant lines of

with blue knots of star formation outside of the stellar disk have been found by Cortese et al. (2007). More recently Ebeling et al. (2014) presented a large survey of such objects in X-Ray selected clusters at $z > 0.3$, directly linking star forming knots to RPS.

These objects, commonly named “jellyfish galaxies” because of their peculiar morphology with tentacles of materials that appears to be stripped from the main body of the galaxy (e.g. Chung et al. 2009a; Ebeling et al. 2014; Poggianti et al. 2016), have been more recently defined by Ebeling et al. (2014) whenever they exhibit in optical broad band images the following features:

- 1) a strongly disturbed morphology indicative of unilateral external forces.
- 2) a pronounced brightness and colour gradient suggesting extensive triggered star formation.
- 3) a compelling evidence of a debris trail.
- 4) the directions of motion implied by each of these three criteria have to be consistent with each other.

Since their discovery in intermediate redshift massive clusters ($z \sim 0.2$) by Owen et al. (2006) and Cortese et al. (2007) who did not yet use the term “jellyfish”, these objects are now becoming common in different environments in the local (Smith et al. 2010; Poggianti et al. 2016, 2017b) and intermediate redshift Universe up to $z \simeq 0.7$ (Owers et al. 2012; Ebeling et al. 2014; Rawle et al. 2014; McPartland et al. 2016; Ebeling & Kalita 2019; Roman-Oliveira et al. 2019; Durret et al. 2021). From the relative position of these galaxies with respect to that of the cluster (they are principally located in the outskirts), and from the analysis of their velocity distribution it has been concluded that jellyfish galaxies are infalling within the high-density region as a group along trajectories with high impact parameters rather than infalling into the cluster centre along filaments (small impact parameters) as individual objects (McPartland et al. 2016; Ebeling & Kalita 2019).

We want to stress, however that jellyfish galaxies defined solely per the criteria above can not be *a priori* considered as systems undergoing an RPS event because the stellar distribution has a too small cross-section to be perturbed by the external gas flow¹². Galaxies with this morphological aspect can be the results of an RPS event only if all stars in the tail have been formed outside the stellar disc after the stripping event. Indeed, as largely discussed in Cortese et al. (2007), these asymmetric morphologies with strong colour (age) gradients in the stellar populations and stellar tails can also be produced in long-lived gravitational interactions with nearby companions (Merritt 1983), high velocity encounters with other cluster members (harassment, Moore et al. (1998, 1999)), or by the perturbation induced by the gravitational potential well of the cluster (Byrd & Valtonen 1990; Valluri 1993). RPS is a relatively short-lived process ($\lesssim 500$ Myr, see Sec. 4.2), it is thus conceivable that stars

CIV and MgII generated by shocks rather than from stellar continuum emission (e.g., Bracco et al. 2020).

¹² The case of Mira indicates that the external pressure can perturb the wind produced by the mass loss of evolved stars as AGB stars (e.g., Li et al. 2019b). In general, stellar winds are subject to ram pressure.

with ages older than these typical timescales have been formed within the disc of the galaxy and later removed during the interaction. For this reason optical selections, which are sensitive to the distribution of stellar populations of ages of several Gyrs, can be easily contaminated by galaxies undergoing gravitational perturbations.

We can quantify the importance of high velocity gravitational interactions with other cluster members or with the potential well of the cluster and compare them to those of RPS following [Henriksen & Byrd \(1996\)](#) and [Cortese et al. \(2007\)](#). An infalling galaxy suffering a gravitational perturbation is subject to two different accelerations, a radial tidal one (a_{rad}), which is pulling matter along the direction connecting the galaxy and the perturber on either sides of the disc:

$$a_{rad} = GM_{pert} \left[\frac{1}{r^2} - \frac{1}{(R+r)^2} \right] \quad (41)$$

and a transverse acceleration (a_{tr}), which is pushing matter versus the inner regions on the disc and in the nucleus along the direction perpendicular to the line connecting the galaxy and the perturber ([Henriksen & Byrd 1996](#); [Cortese et al. 2007](#)):

$$a_{tr} = GM_{pert} \frac{R}{[R^2 + (R+r)^2]^{1.5}} \quad (42)$$

where M_{pert} is the mass of the perturber within r , R is the radius of the perturbed galaxy, and r is its distance from the perturber. If the radial acceleration overcomes the internal galaxy acceleration keeping the matter linked to the gravitational potential well of the galaxy:

$$a_{gal} = \frac{GM_{dyn}}{R^2} \quad (43)$$

where M_{dyn} is the dynamical galaxy mass, the perturbation is able to remove matter from the galaxy disc. The perturber can be either another cluster galaxy or the cluster itself. As shown in [Cortese et al. \(2007\)](#), for a non-interpenetrating galaxy-galaxy high velocity encounter the impact parameter is at least equal or greater than the galactic radius ($R \geq r$), which implies that the interaction is able to remove mass only whenever $M_{pert} \geq 1.33M_{dyn}$, and the perturber should not be at a distance larger than the typical length of the tail. This condition makes the formation of jellyfish galaxies quite unlikely for massive objects, whose number density in rich cluster remains limited, while it is still possible in low mass, low surface brightness systems ([Moore et al. 1999](#); [Mastropietro et al. 2005](#)).

Both dwarfs and massive systems, however, can be perturbed by the gravitational potential well of the cluster itself. Following [Cortese et al. \(2007\)](#) we can quantify the effect of tidal forces induced by gravitational potential well of the cluster by assuming a NFW mass profile ([Navarro et al. 1997](#)) given in Sec. 2.1 where the mass of the perturber M_{pert} is derived using Eq. 9. We can than

estimate under which conditions $a_{\text{rad}} \leq a_{\text{gal}}$ in different clusters such as Virgo, Coma, and A1689 and in representative galaxies of stellar mass $M_{\text{star}} = 10^{10}$, 10^9 , and $10^8 M_{\odot}$. For the three clusters we use the NFW parameters given in Table 1. For the galaxies we calculate the total dynamical mass M_{dyn} following Behroozi et al. (2013), and assume as radii $r = 1.5 R_{23.5}(i)$ derived from SDSS data of the HRS galaxies by Cortese et al. (2012), thus considering that the stellar disc extends outside the i -band isophotal radius measured on the shallow SDSS images, as indeed deep UV images suggest (XUV discs, e.g. Thilker et al. (2007)). Figure 7 shows that, under some conditions, galaxies can be tidally perturbed by the gravitational potential well of the cluster up to $\simeq 250$ kpc from the cluster centre. This process is more efficient in massive clusters ($M_{\text{pert}} > 10^{15} M_{\odot}$) and in galaxies of intermediate stellar mass ($M_{\text{star}} \simeq 10^9 M_{\odot}$) because of their low $M_{\text{dyn}}/M_{\text{star}}$ ratio. We should recall that these estimates are probably lower limits because this effect is expected to be more efficient if the galaxies infall into the clusters within small groups, as indeed semi-analytic models and hydrodynamic cosmological simulations suggest: $\sim 40\%$ of the galaxies in massive clusters have been accreted as satellites of smaller groups (Gnedin 2003b,a; McGee et al. 2009; De Lucia et al. 2012; Han et al. 2018). In this case, high speed encounters with other members can rapidly change the gravitational field of the infalling galaxies, accelerating mass loss for tidal heating (Taylor & Babul 2001).

Using similar arguments we can also estimate which is the truncation radius outside which matter is removed from the perturbed galaxy (Binney & Tremaine 2008):

$$R_{\text{trunc}} \simeq R \left(\frac{M_{\text{dyn}}}{M_{\text{pert}}(< r)} \right)^{1/3} \quad (44)$$

Figure 8 shows how the truncation radius changes as a function of the distance from the cluster core for representative galaxies of three different stellar mass ($M_{\text{star}} = 10^{10}$, 10^9 , and $10^8 M_{\odot}$) whose typical optical isophotal radius is $R_{23.5}(i) = 10, 5, 2$ kpc (Cortese et al. 2012), often ($\sim 30\%$) characterised by extended UV discs of twice the optical size and with HI discs of size $\simeq \times 1.8$ - 1.9 the optical size (Cayatte et al. 1994, see Sec. 3.4). As mentioned above, in massive clusters ($M_{\text{cluster}} \simeq 10^{15} M_{\odot}$) gravitational perturbations are able to remove gas and stars in the outer discs of infalling galaxies whenever they get close to the core of the cluster. The observed by Cortese et al. (2007) in two massive clusters at $z \simeq 0.2$ have been probably formed after the combined action of the gravitational interaction with the potential well of the clusters and ram pressure. To conclude, although the jellyfish morphology suggests an ongoing hydrodynamical interaction with the surrounding ICM, gravitational interactions can produce similar properties in the perturbed systems thus this peculiar morphology cannot be taken by itself as an unambiguous sign of an ongoing RPS event.

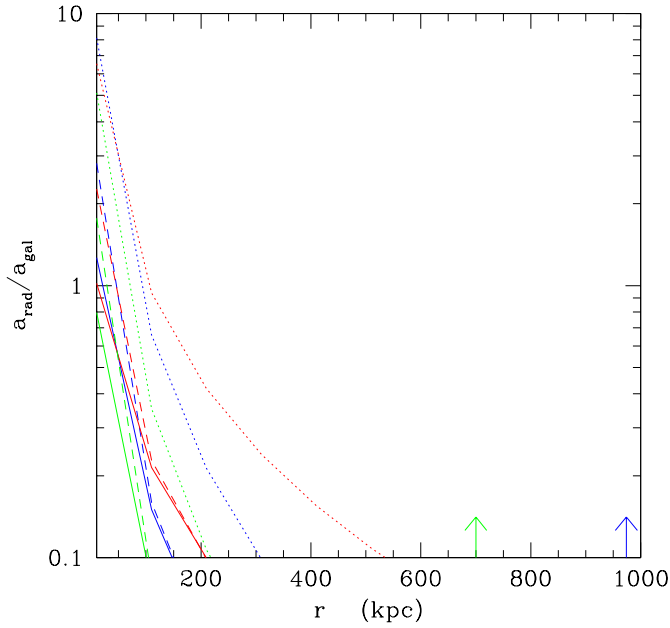


Fig. 7 Variation of the ratio between the radial acceleration on the galaxy disc induced by the gravitational potential well of the cluster (a_{rad}) and the acceleration due to the potential well of the galaxy (a_{gal}) as a function of the distance from the cluster centre for four representative high density regions (Groups - green; Virgo - blue; Coma - red). The different lines are for galaxies of different stellar mass: solid ($M_{\text{star}} = 10^{10} M_{\odot}$), dotted ($M_{\text{star}} = 10^9 M_{\odot}$), and dashed ($M_{\text{star}} = 10^8 M_{\odot}$). The green and blue vertical arrows indicate r_{200} for groups and for the Virgo cluster, respectively. The mass of the overdensity regions are derived using a NFW density profile assuming $c = 8.6, 4,$ and 8 for the Virgo, Coma, and Fornax (group) clusters, respectively, with $r_s = r_{200}/c$.

3.4 Truncated discs

Cluster galaxies are generally deficient in H I gas (see Sec. 3.6). Interferometric observations at 21 cm of late-type systems in nearby clusters have shown that the H I deficiency¹³ is in most cases due to a reduced H I discs. In Virgo, where all objects are fully resolved thanks to the proximity of the cluster, it has been shown that the degree of truncation of the H I disc increases towards the core of the cluster where RPS is more efficient (Warmels 1986; Cayatte et al. 1990, 1994; Chung et al. 2009a). A similar trend has been observed also in the Coma (Bravo-Alfaro et al. 2000) and Fornax clusters (Loni et al. 2021). Given the radial exponentially declining gas and stellar surface densities of late-type galaxies, Eq. 21 indicates that during a face-on interaction RPS

¹³ The H I deficiency parameter, first defined by Haynes & Giovanelli (1984), is a measure of the logarithmic difference between the expected and the observed H I mass of galaxies of different morphological type and size, where the estimated measure is taken from standard scaling relations of unperturbed galaxies in the field. For an updated calibration of these relations, see Boselli & Gavazzi (2009).

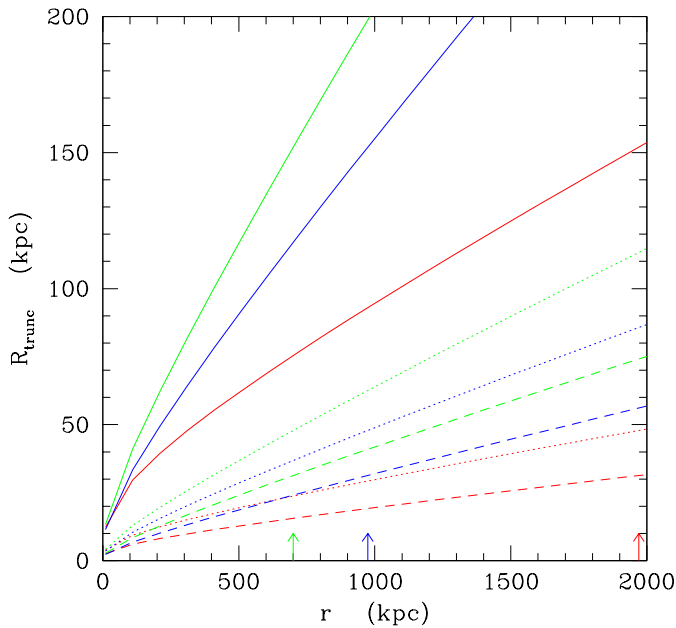


Fig. 8 Variation of the truncation radius as a function of the distance from the cluster centre for four representative high density regions (Group - green; Virgo - blue; Coma - red). The different lines are for galaxies of different stellar mass: solid ($M_{\text{star}} = 10^{10} M_{\odot}$), dotted ($M_{\text{star}} = 10^9 M_{\odot}$), and dashed ($M_{\text{star}} = 10^8 M_{\odot}$). The vertical arrows indicate r_{200} for the different clusters.

removes the gas located in the outer disc producing truncated profiles while unperturbing the stellar distribution (outside-in, (Warmels 1988a,b,c; Cayatte et al. 1990, 1994; Vollmer et al. 2001b)). It should be noted that, because of the conservation of the angular momentum including that of the spin vector, a late-type system entering a cluster will soon or late cross the ICM face-on although this might occur at different clustercentric distances if the infall is along a radial orbit. The observed outside-in truncation of the gaseous disc is in line with the prediction of simple models (Hester 2006) and hydrodynamic simulations (Abadi et al. 1999; Quilis et al. 2000; Roediger & Hensler 2005; Roediger & Brüggen 2007).

Truncated discs in cluster galaxies have been also observed in other components of the ISM, from the molecular gas (Fumagalli et al. 2009; Boselli et al. 2014b; Mok et al. 2017) to the dust (Cortese et al. 2010, 2014), with similar trends of the ratios of the CO-to-optical and dust-to-optical radii with the HI-deficiency parameter, suggesting that all the different components of the ISM are stripped away during the interaction. Figure 9 shows the relationship between the ratio of the HI and molecular gas isophotal radii to the optical radius (stars) as a function of the HI-deficiency parameter for the sample of Virgo cluster galaxies with interferometric HI data gathered during the VIVA survey (Chung et al. 2009a) and with available CO maps (Chung et al.

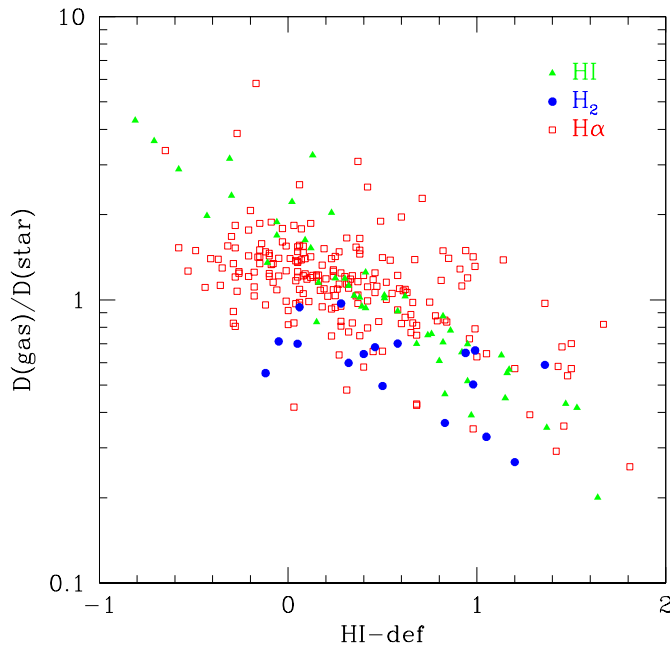


Fig. 9 Variation of the gas-to-stellar disc diameters of the atomic (green filled triangles, with HI isophotal diameters taken from [Chung et al. \(2009a\)](#)), the molecular (blue solid circles, with isophotal CO diameters taken from [Chung et al. \(2009b\)](#)), and the ionised (red empty squares, with effective H α equivalent width diameters taken from [Boselli et al. \(2015\)](#)) gas phases as a function of the HI-deficiency parameter for galaxies in the Virgo cluster (HI, CO) and in the Herschel Reference Survey (H α).

2009b). Figure 9 clearly shows how the gaseous disc is reduced with respect to the stellar disc in galaxies deprived of their HI content, indicating that the stripping occurs outside-in. In the most deficient galaxies ($HI - def \simeq 1$) the gas disc is a factor of $\simeq 2$ less extended than the optical disc, as expected in a ram pressure stripping scenario where only the gaseous component is removed while leaving unaffected the stellar disc. It also shows that the molecular gas component, mainly located in the inner disc within giant molecular clouds, is less subject to gas stripping than the diffuse HI component (see Sec. 3.2.3).

The lack of gas, principal feeder of star formation, quenches the activity of star formation in the outer disc, producing truncated discs also in the youngest stellar populations such as those traced by the H α line (O-early B stars of age ≤ 10 Myr, ([Kennicutt 1998](#); [Boselli et al. 2009](#))), or by the UV emission (A-F stars of age ≤ 100 Myr), as depicted in Fig. 9. Truncated discs in H α and UV have been observed in several HI-deficient Virgo cluster galaxies by [Koopmann & Kenney \(2004a,b\)](#); [Koopmann et al. \(2006\)](#), [Boselli & Gavazzi \(2006\)](#), [Cortese et al. \(2012\)](#), and [Fossati et al. \(2013\)](#), and predicted by simulations ([Bekki 2009, 2014](#); [Tonnesen & Bryan 2012](#)). In dwarf galaxies, simulations indicate that the gas can be retained only in the nucleus, where the gravita-

tional potential well is the deepest (Steyrleithner et al. 2020). This gas can feed a nuclear activity of star formation, as indeed observed in several dwarf ellipticals in the Virgo cluster probably formed after an RPS event (Boselli et al. 2008a). The time elapsed since the first gas removal can be estimated by comparing models predictions of radial gas stripping on the age-sensitive stellar populations observed in different photometric bands, as firstly done on the iconic galaxy NGC 4569 in the Virgo cluster (Boselli et al. 2006), illustrated in Fig. 10. As shown in this figure, all the different components of the ISM (atomic, molecular, ionised, and hot gas, dust) have been removed away from the outer disc during the stripping event. The lack of gas also reduced the activity of star formation, which is now limited only to the inner disc. The truncation of the star forming disc has been observed in other environments down to massive groups (Bretherton et al. 2013; Schaefer et al. 2017, 2019; Owers et al. 2019) and in clusters at redshift $0.3 < z < 0.6$ (Vaughan et al. 2020).

3.5 Asymmetries

It has been suggested that galaxies suffering an external pressure can be characterised by an asymmetric distribution of the gas within the stellar disc, sometime visible also in the shape of the two-horns H I profile (Gavazzi 1989; Roberts & Parker 2020). In an edge-on interaction, the gas is compressed on the leading side while it is stretched along the tail on the opposite side, as indeed observed in several representative galaxies (CGCG 097-073 and CGCG 097-087 in A1367, (Gavazzi et al. 1995, 2001a; Consolandi et al. 2017; Pedrini et al. 2022); NGC 4501, NGC 4654 and IC 3476 in Virgo, (Vollmer et al. 2008b; Nehlig et al. 2016; Vollmer 2003; Boselli et al. 2021); ESO 137-001 in Norma, (Sun et al. 2007a; Fossati et al. 2016). At the leading side, the compressed gas can form a bow-shocked structure where star formation can take place, sometime after a vigorous burst which leads to the formation of giant H II regions as those observed in CGCG 097-073 in A1367 (Gavazzi et al. 1995, 2001a) and IC 3476 in Virgo (Boselli et al. 2021). The compression of the gas on the leading side occurs also in less inclined interactions, although in a less spectacular way (Bekki 2014). By comparing the properties of a sample of 11 ram pressure stripped galaxies extracted from the GASP survey to those of a reference sample of unperturbed objects, Bellhouse et al. (2021) have shown that the pitch angle of perturbed galaxies increases radially as predicted by tuned simulations. Ram pressure, thus, unwind the spiral arms of cluster galaxies. The presence of asymmetries can be taken as a proof of an ongoing RPS event only whenever the distribution of the old stellar population is unaffected. This is something difficult to demonstrate even when deep near-IR imaging is available since red supergiants formed after the interaction can heavily contaminate these photometric bands. A less biased tracer is the asymmetry of the stellar and gas radial velocities, made accessible by large FoV IFU instruments. In these cases (Fossati et al. 2016, 2018) the asymmetry of the ionised gas distri-

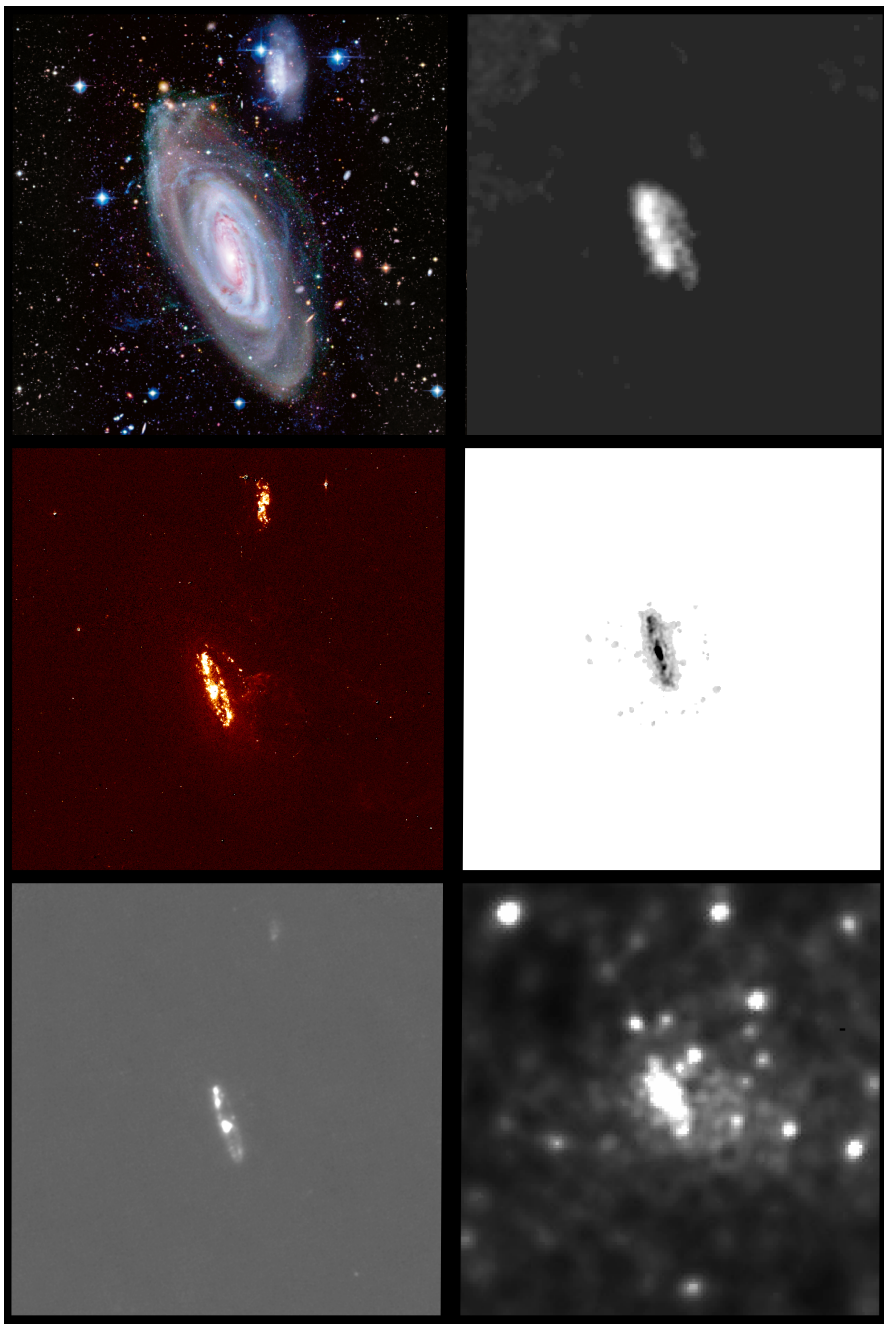


Fig. 10 Comparison of the 2D-distribution of the different components of the RPS galaxy NGC 4569. Left column, from top to bottom: colour image tracing the distribution of the stellar component (adapted from [Boselli et al. \(2016a\)](#)); continuum subtracted $H\alpha$ image tracing the distribution of the star forming regions (adapted from [Boselli et al. \(2016a\)](#)); Herschel/PACS image at $70\ \mu\text{m}$ tracing the distribution of the dust component (from the KINGFISH survey, [Kennicutt et al. 2011](#)). Right column, from top to bottom: atomic gas distribution (from the VIVA survey, [Chung et al. \(2009a\)](#)); molecular gas distribution derived from the $^{12}\text{CO}(1-0)$ line transition (from the BIMA survey, [Helfer et al. 2003](#)); hot gas distribution from XMM-Newton. All panels are on the same spatial scale.

bution marks a strong contrast with symmetric stellar rotation fields in case of pure RPS, while in the case of gravitational interactions we see clear signs of the perturbation of the stellar rotation field (Boselli et al. 2021; Bellhouse et al. 2021, see also Sec. 4.4).

Asymmetries in the different gas phases of the ISM have been systematically searched for and observed in several nearby clusters whenever the angular resolution of the data was not prohibitive. Evidence of an asymmetric distribution of the HI gas has been first observed by Warmels (1988c), Cayatte et al. (1990), Chung et al. (2009a), and Reynolds et al. (2020) in the Virgo cluster, by Scott et al. (2018) in A1367, and Bravo-Alfaro et al. (2000) in Coma. Asymmetries have been also looked for in the molecular gas component (Scott et al. 2015), although systematic studies of complete samples of cluster galaxies are still lacking.

Thanks to its high angular resolution, narrow-band H α imaging data are perfectly suited to trace the distribution of the gas ionised by young ($\lesssim 10$ Myr) massive ($\gtrsim 10 M_{\odot}$) stars (Kennicutt 1998; Boselli et al. 2009) formed after the interaction. Given the stochasticity of the star formation process, which results in a clumpy structure over the entire galactic disc, the interpretation of asymmetries as a product of an external perturbation can be reached only on statistical basis when confronted to a reference sample of unperturbed, field objects, or in the study of selected objects in conjunction with other indicators. Asymmetries in the ionised gas distribution have been searched for using the concentration, asymmetry, and smoothness (CAS) parameters (Conselice et al. 2000) in the nearby clusters Virgo, Coma, and A1367 by Fossati et al. (2013) and Boselli et al. (2015). When plotted against the HI-deficiency parameter, often used as a direct tracer of an ongoing or past external perturbation, the CAS parameters are fairly constant in the r -band, while the asymmetry parameter $A_{H\alpha}$ and the clumpiness parameter $S_{H\alpha}$ systematically decrease with increasing HI-deficiency. This trend, however, has been interpreted as a second order effect related to the decrease of the specific star formation activity observed in cluster galaxies rather than an evidence of an ongoing RPS event. The presence of galaxies suffering an ongoing perturbation in the Coma cluster has been also claimed after the analysis of the structural parameters of galaxies extracted from a set of high-resolution broad band optical images by Roberts & Parker (2020). The presence of asymmetries has been correlated with their direction and the position of the galaxies within the cluster to identify objects undergoing an RPS event. Finally, it is worth mentioning that associated to these asymmetries in the stellar distribution, stars are also less concentrated in the inner regions as indicated by a lower Sercic index compared to unperturbed systems (Roman-Oliveira et al. 2021).

3.6 Integrated properties

The tight relationship between the radial extent of the different components of the ISM and the total available reservoir of atomic gas shown in Fig. 9

naturally brought to the general assumption that the HI-deficiency parameter can be statistically taken as an indirect tracer of an RPS perturbation (e.g. [Boselli & Gavazzi 2006](#)). Since this parameter can be easily derived from single dish observations of unresolved galaxies, available for several thousands of objects in the nearby Universe, the HI-deficiency parameter has become one of the most used tracer of RPS in statistical analyses (e.g. [Haynes & Giovanelli 1984](#); [Solanes et al. 2001](#); [Catinella et al. 2013](#); [Boselli et al. 2014b,d](#); [Gavazzi et al. 2005, 2006b, 2013b](#); [Loni et al. 2021](#)).

It has been shown that the HI-deficiency parameter systematically increases towards the centre of rich clusters of galaxies consistently with the observed decrease of the HI-disc extension gathered from interferometric observations (see Sec. 3.4). The statistical analysis of large samples of galaxies in nearby clusters has indicated that the atomic hydrogen starts to be depleted at clustercentric distances as high as $\simeq 1-2 \times r_{200}$ reaching its maximum at the cluster centre where up to $\gtrsim 90\%$ of the atomic gas can be stripped ([Solanes et al. 2001](#); [Gavazzi et al. 2005, 2006b, 2013b](#); [Healy et al. 2021](#); [Morokuma-Matsui et al. 2021](#)). Again, this statistical evidence matches the results obtained from the analysis of representative objects with interferometric data showing the presence of extended HI tails up to similar clustercentric distances (see Sec. 3.2.2). It has been shown that the fraction of HI-deficient galaxies increases as a function of the X-rays luminosity of the cluster ([Giovanelli & Haynes 1985](#)), as expected considering that the X-ray luminosity is tightly connected to the density of the ICM. This relation, however, has not been confirmed on a large sample by ([Solanes et al. 2001](#)). The correlation between the HI-deficiency parameter and the X-rays luminosity, however, seems to be valid locally when the hot gas distribution is compared to the position of individual objects as done in the Virgo cluster ([Solanes et al. 2001](#); [Boselli et al. 2014d](#)). Furthermore, HI-deficient galaxies are preferentially located on radial orbits ([Solanes et al. 2001](#)). Using a combination of direct observations and stacking techniques, it has been also shown that groups of galaxies are also populated by HI-deficient late-type systems ([Fabello et al. 2012](#); [Catinella et al. 2013](#); [Hess & Wilcots 2013](#); [Brown et al. 2017](#); [Hu et al. 2021](#)). HI-deficiency has been also observed in compact groups by [Verdes-Montenegro et al. \(2001\)](#) and interpreted as possibly/partly due to ram pressure in some of these objects by [Rasmussen et al. \(2008\)](#). Similarly, a decrease of the atomic gas content has been observed also in the filaments at the periphery of the Virgo cluster ([Castignani et al. 2022](#)). We recall, however, that this last observational evidence cannot be unequivocally interpreted as an evidence of RPS just because the atomic gas, being loosely bound to the gravitational potential well of the galaxy, can be removed also by gravitational perturbations.

By comparing the integrated properties of different samples of local galaxies [Fumagalli et al. \(2009\)](#) and [Boselli et al. \(2014b\)](#) have shown that the molecular gas content also decreases in HI-deficient galaxies, suggesting that part of the molecular phase can be stripped away along with the atomic gas (see however [Mok et al. 2016](#); [Chung et al. 2017](#)). In some galaxies such as NGC 4569 the stripping process can affect also the dense molecular gas component ([Wilson](#)

et al. 2009). The stripping of the molecular gas component, which is deeply embedded in the gravitational potential well of the galaxies in large part inside giant molecular clouds with a low cross section vs. the external pressure, is less efficient than that of the atomic phase, leading to an increase of the H_2/HI gas ratio. These results are in line with the most recent Illustris TNG100 hydrodynamical simulations (Stevens et al. 2021), or with tuned simulations of RPS in local galaxies (e.g. Tonnesen & Bryan 2009; Boselli et al. 2021). Being closely connected to the star formation process, the lack of atomic and molecular gas induces a reduction of the star formation activity (e.g. Koyama et al. 2017) which is observed in late-type cluster galaxies at roughly similar clustercentric distances ($R/r_{200} \simeq 1 - 2$; (Lewis et al. 2002; Gómez et al. 2003; Gavazzi et al. 2013b), in groups (Hu et al. 2021), or in the filaments surrounding rich structures such as Virgo (Castignani et al. 2022). It is worth noticing that in the specific population of jellyfish galaxies (see Sec. 3.2.3) the molecular gas fraction is the dominant cold gas component over the disc of the perturbed systems (Moretti et al. 2020a). Here the observed increase in the H_2/HI ratio is probably related to the increase of the external pressure which favors the formation of molecular hydrogen (Blitz & Rosolowsky 2006). This molecular gas formation, however, seems to occur only under a specific geometrical configuration, where the interaction with the surrounding ICM is mainly edge-on. In this case, the gas is compressed over the disc of the galaxy on the leading side of the interaction, producing a bow-shocked region where the gas density increases and the star formation can be boosted, as indeed observed in the galaxy IC 3476 in the Virgo cluster (Boselli et al. 2021), or predicted by tuned simulations (Safarzadeh & Loeb 2019).

Given that along with the gaseous component also dust and metals can be stripped during the perturbation, and that ram pressure preferentially removes gas located in the outer disc, which is known to be metal poor, the stripping process can alter the typical metallicity and dust-to-gas ratio of the perturbed galaxies. Effects on the gas metallicity of ram pressure stripped galaxies have been first looked for by Skillman et al. (1996) in nine Virgo cluster galaxies. Their analysis have shown that HI-deficient galaxies in the core of the cluster have, on average, higher gas metallicities than similar objects in the field. This result has been later confirmed on a large sample of 260 late-type galaxies in nearby clusters by Hughes et al. (2013), and interpreted as due to the removal of the gas poor component located in the outer regions (for a different interpretation see Peng et al. (2015) and Gupta et al. (2017)). By studying the properties of galaxies extracted from the *Herschel* Reference Survey (Boselli et al. 2010), a complete volume-limited, mass-selected sample of local galaxies with a complete set of multifrequency data, Cortese et al. (2016) have shown that while the $M_{\text{gas}}/M_{\text{dust}}$ ratio varies by no more than a factor of two when moving from the core of the Virgo cluster to the field, the $M_{\text{HI}}/M_{\text{dust}}$ ratio increases and the $M_{\text{H}_2}/M_{\text{dust}}$ decreases with the HI-deficiency. They have explained this opposite behaviour as due to a different radial distribution of the different gas phases and of the dust component whenever the stripping process occurs outside-in, as indeed happens during an RPS event. These results are

fairly consistent with the previous work of [Corbelli et al. \(2012\)](#). Evidence for dust stripping in rich environments comes also from the multifrequency study of the cluster A1758 which shows a decrease of the dust-to-stellar mass ratio and a lower level of infrared emission in the star forming galaxies belonging to the cluster with respect to that of similar and coeval objects in the field ([Bianconi et al. 2020](#)).

3.7 Galaxy distribution within high-density regions

The radial decrease of the density of the ICM and that of the velocity of infalling galaxies suggest that outside a given clustercentric radius, which might depend on the properties of the high-density regions and of the mass of the perturbed system, ram pressure is not sufficient to overcome the gravitational forces keeping the gas anchored to the gravitational potential well of the galaxy. The observation of galaxies with evident signs of an ongoing interaction, such as extended tails of gas in its different phases, or of truncated discs, have been used to physically identify the region where RPS is active. The results of these works are summarised in [Sec. 3.7.1](#). Thanks to the advent of deep spectroscopic surveys on statistically significant samples we are now able to add the relative velocity of perturbed galaxies as a new parameter to trace their distribution within the gravitational potential well of high-density regions. Positions and velocities have been recently used to trace the distribution of galaxies within the phase-space diagrams. The results of these works, which can be easily compared to the predictions of simulations, are summarised in [Sec. 3.7.2](#).

3.7.1 Galaxy distribution as a function the angular distance

In the nearby Virgo cluster, galaxies with extended tails of gas undergoing RPS have been observed up to a projected distance of $R/r_{200} \simeq 1 - 1.3$, in A1367 and in Coma up to $R/r_{200} \simeq 0.6$ and $R/r_{200} \simeq 1.4$, respectively (see [Table 2](#)), although these numbers are likely lower limits given the limited extension of the blind narrow-band H α imaging survey carried out with Suprime Cam at the Subaru telescope ([Yagi et al. 2010, 2017](#); [Gavazzi et al. 2018b](#)). Tails of gas have been observed even at further distances, up to twice r_{200} in A1367, but in objects where ram pressure combined with other mechanisms have been invoked to explain the origin of the perturbation ([Scott et al. 2012](#)). HI interferometric observations of galaxies in the Virgo cluster have also revealed that the truncation of the atomic gas disc decreases with increasing clustercentric distance, as expected in an RPS scenario ([Cayatte et al. 1990](#); [Chung et al. 2009a](#)). Galaxies with HI discs less extended than their stellar counterparts have been observed at distances up to $1.5 \times r_{200}$, although this radial distance is quite uncertain given the complex structure of the Virgo cluster. On a more solid statistical basis, it is well known that the HI-deficiency parameter starts to increase at clustercentric projected distances smaller than $1.5 \times r_{200}$ in Virgo ([Gavazzi et al. 2013b](#); [Boselli et al. 2014d](#)).

and $2 \times r_{200}$ in Coma (Gavazzi et al. 2006b; Boselli & Gavazzi 2006) and in other nearby clusters (Solanes et al. 2001). The presence of HI-deficient galaxies has been also observed along the filaments surrounding the Virgo cluster region (Castignani et al. 2022), where pre-processing might have been acting. These observational results are corroborated by the predictions of cosmological hydrodynamical simulations now able to resolve the HI gas component of satellite galaxies of stellar mass $M_{\text{star}} \sim 10^9 M_{\odot}$ (Marasco et al. 2016). These trends observed in HI are mirrored in H α : in the Virgo cluster, for instance, the star formation activity of late-type galaxies starts to decrease at the same clustercentric distance where the HI-deficiency increases ($R \simeq 1.5 \times r_{200}$; (Gavazzi et al. 2013b; Boselli et al. 2014d; Castignani et al. 2022). The same decrease of the star formation activity is seen in several other well known nearby clusters (Haines et al. 2006, 2015), and on larger samples in all high density regions in the local Universe within $1-2 \times r_{200}$ from the central galaxy as derived from the analysis of SDSS (Gómez et al. 2003), 2dF (Lewis et al. 2002), and GALEX (Catinella et al. 2013) surveys. In particular, Kauffmann et al. (2004) have shown that the decrease of star formation activity per unit stellar mass (specific star formation rate) is more pronounced in intermediate mass galaxies with respect to massive systems. This mass segregation effect in the quenching mechanism typically occurs in nearby massive haloes $M_{\text{halo}} \sim 10^{13} - 10^{14} M_{\odot}$ (Catinella et al. 2013), suggesting a relevant (although maybe not dominant) role of RPS in the quenching of a large population of galaxies orbiting these haloes. It is also worth mentioning that in two clusters at $z \sim 0.25$ the orientation of the ionised gas asymmetries, which are generally pointing away from the cluster centre, has been used to identify RPS as the dominant perturbing mechanism (Liu et al. 2021). This observational evidence also indicates that RPS occurs principally during the first passage of an infalling galaxy within the cluster, and that the quenching episode is rapid (Liu et al. 2021).

3.7.2 Galaxy distribution within the phase-space diagram

An alternative way of identifying the region of action of a given perturbing mechanism is that of plotting galaxies with evident signs of that ongoing perturbation in the phase-space diagram, i.e. in a diagram showing the relationship between the line of sight velocity of the galaxy with respect to the mean velocity of the cluster as a function of the projected distance from the cluster centre. An example of phase-space diagram is shown in Fig. 11 constructed using the sample of galaxies in the Coma supercluster of Gavazzi et al. (2010) combined with identified RPS galaxies in the Virgo, Coma, A1367, and Norma clusters given in Table 2, and the GASP sample of jellyfish galaxies. This diagram has the advantage of putting the studied galaxies extracted from different clusters in a normalized parameter space where both axis are tightly connected to the ram pressure force ($\rho_{\text{ICM}}V^2$), the line of sight velocity within the cluster (Y-axis) and the clustercentric distance, which varies as the density of the ICM. The position of galaxies in this diagram can be used to statistically

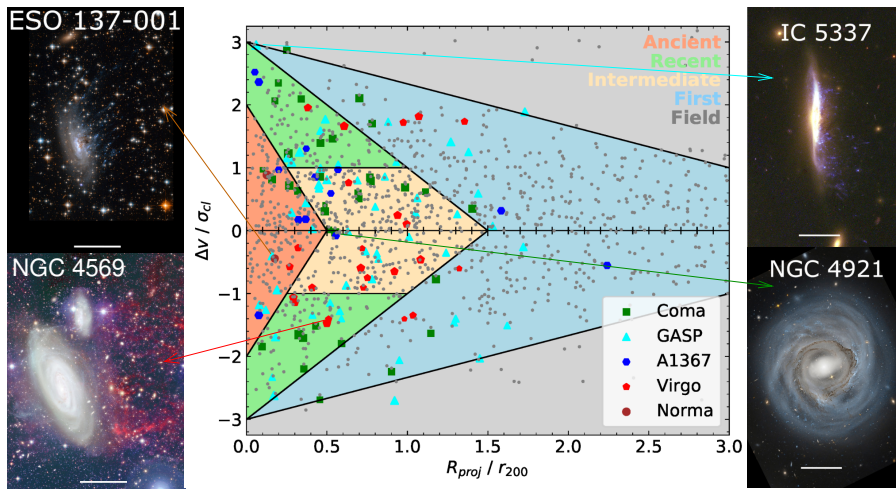


Fig. 11 Phase-space diagram of the Coma supercluster constructed using the sample of (Gavazzi et al. 2010) (gray filled dots) and including the galaxies suffering an RPS event in the Virgo (red pentagons), Coma (green squares), A1367 (blue hexagons), and Norma (brown circles) clusters listed in Table 2. The cyan triangles indicate the jellyfish galaxies of the GASP survey extracted from Gullieuszik et al. (2020). The solid lines and the coloured segments delimit the different regions extracted from the simulations of Rhee et al. (2017) to identify galaxies in different phases of their infall into the cluster: first (not fallen yet - light blue), recent ($0 < \tau_{\text{inf}} < 3.6$ Gyr - light green), intermediate ($3.6 < \tau_{\text{inf}} < 6.5$ Gyr - orange), and ancient ($6.5 < \tau_{\text{inf}} < 13.7$ Gyr - red) infallers. Optical RGB images of four RPS galaxies at different positions on the phase diagram are also shown (image credits: ESO 137-001 and NGC 4921 — STScI; NGC 4569 — Boselli et al. 2016a; IC 5337 — Sunil Laudari with the HST data from the program 16223, PI: Gullieuszik). The white scalebar shows 10 kpc.

identify samples at different phases of their journey within the cluster, from their first infall, to their long term presence in the central virialised region, and can easily be compared to the predictions of cosmological simulations in the same observed parameter space (Oman et al. 2013; Oman & Hudson 2016; Sorce et al. 2016, 2019, 2021; Rhee et al. 2017; Arthur et al. 2019).

This exercise has been done in several nearby high-density regions (Mahajan et al. 2011b; Hernández-Fernández et al. 2014; Haines et al. 2015; Jaffé et al. 2015, 2018; Gavazzi et al. 2018b; Rhee et al. 2020; Wang et al. 2021), including Virgo (Vollmer et al. 2001b; Boselli et al. 2014d; Yoon et al. 2017; Morokuma-Matsui et al. 2021) and Fornax (Loni et al. 2021), and in high redshift clusters (Muzzin et al. 2014; Liu et al. 2021). We recall that while early-type galaxies are mainly virialised within the inner regions of high-density environments and have isotropic orbits, spiral galaxies have radial orbits with no significant evolution with redshift (Colless & Dunn 1996; Biviano & Poggianti 2009). The results of these works do not always agree. In the Virgo cluster, where galaxies suffering ram pressure have been clearly identified thanks to the excellent angular resolution of the data, the analysis of the phase space diagram suggests that the hydrodynamic interaction between the hot ICM and the cold ISM acts preferentially on fresh infalling systems rapidly strip-

ping the gas and quenching the activity of star formation on short timescales. Here the most perturbed galaxies, which have suffered the external perturbation on longer timescales, are located deep within the potential well of the cluster (Vollmer et al. 2001b; Boselli et al. 2014d; Yoon et al. 2017). Jaffé et al. (2018) also indicated that most of the jellyfish galaxies identified in the WINGS survey and targets of the MUSE GASP survey are located in the infalling regions, and thus have higher peculiar velocities than the other cluster members. A similar picture consistent with a rapid quenching of the star formation activity (see Sec. 4.2) in the infalling galaxies has been also claimed thanks to the statistical analysis of several nearby clusters by Mahajan et al. (2011b), Hernández-Fernández et al. (2014), Jaffé et al. (2015), and Oman & Hudson (2016), again consistent with a dominant RPS scenario at least within 1 – 2 virial radii of massive clusters. Longer timescales ($\tau \sim 1.7$ Gyr), on the contrary, suggesting a smooth decrease of the star formation activity as predicted by a starvation scenario, have been suggested by the analysis of other nearby clusters by Haines et al. (2015). The analysis of $z \sim 1$ clusters extracted from the GCLASS survey by Muzzin et al. (2014) indicates a delayed ($t_d \sim 2$ Gyr) then rapid ($\tau \sim 0.4$ Gyr) quenching of the star formation activity. As we discuss in Sec. 6.2 the delay time is shorter than the one derived for satellite galaxies in less dense environments (e.g. groups) suggesting some degree of dynamical gas removal in clusters also at these cosmic epochs.

4 The impact of RPS on galaxy evolution

4.1 Induced effects on the star formation process

The suppression of gas removed during the interaction has heavy consequences on the future evolution of the perturbed galaxies. The main gas component removed during a RPS event is the diffuse atomic gas reservoir distributed on an extended disc. The one located within the stellar disc, which is the principal supplier of giant molecular clouds where star formation takes place, is only moderately or indirectly affected by the interaction¹⁴. Whenever this occurs, the decrease of the atomic and molecular gas components in the inner regions, (the former partly swept away during the interaction, the latter gradually exhausted by the lack of feeding from the atomic gas reservoir), induce a decrease of the star formation activity, as indeed observed in the large majority of the HI-deficient galaxies in nearby clusters (e.g. Kennicutt 1983; Gavazzi et al. 1991, 1998, 2002, 2006a, 2013b; Donas et al. 1990, 1995; Moss & Whittle 1993; Haines et al. 2007, 2009; Vulcani et al. 2010; Boselli et al. 2014d; Cybulski et al. 2014) and groups (Hu et al. 2021). Within the Virgo

¹⁴ Infall of the HI gas located in the outer regions to the inner disc has been invoked to explain the observed strong correlation between the total gas content (HI plus H₂) of isolated late-type galaxies, a large fraction of which is located outside the stellar disc, and their overall star formation activity (Boselli et al. 2001). The supply of this gas component to the inner star forming regions, however, would occur on timescales relatively long compared to the typical ones for gas stripping (see Sec. 4.2).

cluster, the radial dependence of the specific star formation activity with clustercentric distance perfectly matches that of the increase of the HI-deficiency parameter, which starts to systematically change from that of unperturbed field objects at projected $R/r_{200} \lesssim 1-2$ (Gavazzi et al. 2013b). We recall that this clustercentric distance measured in Virgo also corresponds to that of the decrease of the star formation activity observed in large statistical samples extracted from the 2dF (Lewis et al. 2002) and SDSS (Gómez et al. 2003) surveys, as described in Sec. 3.7. The overall decrease of the star formation activity put HI-deficient galaxies below the main sequence relation traced by unperturbed field objects (see Fig. 12; (Boselli et al. 2015, 2016b; Ciesla et al. 2016), or in the green valley when colour indices including a UV band, sensitive to the youngest stellar populations, are used in the definition of the colour-magnitude or colour-stellar mass relation (e.g. Hughes & Cortese 2009; Cortese & Hughes 2009; Boselli et al. 2014b,d). In the Virgo cluster, the spatial distribution of HI-deficient late-type galaxies with reduced star formation activity (red $NUV - i$ colours) seems fairly correlated with the distribution of the hot gas emitting in X-rays (Cayatte et al. 1990; Chung et al. 2009a; Boselli et al. 2014d).

As described in Sec. 3.4, ram pressure removes the gas outside-in, forming truncated gas discs whose radial extension decreases at the increasing of the HI-deficiency parameter, thus in those galaxies located closer to the cluster core. As a consequence, the star formation activity of the perturbed galaxies mainly decreases in the outer disc, but there are some cases where it is also reduced in the inner disc as deduced by a lower $H\alpha$ surface brightness with respect to similar objects in the field (Koopmann & Kenney 2004a). The decrease of the star formation activity might be drastic in dwarf systems, where the shallow gravitational potential well is not sufficient to keep the cold gas anchored to the stellar disc. Gas rich, low mass systems can thus be transformed in quiescent dwarf ellipticals in relatively short timescales (Haines et al. 2007; Boselli et al. 2008a,b; Boselli & Gavazzi 2014; Toloba et al. 2009, 2011, 2012, 2015; Smith et al. 2012b; Mahajan et al. 2011a; Janz et al. 2021; Junais et al. 2021). In a few objects, some ISM is retained only in the nucleus, where the gravitational potential well is at its maximum (Boselli et al. 2008a; De Looze et al. 2010; Boselli et al. 2014d). Here star formation can continue at small rates (Boselli et al. 2008a) and possible be at the origin of the blue nuclei observed in the most massive dwarf ellipticals within the Virgo cluster (Lisker et al. 2006).

Under some conditions, however, the RPS process can boost the overall activity of star formation and bring galaxies above the main sequence, as indeed suggested by several simulations (Fujita et al. 1999; Bekki & Couch 2003; Bekki 2014; Steinhauser et al. 2012, 2016; Henderson & Bekki 2016; Steyrleithner et al. 2020; Lee et al. 2020; Troncoso-Iribarren et al. 2020) (see Fig. 12). A systematic enhancement of the star formation activity of local cluster galaxies has been looked for using data gathered during several blind surveys, but never convincingly shown so far (Donas et al. 1990, 1995; Moss & Whittle 1993; Mahajan et al. 2012). There are, however, clear examples of galaxies with an

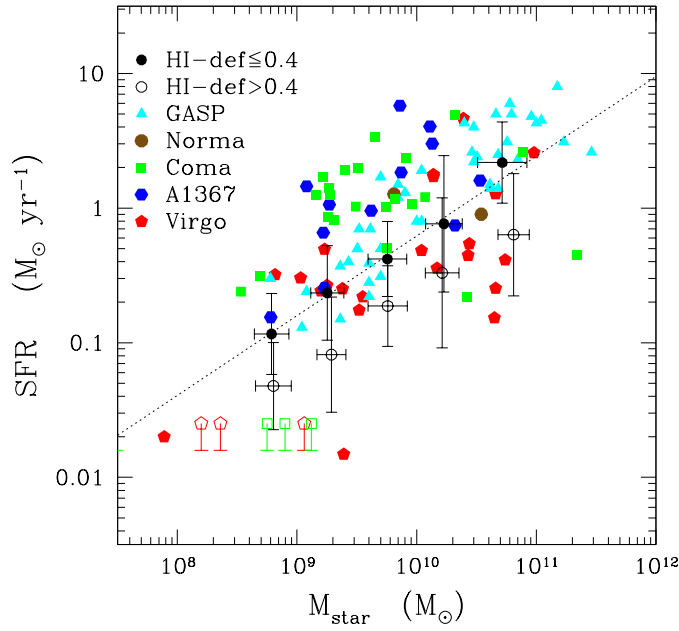


Fig. 12 Relationship between the star formation rate and the stellar mass (main sequence) for galaxies suffering an RPS event listed in Table 2 or extracted from the GASP sample compared to the mean main sequence relation extracted from the *Herschel* Reference Survey for HI-normal (black filled dots) and HI-deficient (black empty circles) galaxies (Boselli et al. 2015). For the GASP sample (cyan filled triangles), data have been extracted from the compilation of Vulcani et al. (2018), while for the Virgo cluster (red pentagons) from Boselli et al. (2015) or from the VESTIGE survey. Those for Coma (green squares), A1367 (blue exagons), and Norma (brown circles) have been measured from $H\alpha$ fluxes available in the literature (from dedicated MUSE papers when available, as indicated in Table 2, or from (Gavazzi et al. 2015) and references therein) corrected for dust attenuation and [NII] contamination (whenever necessary) consistently with Boselli et al. (2015). Empty red pentagons and green squares are for those galaxies with clear $H\alpha$ extended tails but with no emission in the disc as seen in the deep VESTIGE (Boselli et al. 2018c) or Subaru (Yagi et al. 2010) narrow-band $H\alpha$ images. The black dotted line gives the best fit to the *Herschel* Reference Survey for HI-normal galaxies (unperturbed reference sample). Stellar masses and star formation rates have been estimated assuming a Chabrier IMF. Adapted from Boselli et al. (in prep.).

enhanced activity such as the jellyfish galaxies observed during the GASP survey (Vulcani et al. 2018) (cyan filled triangles in Fig 12). Other examples are the blue cluster galaxies discovered by Bothun & Dressler (1986), whose spectroscopic properties (presence of strong emission and absorption Balmer lines) suggest a recent enhanced star formation activity (some of these are indicated as green filled squares in Fig. 12). Representative RPS galaxies with enhanced star formation activities are also UGC 6697, CGCG 097-073 and CGCG 097-079 at the periphery of the cluster A1367 (Gavazzi et al. 1995, 2001a; Boselli et al. 1994; Scott et al. 2015; Consolandi et al. 2017) (blue filled pentagons in Fig 12). On the leading-edge opposite to the observed radio continuum tail

these galaxies have a bow-shocked structure of star forming complexes probably formed after the interaction. Another spectacular case is IC 3476 in the Virgo cluster (Boselli et al. 2021). Despite a marked HI-deficiency ($HI - def = 0.67$), the galaxy is located in the upper envelop of the main sequence drawn from unperturbed isolated systems (see Fig. 12). The exquisite quality of the $H\alpha$ narrow-band imaging gathered during the VESTIGE survey indicates that giant H II regions are formed on the leading side of the disc, at the interface between the stripped ISM and the surrounding ICM. Here, the observed increase of the star formation seems due to the compression of the gas which induces an increase of its mean electron density (Boselli et al. 2021) and probably of the molecular gas phase, as indeed observed in a few other Virgo galaxies (Nehlig et al. 2016; Lizée et al. 2021). Tuned simulations suggest that the overall increase of the star formation activity of these objects is mainly localised in this front region, but also show that any bursting phase generally lasts only a few tens of million years (Weinberg 2014; Troncoso-Iribarren et al. 2020). The origin of this burst, as those observed in the galaxies mentioned above, can be due to the inclination angle of the infalling galaxies, all entering the cluster mainly edge-on, as indeed indicated by tuned simulations (Safarzadeh & Loeb 2019). In this particular configuration, most of the stripped gas has to cross the stellar disc before leaving the galaxy, creating turbulences and instabilities which favour gas collapse and star formation (Lee et al. 2020; Boselli et al. 2021). The perturbed galaxies with an enhanced star formation activity located above the main sequence might thus be perturbed systems representative of a particular short living phase of the ram pressure stripped population, while the quiescent population associated to the gas deficiency the following long living phase, as suggested by models (Boselli et al. 2006, 2008a, 2014d). The excellent quality of the VESTIGE data in terms of angular resolution ($\simeq 50$ pc) and sensitivity ($L(H\alpha) \sim 10^{36}$ erg s $^{-1}$) also allowed to extend the study the effects of RPS down to the scale of individual H II regions (Boselli et al. 2020). This analysis has shown that the HI-deficient galaxies have, on average a lower number of H II regions with respect to similar gas-rich objects. It has also shown that H II regions are mainly lacking in the outer disc, thus consistent with an outside-in truncation of the star formation activity as expected in an RPS scenario (Koopmann & Kenney 2004b; Boselli et al. 2020).

4.2 Timescales for stripping and quenching

The different perturbing mechanisms affecting galaxies in high density environments act on different timescales for the gas removal, and thus have different effects on the star formation activity of the perturbed objects. The typical timescale for RPS to be efficient has been derived using semi-analytical models and full or zoomed-in hydrodynamic cosmological simulations of rich clusters of galaxies (Abadi et al. 1999; Balogh et al. 2000; Quilis et al. 2000; Mori & Burkert 2000; Schulz & Struck 2001; Marcolini et al. 2003; Tonnesen et al. 2007; Roediger & Brüggén 2007; Marasco et al. 2016; Trayford et al. 2016; Lotz

et al. 2019; Pallero et al. 2022) or tuned simulations of selected objects with multifrequency data consistently indicating that they are undergoing a stripping event (Vollmer 2003; Vollmer & Huchtmeier 2003; Vollmer et al. 2004a, 2005b, 2006, 2008a,b, 2009, 2012, 2021; Boselli et al. 2021). 3-D hydrodynamic simulations suggest that a large fraction of the total gas reservoir (Abadi et al. 1999; Quilis et al. 2000; Schulz & Struck 2001; Tonnesen et al. 2007; Roediger & Brüggén 2007; Lotz et al. 2019) can be efficiently stripped on relatively short timescales ($\lesssim 1$ Gyr) compared to the typical crossing time within a cluster (~ 2 Gyr; see however Bahé & McCarthy (2015)). This is particularly true in dwarf systems, where the shallow gravitational potential well hardly keeps the gas anchored to the stellar disc (Mori & Burkert 2000; Marcolini et al. 2003). For these low mass objects the typical timescale for gas stripping can be of ~ 100 -200 Myr. Simulations based on a single and homogeneous gas phase such as these, however, generally underestimate the efficiency of RPS, suggesting that these timescales could even be overestimated (Tonnesen & Bryan 2009).

Observationally, these timescales can be estimated by reconstructing the star formation history of the perturbed galaxies through the analysis of their stellar population (quenching episode). Statistically, this has been done by comparing the star formation history of cluster galaxies (reconstructed from multifrequency datasets) with that predicted by cosmological simulations or semi-analytic models of galaxy evolution. The outside-in truncation of the gaseous disc of RPS galaxies gradually quenches the activity of star formation in the outer regions, inverting the typical colour gradients of spiral systems which generally gets bluer in the outer disc. The UV photometric bands, most sensitive to the youngest stellar populations, are those which become redder first after the stripping of the gas has been completed (Crowl & Kenney 2006). The comparison of the light profiles in different photometric bands with the predictions of spatially resolved models of gas stripping can thus be used to estimate the typical timescale for the quenching of the star formation activity. This experiment has been successfully done for the first time on the spiral galaxy NGC 4569 in Virgo (Boselli et al. 2006), and led to the conclusion that the cold gas content and the star formation activity of this ram pressure stripped galaxy, as indicated by the presence of a long cometary tail of ionised gas (Boselli et al. 2016a), have been reduced by $\sim 95\%$ in about 100 Myr (Boselli et al. 2006). This short timescale is consistent with the one derived by Vollmer et al. (2004a) (~ 300 Myr) by comparing the kinematical properties of the perturbed gas with those derived from tuned hydrodynamic simulations. Since then, several works have tried to estimate the typical timescale for star formation quenching in representative RPS galaxies (Pappalardo et al. 2010; Abramson et al. 2011; Fossati et al. 2018; Boselli et al. 2018b,a, 2021; Vollmer et al. 2018; Vulcani et al. 2020) or in larger statistical samples (Crowl & Kenney 2008; Boselli et al. 2008a, 2014d, 2016b; Smith et al. 2012b; Wetzel et al. 2013; Haines et al. 2015; Ciesla et al. 2016; Owers et al. 2019; Gallazzi et al. 2021). The most recent used SED fitting techniques on FUV-to-FIR photometric data with the purpose of removing any possible degeneracy related to the reddening of the stellar population, which might result from either an ageing of the

stellar population or an increasing dust attenuation (Ciesla et al. 2016; Boselli et al. 2016b). The most recent SED fitting codes are now able to combine photometric with spectroscopic data, these last important since they include age-sensitive Balmer absorption lines (Poggianti & Barbaro 1997). Whenever the star formation quenching episode needs to be dated with a time resolution < 100 Myr, the use of the Balmer emission lines such as $H\alpha$ (λ 6563 Å) or $H\beta$ (λ 4861 Å) becomes critical (Boselli et al. 2016b; Fossati et al. 2018), if combined with UV photometric bands. Indeed, these lines are due to the emission of the gas ionised in H II regions by O-early B stars, whose typical age is $\lesssim 10$ Myr (Kennicutt 1998; Boselli et al. 2009). The short quenching timescales derived from the analysis of the stellar population is consistent with the observed orientation of the ionised gas tails of perturbed galaxies in local and $z \sim 0.25$ clusters, which are mainly pointing away from the cluster centres, suggesting a rapid stripping and quenching process occurring during the first infall within the cluster potential (Yagi et al. 2010, 2017; Gavazzi et al. 2018b; Liu et al. 2021).

Donnari et al. (2021) using data from the IllustrisTNG simulations revealed a great diversity of quenching pathways for satellite galaxies found in $z = 0$ clusters. Satellites can quench before infall in dense environments or after being accreted into groups (pre-processing) or in the host where they currently reside. The frequency of each quenching track depends on the satellite stellar mass and the host halo mass. As a result, the timescales derived using SED fitting analysis of a large sample of galaxies in the Virgo cluster, which indicate a rapid evolution, suggest that RPS is the dominant perturbing mechanism in clusters (Boselli et al. 2016b; Oman & Hudson 2016) but its effects become less prominent when larger populations of satellites are considered. A consistent result is given by the analysis of a sample of 11 massive early-type galaxies in the Coma cluster with high signal-to-noise spectra carried on by Upadhyay et al. (2021). By studying the variation of their star formation activity as a function of their orbital parameters as derived from tuned simulations, the authors concluded that in these objects the activity of star formation ceased ~ 1 Gyr after their first pericentre passage. They ascribed this rapid quenching to RPS possibly combined with tidal interactions.

4.3 Nuclear activity

The recent discovery by the GASP survey that a large fraction of jellyfish galaxies host an AGN (optical definition based on emission line diagnostics Poggianti et al. 2017a) raised a new interesting question on the interplay between RPS and the triggering of nuclear activity. In this scenario, the AGN feedback could efficiently combine with ram pressure to expel the gas from the galaxy disc and quench the activity of star formation (George et al. 2019; Radovich et al. 2019). Theoretical considerations and simulations consistently suggest that during the stripping process the external perturbation can induce a loss of angular momentum of the gas in the disc that could fall in the in-

ner regions and feed the nuclear activity (Schulz & Struck 2001; Tonnesen & Bryan 2009; Ramos-Martínez et al. 2018). Other cosmological hydrodynamical simulations also show no signs of enhanced AGN activity in massive ($M_{\text{star}} > 10^{10.7} M_{\odot}$) galaxies infalling in high mass clusters, where the activity of star formation is also significantly reduced during an RPS event (Lotz et al. 2021).

In Poggianti et al. (2017a), the evidence of an increase of the fraction of galaxies hosting an AGN in jellyfish galaxies is based on a very limited sample of galaxies (5 objects out of 7 observed) and thus might be uncertain due to the low number statistics. Peluso et al. (2021) extended this analysis in sample size and stellar mass range finding that the AGN fraction drops to 24% if a sample of 82 objects at $M_{\text{star}} > 10^9 M_{\odot}$ is considered while it is 80% in a sample of 15 high mass galaxies ($M_{\text{star}} > 10^{10.5} M_{\odot}$). These authors, however, include as AGNs also LINERs, which are known not to always correspond to accreting super massive black holes in the galaxy centres (see e.g. Belfiore et al. 2016). However, several observational results do not seem to confirm this result. The analysis of the cluster A901/2 at $z=0.165$ carried on with H α GTC and ACS HST imaging by Roman-Oliveira et al. (2019) has clearly shown that, among the 70 jellyfish candidates with a stellar mass $10^9 \leq M_{\text{star}} \leq 10^{11.5} M_{\odot}$, the majority are star forming systems (53) and only 5 probably host an AGN (defined using optical line diagnostics). In these five AGN candidates the nuclear activity does not seem to be correlated with the presence of extended tails. In local clusters such as Coma, A1367, and Virgo, where the large sets of multifrequency data acquired during several complete, blind surveys allowed the identification of relatively complete sets of galaxies currently undergoing an RPS event. Indeed, as summarised in Table 2, the fraction of late-type systems suffering an RPS event and at the same time hosting an AGN is 3% (2/70) and increases to 14% (10/70) when LINERs are included. The BPT classification adopted is the same used in Poggianti et al. (2017a) and is based on the Kewley et al. (2001) and Kauffmann et al. (2003) thresholds to divide star formation from AGN ionisation. The sample from Table 2 is divided into four stellar mass bins with the highest mass bin corresponding to the range probed by Poggianti et al. (2017a), and the AGN fraction is shown by the red points with Binomial uncertainties in Figure 13. To accurately compare to the general galaxy population we randomly select a mass matched sample from a complete local Universe catalogue (G.Gavazzi private comm.), with RPS galaxies removed. Bootstrap resampling statistics shows that across all the four stellar mass bins there is no excess of AGNs in RPS galaxies compared to the general galaxy population.

An increase of the AGN fraction in ram pressure stripped galaxies seems also at odd with the analysis of large statistical samples extracted from the SDSS survey which rather indicate a decrease of the AGN fraction with galaxy density (Kauffmann et al. 2004) and that while Seyfert galaxies are less clustered than normal galaxies, LINERs follow a similar distribution (Constantin & Vogeley 2006). More recent works aimed at studying the incidence of AGNs in different environments, despite the uncertainty introduced by different selection criteria (optical emission lines, radio emission, or X-rays data) or by

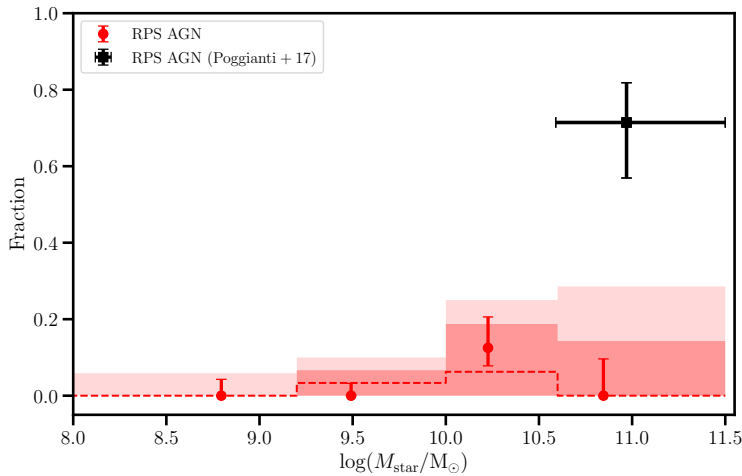


Fig. 13 Fraction of RPS galaxies from Table 2 with an AGN. The fraction of AGN in the RPS sample from Poggianti et al. (2017a) is also shown. The dashed lines show the median fraction of galaxies with AGNs from a bootstrap mass matched sample of a local galaxy catalogue (G.Gavazzi private comm.). The dark and light shaded areas show the boundaries of the 1σ and 2σ confidence levels, respectively.

a different definition of the environment, appear to agree that the fraction of AGNs decreases towards the inner parts of high density regions, from clusters to groups (AGN selected from optical line ratios, and excluding LINERs Sabater et al. 2013, 2015; Lopes et al. 2017; Li et al. 2019a), (X-rays selected AGNs Ehlert et al. 2014, 2015; Koulouridis et al. 2018; Mishra & Dai 2020). The observed decrease of the AGN fraction in star forming systems towards the centre of rich clusters of galaxies is interpreted as due to a lack of cold gas available to feed the nuclear activity (Sabater et al. 2013). A statistical reduction of the cold gas content in samples of these objects is likely due to RPS, leading to the conclusion that ram pressure generally inhibits rather than increases the AGN activity. A possible increase of the AGN activity is present in the infalling regions of low mass clusters and massive groups (spectroscopically selected AGN, Pimblet et al. 2013; Gordon et al. 2018); (X-rays selected but spectroscopically confirmed AGN, Koulouridis et al. 2018), or in low mass groups (spectroscopically selected AGN, Manzer & De Robertis 2014). Such an increase is rather interpreted as due to the gravitational perturbations acting on the infalling systems (pre-processing). The relative close position within infalling groups, combined with their low velocity dispersion, give enough time to the infalling galaxies to be tidally perturbed, fuelling the gas towards the inner regions, and thus feeding the nuclear activity (Manzer & De Robertis 2014; Gordon et al. 2018; Koulouridis et al. 2018).

How can the GASP results be then explained? The first possible interpretation is that the jellyfish galaxies observed by the GASP survey are only a

small fraction of the galaxies undergoing an RPS event, possibly those where the interaction with the surrounding ICM is mainly edge-on. In this geometrical configuration, the gas located in the outer regions is pushed along the disc before being totally stripped from the parent galaxy (Consolandi et al. 2017; Boselli et al. 2021). It can thus be partly accreted by the nucleus. A second possible interpretation is that the peculiar morphology of these jellyfish galaxies is not (only) due to an RPS event, but also to gravitational perturbations (see Sec. 3.3), which could create strong instabilities able to fuel the cold gas of the disc towards the centre (e.g. Lake et al. 1998).

An interesting related question is the possible contribution of the nuclear activity via feedback to the quenching episode that follows the stripping of the gas. A detailed analysis of NGC 4569, a massive late-type galaxy in the Virgo cluster hosting a nuclear starburst or a weak AGN as derived from X-rays observations, and optically classified as a LINER, revealed that the quantity of gas expelled by the nuclear outflow is only a very small fraction of that removed by the RPS phenomenon (Boselli et al. 2016a). On the contrary, the lack of molecular gas observed in the central regions of the massive jellyfish galaxy JO201 suggests that the suppression of the star formation activity in these regions could mainly be driven by the feedback from a relatively strong AGN (George et al. 2019).

4.4 Gas and stellar kinematics

RPS acts on the gaseous component of the late-type galaxies infalling for the first time into rich clusters. It is thus conceivable that, along with its distribution, the kinematical properties of the gas are also affected during the perturbation. This is indeed predicted by hydrodynamic simulations of galaxies suffering an RPS event (Schulz & Struck 2001; Hidaka & Sofue 2002; Kronberger et al. 2008b; Smith et al. 2012a; Haan & Braun 2014). The interaction is expected to displace the kinematical centre of the rotating gas with respect to that of the unperturbed stars, change the shape of its rotation curve and modify the velocity field mainly in the outer regions where the gas is only weakly bound to the gravitational potential well of the galaxy (Kronberger et al. 2008b; Bellhouse et al. 2021), while producing on long terms warps (Haan & Braun 2014). The degree of the perturbations and the effects on the rotation curve depend on the impact angle and are more important in nearly edge-on interactions, but are generally less pronounced than in those due to tidal interactions (Kronberger et al. 2008b). The first systematic study of the kinematical properties of the ionised gas of cluster perturbed galaxies is the work of Rubin et al. (1988) suggesting modified rotation curves in RPS galaxies. Since then, a major improvement in the observational data has been gathered thanks to IFU spectroscopy able to probe at the same time the gas and stellar 2D-kinematics whenever the stellar continuum is sampled. Optical IFU spectroscopy, which now has the required sensitivity, angular, and spectral resolution to reconstruct the detailed velocity field of nearby perturbed

galaxies, confirmed this picture. The first clear evidence of gas perturbed velocity fields in a statistically representative sample of ram pressure stripped galaxies comes from the Fabry-Perot spectroscopic observations of a large sample of late-type galaxies in the Virgo cluster (Chemin et al. 2006). This work confirmed previous claims of a modified velocity field discovered using radio interferometry in NGC 4522 (Kenney et al. 2004) and later detected in another Virgo cluster object NGC 4330 still using HI data (Abramson et al. 2011). Systematic differences between the gas and stellar velocity field in a galaxy suffering an RPS event in the cluster A3558 in the Shapley supercluster have been shown by Merluzzi et al. (2013). This object has a complex gas velocity field, with the extraplanar gas showing signs of rotation up to 13 kpc from the stellar disc (projected distance), while the stellar velocity field is uniform and symmetric. Another interesting example of galaxy suffering an RPS event with a peculiar kinematics is an object in Abell 2670. This object, which has an elliptical morphology, is characterised by an extended ionised gas tail with a significant rotation, without a stellar component (Sheen et al. 2017). The IFU observations of ESO 137-001 (Fumagalli et al. 2014), UGC 6697 (Consolandi et al. 2017), and NGC 4330 (Sardaneta et al. 2022), suggest that the gas conserves its rotation close the galactic disc. The rotation velocity decreases with increasing distance from the galaxy disc where the gas becomes more turbulent. Further evidence for a perturbed velocity field of the gaseous component comes from the MUSE and Fabry-Perot observations of the galaxy IC 3476 in the nearby Virgo cluster, where the angular resolution of the instruments and the low distance of the cluster allow to resolve the different components down to scales of ~ 100 pc (Boselli et al. 2021). The perturbation, which here is acting almost edge-on ($\simeq 70$ deg. from face-on), has displaced the gas kinematical centre from that of the unperturbed stars by ~ 500 pc along the direction of the motion of the galaxy within the cluster on timescales of the order of 50 Myr. It has also changed the mean velocity of the gas with respect to that of the stars in each position along the disc by ~ 20 km s $^{-1}$. All this observational evidence has been reproduced by tuned hydrodynamic simulations for a galaxy with similar properties undergoing an RPS event (Boselli et al. 2021). Another interesting case is the edge-on late-type galaxy NGC 4330 in the Virgo cluster, where the stripping process, which acts mainly face-on, allows us to study the effects of the perturbation along the z -axis. Fabry-Perot observations have shown a decrease of the rotational velocity of the stripped gas with increasing distance from the disc plane, suggesting a gradual but not linear loss of angular momentum (Sardaneta et al. 2022). It is also worth mentioning that tuned simulations of RPS events indicates that the velocity of the stripped gas can be lowered close to the stellar disc and increased far away in the presence of magnetic fields (Tonnesen & Stone 2014). By reconstructing the kinematical properties of the gas in perturbed systems using tuned N-body simulations, Vollmer and collaborators were able to estimate the epoch of the first interaction of these objects with the surrounding ICM and thus pose strong constraints on the time required by an RPS event to remove the cold gas component (Vollmer et al. 1999, 2000, 2001a, 2004a,

2005b, 2006, 2008a,b, 2009, 2012, 2018, 2021). These works also showed for the first time that part of the stripped gas can fall back on the stellar disc once the galaxy has passed the peak of the interaction (Vollmer et al. 2001b; Steyrleithner et al. 2020).

Other simulations, however, indicate that while ram pressure pushes the gas outside the stellar disc, the drag force exerted by this gas on the dark matter component is able to modify the gravitational potential well, moving the position of the dynamical centre of the perturbed galaxy by several kpc (Smith et al. 2012a). For this reason, also the stellar velocity field would be modified during the interaction. For the same reason, the perturbation would also thicken the stellar disc by a factor of ~ 2 mainly in the outer regions where most of the gas can be stripped, consistently with simulations (Farouki & Shapiro 1980; Clarke et al. 2017; Safarzadeh & Scannapieco 2017; Steyrleithner et al. 2020). A boxy shape in the outer disc probably resulting from the induced perturbation in the stellar orbits has been observed in the edge-on spiral galaxy NGC 4330 in the Virgo cluster which is suffering a RPS event as suggested by the presence of extended tails of ionised gas (Sardaneta et al. 2022). Using different arguments, a thickening of the stellar disc has been also invoked by Boselli et al. (2008a,b) to explain the formation of dwarf ellipticals in clusters. Indeed, the lack of cold gas which in dwarfs is rapidly stripped during the interaction (Mori & Burkert 2000; Marcolini et al. 2003) prevents the formation of new stars on the stellar disc. Since young stars are formed within a thin layer of cold gas, they have a low velocity dispersion. The lack of this newly formed stellar population induces an instability in the stellar disc which heats up, dumping spiral waves on a few revolutions (Sellwood & Carlberg 1984; Fuchs & von Linden 1998; Elmegreen et al. 2002; Bekki et al. 2002). This effect is expected to be more important in dwarf systems, where most of the gas can be easily removed during the interaction and where the velocity rotation of the disc is relatively low. Indeed, in low-luminosity systems the scale-height of the disc increases by a factor of ~ 2 in ~ 3 Gyr (Seth et al. 2005). This mechanism could explain the properties of dwarf ellipticals in clusters if they were formed after an RPS event able to remove on short timescales their gas content from the disc. In this picture, the flattening of their disc could be anti-correlated to the age of the perturbation. It is worth mentioning that this process would increase the velocity dispersion of the stellar component while conserving its angular momentum (Steyrleithner et al. 2020). This picture is also consistent with the evidence that several dE galaxies in the Virgo cluster are rotating systems, and that their v/σ ratio or λ_R is higher in those systems located at the periphery of the cluster and characterised by a young stellar population (Toloba et al. 2009, 2011, 2012, 2015; Boselli et al. 2014d; Bidaran et al. 2020). This result is in agreement with the evidence that satellite galaxies have, at fixed stellar mass and ellipticity, lower values of v/σ than similar main sequence objects in the field (Cortese et al. 2019). This observed decrease of the spin parameter of satellites is mainly due to satellite galaxies which have already reached the red sequence.

5 The impact of RPS on the surrounding environment

5.1 The fate of the stripped gas

As soon as a galaxy becomes satellite of a larger structure, its halo, which is principally composed of hot gas, gets mixed with the hot gas trapped within the gravitational potential well of the central system. The hot halo of the galaxy is not available any more for supplying gas to the disc, reducing at long timescales the activity of star formation in the satellite. This mild phenomenon is generally called starvation or strangulation (e.g. Larson et al. 1980; Bekki et al. 2002; van den Bosch et al. 2008). Ram pressure, which is a more violent process, adds up to this effects and removes the cold gas from the disc. As mentioned in Sec. 3.1, the gas phase which is most efficiently removed is the atomic one, since located on a disc extending far out from the stellar disc, where the gravitational potential well of the galaxy is shallow. It is thus interesting to understand what is the fate of the stripped gas.

We can first notice that the perturbed gas can definitely leave the galaxy only if it overcomes the gravitational forces keeping it bound to the disc, i.e. if the velocity of the gas overcomes the escape velocity from the galaxy, which for a spherically symmetric solid body is given by the relation:

$$v_e = \sqrt{\frac{2GM_{\text{DM}}}{r_{\text{gas}}}} \quad (45)$$

where M_{DM} is the total mass of dark matter of the perturbed galaxy and r_{gas} is the distance of the gas from the galaxy. Whenever this condition is not satisfied, once the galaxy gets to the apocentre of its orbit, where the external pressure on its ISM is significantly reduced, the stripped gas can fall back on the disc (e.g. Vollmer et al. 2001b; Roediger & Hensler 2005; Boselli et al. 2018b; Steyrleithner et al. 2020; Cramer et al. 2021). If removed from the galaxy, the gas gets mixed with the surrounding hot gas, where it can be heated and change phase, than becoming part of the ICM. The change of phase in the stripped gas is now commonly observed in ram pressure stripped tails, as mentioned in Sec. 3.2.4. Indeed these tails have been seen in cold atomic gas, in molecular gas through different molecular transitions (see Sec. 3.2.3), witnessing thus a different gas density and temperature, in ionised and hot gas, this last with temperatures generally lower than those typically observed in the surrounding ICM (see Sec. 3.2.5).

Different mechanisms have been proposed to explain the change of phase of the stripped gas. These includes shocks in the instabilities at the interface of the cold ISM and the hot ICM formed during the journey of the galaxy within the cluster (e.g. Nulsen 1982; Roediger et al. 2006; Roediger & Brüggen 2008; Tonnesen & Bryan 2009, 2010; Tonnesen et al. 2011; Poggianti et al. 2019b), thermal evaporation and mixing (e.g. Cowie & Songaila 1977), magneto-hydrodynamic waves (e.g. Tonnesen & Stone 2014; Ruszkowski et al. 2014; Vijayaraghavan & Ricker 2015), and photoionisation by young stars

formed in the stripped tails (see Sec. 3.3). All these physical mechanisms are now explored in the most recent hydrodynamic simulations which began to reproduce some observed properties of the different gas phases in the tails. There are, however, several observational results which remains unexplained. For instance, it is still unclear why the tails are rarely seen in all the different gas phases at the same time, or why star formation occurs in some of them why not in others. The reasons behind these still unexplained results are manifold. First, they can depend on the properties of the surrounding medium (gas temperature and pressure (Tonnesen et al. 2011), two radially dependent variables which might affect the typical timescales for the gas change of phase), on the impact parameter of the galaxies with the hot ICM (which might differently favor the formation of turbulent regions where the gas can collapse to form giant molecular clouds), or on the progression with time of the gas stripping process (which might act on different components of the ISM working this mechanism outside-in). Moreover, other complex physical processes can shape the morphology and physical conditions of the tails, including but not limited to the presence of magnetic fields, shocks, and instabilities.

5.1.1 Gas evaporation

To understand whether RPS is the dominant mechanism affecting the late-type population in these environments we have to quantify the fraction of galaxies which are now undergoing or underwent this perturbation. Truncated gaseous discs combined with unaffected stellar discs are a clear sign of a past RPS event. If the typical timescale for gas evaporation is short, as suggested by the low fraction of H I tails observed in nearby clusters, these tails are short lived phenomena and rather indicate an ongoing perturbation. This evidence also suggests that the H I gas, once stripped, changes of phase while mixing with the surrounding ICM. How does this gas phase transformation occurs? The typical timescale for gas evaporation can be measured using different approaches. The total H I mass in the tail can be first compared to the lacking mass of H I over the disc of the galaxy by mean of the H I-deficiency parameter (Haynes & Giovanelli 1984). Derived from different mean scaling relations in field objects, the H I-deficiency parameters gives the difference in logarithmic scale between the expected and the observed total mass of H I that a galaxy of given type, size, or luminosity has with respect to similar objects in the field. Recent calibrations of this relation are given in (Boselli & Gavazzi 2009). The lacking mass of H I can be compared to that observed in the tail to see whether all the stripped H I gas is still there (see for an example Boselli et al. (2016a)). The mass, the column density, and the volume density of the H I gas can be directly measured from the H I observations, the latter making simple assumptions on the 3D geometrical distribution of the gas within the tail. The largest uncertainty in these estimates is the clumpiness of the gas leading to a very uncertain volume filling factor.

In the case that the time since the beginning of the interaction τ_{RPS} is known, as for instance derived from simulations, models, or from SED fitting

analysis as described in the next sections, these data can be used to estimate an evaporation rate (Vollmer & Huchtmeier 2007):

$$\dot{M}_{\text{evap}} \sim \frac{(M_{\text{expected}} - M_{\text{observed}})}{\tau_{\text{RPS}}} \quad [\text{M}_{\odot}\text{yr}^{-1}] \quad (46)$$

As suggested by Vollmer & Huchtmeier (2007), this estimate can be compared to that derived from the evaporation rate of a spherical gas cloud (Cowie & McKee 1977):

$$\dot{M}_{\text{evap}}^{\text{sphere}} = 1.74 \times 10^{-3} \left(\frac{T_{\text{ICM}}}{3 \times 10^7 \text{K}} \right)^{5/2} \left(\frac{r}{\text{pc}} \right) \left(\frac{37}{\ln \Lambda} \right) \quad [\text{M}_{\odot}\text{yr}^{-1}] \quad (47)$$

where r is the cloud radius and T_{ICM} is the ICM temperature and $\ln \Lambda$ is the Coulomb logarithm. Noticing this mass loss rate is proportional to the cloud radius, one can analytically solve the evaporation timescale of this spherical cloud:

$$\tau_{\text{evap}}^{\text{sphere}} = 2.5 \times 10^6 \left(\frac{\bar{n}_{\text{H}}}{1 \text{cm}^{-3}} \right) \left(\frac{T_{\text{ICM}}}{3 \times 10^7 \text{K}} \right)^{-5/2} \left(\frac{r}{100 \text{pc}} \right)^2 \left(\frac{\ln \Lambda}{37} \right) \quad [\text{yr}] \quad (48)$$

where \bar{n}_{H} is the average hydrogen number density of the cloud. We also include a factor of 1.4 on the total cloud mass from He and other heavy elements. This timescale¹⁵ is typically less than 100 Myr for galactic clouds, e.g., an H I cloud with a radius of 500 pc (corresponding to the scale height of a galaxy disc) and an average density of 1 cm^{-3} , or a molecular cloud with a radius of 50 pc and an average density of 10^2 cm^{-3} . Similarly, Vollmer & Huchtmeier (2007) estimated that the evaporation rate $\dot{M}_{\text{evap}}^{\text{sphere}} \sim 1 \text{ M}_{\odot} \text{ yr}^{-1}$, which for a tail composed of ~ 1000 similar clouds with a given geometric form where 10% of the surface of the spheres is surrounded by the hot ICM, the total evaporation rate of the tail is $\dot{M}_{\text{evap}}^{\text{tail}} \sim 100 \text{ M}_{\odot} \text{ yr}^{-1}$. If the mass of the gas in the tail M_{tail} is known (measured as described above from the HI-deficiency parameter, from a direct measure, or simply assuming that the mean density of the gas within the spheres is $n = 1 \text{ cm}^{-3}$), this quantity can be used to estimate the typical timescale for evaporation once the cold gas in the tail get in contact with the hot ICM. For a typical tail of mass $M_{\text{tail}} \sim 10^9 \text{ M}_{\odot}$, this leads to an evaporation timescale of $\tau_{\text{evap}} \sim 10 \text{ Myr}$, a relatively short timescale compared to the typical crossing time of a cluster ($\sim 2 \text{ Gyr}$, Boselli & Gavazzi (2006)). With a typical velocity within the cluster of $\sim 1000 \text{ km s}^{-1}$, during this time a galaxy travels $\sim 10 \text{ kpc}$, a length comparable to that of the tails observed in H I. This means that H I tails are short living structures, thus their relatively low number in blind surveys does not rule out RPS as a dominant mechanism

¹⁵ Note that the classical evaporation is assumed here. If instead saturated evaporation (Cowie & Songaila 1977) is assumed, the evaporation timescale typically increases by a factor of a few. On the other hand, galactic clouds are clumpy so the actual contact surface between the hot ICM and the cold clouds can be much larger than the surface of a single spherical cloud, which will reduce the evaporation timescale, along with the likely turbulence around the mixing layers.

affecting cluster galaxy evolution. It is worth remembering that this result is in agreement with what found from the analysis of H α narrow-band imaging data: indeed, the large amount of ionised gas measured within the tails of ram pressure stripped galaxies, which is fairly comparable to that of the H I removed from the galaxy disc, combined with its short recombination time ($\lesssim 5$ Myr), and the length of the tails (up to 100 kpc) suggests that the gas has been stripped as cold atomic hydrogen and later ionised and kept ionised in the tail once in contact with the hot ICM (see Sec. 3.2.4).

On the other hand, such a steady, non-radiative evaporation model is certainly too simplified. As stated in Sec. 3.2.5, heat conductivity is typically largely suppressed in the ICM and the interface between the ICM and the hot ISM, which is typically attributed to magnetic field. Even in the absence of magnetic field, hydrodynamical instabilities and turbulence enhance mixing of the stripped cold ISM and the hot ICM by drastically increasing the contact surface area between two phases. However, radiative cooling can be significant as the mixed gas (with a temperature of about the geometric mean of the cold and hot gas temperatures) can cool quickly. Clouds with sufficiently short cooling time in the mixed gas can even grow with time (e.g., Gronke et al. 2022). Such kind of turbulent radiative mixing layer has received a lot of attention recently (e.g., Gronke & Oh 2018; Fielding et al. 2020; Sparre et al. 2020; Tan et al. 2021; Gronke et al. 2022), with the focus on galactic winds and circumgalactic medium. As hydrodynamical instabilities, turbulence and magnetic field are inevitable in stripped tails, more works are required to better understand evaporation and mixing of the stripped ISM in the surrounding hot ICM.

5.1.2 Gas cooling into giant molecular clouds

The detection of large amounts of molecular gas at large distances from the galaxy opened the question whether this molecular gas has been stripped from the inner disc, or it has been formed in-situ after the cooling of the atomic phase. Indeed, as clearly explained in Vollmer et al. (2001b), two major physical processes are competing within the tail of stripped cold gas embedded in a hot diffuse ICM: cooling and heating. As explained in previous sections, once in contact with the hot ICM, the diffuse molecular gas component can be evaporated by the hot ICM. If the density of the stripped gas is sufficiently high, however, self shielding in the outer layers can protect the inner regions from heating and allow the cooling of the gas into giant molecular clouds, where star formation can take place. The presence of diffuse dust, now confirmed by recent far-infrared observations (Longobardi et al. 2020b), could contribute to the cooling of the gas within the tails (see Sec. 3.2.6). The formation of molecular gas generally occurs whenever the column density of H I exceeds 3×10^{20} - 10^{21} cm $^{-2}$ (Schaye 2004) and becomes more efficient in the presence of dust, which can act as a catalyst in the formation of molecular gas and can contribute to the cooling of the gas via absorption of the incoming radiation (Maloney et al. 1996; Krumholz et al. 2009). The typical timescale

for the formation of molecular hydrogen is $\tau_{\text{H}_2} \simeq 10^9/n_e$ yr (Hollenbach & Tielens 1997). Vollmer et al. (2001b) also noticed that, if stripped from the inner regions where star formation occurs, the molecular gas is not further heated by the UV radiation produced by the newly formed stars and thus can collapse if not supported by another source of energy. Furthermore, in the lack of magnetic fields molecular clouds can be destroyed by Kelvin-Helmholtz instabilities before they collapse to form new stars (Yamagami & Fujita 2011). Within a typical environment with characteristics similar to those encountered in the Virgo cluster ($n_e \simeq 10^{-3}$ cm $^{-3}$, $T \simeq 10^7$ K), most of the gas in the tail is expected to be either hot ($T \geq 10^6$ K), ionised, or low density ($n_e \geq n_{\text{ICM}}$), or molecular, cold ($T \sim 10$ -100 K), and high-density ($n_e \geq 100$ cm $^{-3}$) (Vollmer et al. 2001b). It is thus clear that under specific conditions, when the density of the gas is sufficiently high, new stars can be formed in the stripped gas. It is worth recalling that the coexistence of different gas phases, from the cold molecular gas, through the ionised phase, up to the hot plasma, has been also observed in other characteristic regions on the edges of galaxies and their surrounding ICM such as in cool cores in NGC 1275 in Perseus (Conselice et al. 2001; Salomé et al. 2006, 2011) and M87 in Virgo (e.g. Forman et al. 2007; Sparks et al. 2009; Boselli et al. 2019b). These observations confirm that different gas phases at different temperature and density can cohabit the hostile intracluster environment. It has also been stressed that, once star formation has occurred, the newly formed stars, which do not suffer the ram pressure exerted by the ICM because of their very low cross-section, get decoupled from the molecular gas cloud which is still decelerated by the external pressure during the travel of the galaxy within the high-density region, as indeed observed in ESO137-001 in the Norma cluster (Tonnesen & Bryan 2012; Jáchym et al. 2019) or in IC3418 in Virgo (Kenney et al. 2014).

5.1.3 Star formation within the tail

A key question in the study of the fate of the stripped gas is understanding whether it can contribute to the intracluster light by forming new stars outside the stellar discs of stripped galaxies, or whether it just pollutes the diffuse ICM. Indeed, blind surveys such as those carried out in H I or in narrow-band H α imaging clearly indicate that star formation in the tails of stripped galaxies is not ubiquitous (Boissier et al. 2012; Boselli et al. 2016a, 2018b; Fossati et al. 2016; Yagi et al. 2017; Gavazzi et al. 2018b; Laudari et al. 2022). There is also evidence that whenever star formation is present, this occurs with an efficiency reduced by a factor of $\gtrsim 5$ -10 with respect to that of star forming discs (Boissier et al. 2012; Jáchym et al. 2014, 2017; Moretti et al. 2018, 2020b; Gullieuszik et al. 2020).

IFU observations indicate that, within the compact regions in the tails, the velocity dispersion of the gas is lower than in the diffuse component ($\sigma \simeq 25$ -50 km s $^{-1}$; Fossati et al. 2016). The density of the gas here is sufficiently high, as the one encountered in typical GMC in the Milky Way (gas mass $5 \times 10^4 \leq M_{\text{GMC}} \leq 5 \times 10^6 M_{\odot}$, size $5 \leq r_{\text{GMC}} \leq 30$ pc, volume densities 50

$\lesssim n(\text{H}_2) \lesssim 500 \text{ cm}^{-3}$, Solomon et al. 1987; Engargiola et al. 2003). At these densities the typical collapse time (free fall time) for a cloud with a spherically symmetric distribution of mass is:

$$t_{\text{ff}} = \sqrt{\frac{3\pi}{32G\rho}} \simeq 5\text{Myr} \quad (49)$$

where ρ is the mean density of the gas. On relatively short timescales compared to the typical time necessary for a galaxy travelling at $\simeq 1000 \text{ km s}^{-1}$ to form 50 kpc tails ($\simeq 30 \text{ Myr}$) stars are formed within the tail. Thanks to the spectacular angular resolution in the multifrequency data available for perturbed galaxies in nearby clusters, and in particular in Virgo, the physical, kinematic, and spectro-photometric properties of the H II regions formed within the tails have been studied in detail. These compact H II regions are characterised by star clusters of mass $M_{\text{star}} \simeq 10^3\text{-}10^5 M_{\odot}$ and luminosities $L(\text{H}\alpha) \simeq 10^{36}\text{-}10^{38} \text{ erg s}^{-1}$, corresponding to star formation rates $SFR \simeq 10^{-3}\text{-}10^{-4} M_{\odot} \text{ yr}^{-1}$ (Sun et al. 2007a; Hester et al. 2010; Fumagalli et al. 2011; Boselli et al. 2021; Junais et al. 2021). Slightly larger values have been found for the star forming blobs detected in the tails of the jellyfish galaxies analysed during the GASP survey (Poggianti et al. 2019a) probably because these blobs are unresolved in these higher distance galaxies. The extraplanar H II regions have thus characteristics similar to those observed in galaxies suffering a combined effect of harassment and ram pressure (NGC 4254, Boselli et al. 2018b; VCC1249, Arigoni Battaia et al. 2012). The mean age of the stellar population of these regions is of $\lesssim 100 \text{ Myr}$, or even younger ($\lesssim 30 \text{ Myr}$) whenever selected in narrow-band H α imaging, consistent with a picture where they were formed only recently as expected in a short-lived interaction. The metallicity of the gas in these regions is generally similar to that of the parent galaxy in its outer disc (Sun et al. 2007a; Fossati et al. 2016). Similar values of stellar masses, H α luminosities, and SFR derived using HST data to resolve the individual star forming regions are observed in the tail of one ram pressure stripped galaxy in the Coma cluster (D100), where the mean age population is $\leq 50 \text{ Myr}$ (Cramer et al. 2019).

It is still unclear why H II regions are formed within the tail in some objects and why not in others. These condensed regions are formed within the turbulences and instabilities created in the friction layers between the cold ISM stripped during the interaction and the hot ICM (Roediger et al. 2014; Tonnesen & Bryan 2021, G. Henseler priv.comm.). The efficiency in producing high density regions might depend on the impact parameters and on the physical properties of the surrounding medium. The lack of star forming regions far from the galaxy in the tails of NGC 4569 (Boselli et al. 2016a), NGC 4330 (Fossati et al. 2018) and ESO 137-002 (Laudari et al. 2022), contrasts with the large number of young H II regions in the tails of ESO 137-001 (Fossati et al. 2016), UGC 6697 Consolandi et al. (2017), and IC 3476 (Boselli et al. 2021). Our samples are still too small to identify the main physical variable (if one exists) driving the presence of these features. Different scenarios should be further tested with tuned simulations, which explore differences in

the quantity of stripped gas according to realistic wind angles experienced on different possible orbits of the galaxy within the cluster, and on the galaxy structural parameters. Furthermore, simulations also suggest that the presence of magnetic fields does not strongly affect the quantity of stripped material, but rather indicate that the gas is better confined in filamentary structures or bifurcated tails such as those observed in ESO 137-001, and thus might favor the formation of giant molecular clouds (Roediger et al. 2006; Tonnesen & Stone 2014; Ruszkowski et al. 2014; Ramos-Martínez et al. 2018; Vijayaraghavan & Ricker 2017). Some of these simulations also predict the formation of new stars in the tails, but assuming quite uncertain (and different) recipes for the star formation efficiency within the stripped material.

Early GADGET simulations (e.g., Kronberger et al. 2008a; Kapferer et al. 2009) cannot model mixing sufficiently well (e.g., Sijacki et al. 2012), overpredicting the star formation activity in the stripped ISM. On the contrary, the simulations of Tonnesen & Bryan (2012) or Lee et al. (2020) rather suggest a weak star formation activity in the turbulent wakes formed during the interaction ($\sim 1\%$ with respect to that formed within the disc). This activity is mainly limited to clumps where the density of newly formed stars is $\sim 3 \times 10^4 M_{\odot} \text{ kpc}^{-2}$. The star formation in the tail can last ~ 1 Gyr and significantly drop on longer timescales (Calura et al. 2020). The star formation in the tail seems principally modulated by the external pressure of the ICM rather than by the strength of the ram pressure. Low rates of star formation in the tails of dwarf galaxies are also predicted by the simulations of Steyrleithner et al. (2020).

5.2 ICM clumping

Recent X-ray observations have suggested that the ICM distribution is not smooth but instead inhomogeneous (or clumpy), especially at the cluster outskirts (e.g., Walker et al. 2019). The ICM clumping factor, $C \equiv \langle n_e^2 \rangle / \langle n_e \rangle^2$ (Mathiesen et al. 1999), can be derived from the X-ray data and typically measures both the azimuthal variations and local clumping at scales of below 100 kpc. The clumping factor measured in clusters is small, from close to 1 within R_{500} to typically < 1.5 at $\sim r_{200}$ (e.g., Walker et al. 2019). Since the X-ray emissivity of the ICM is proportional to n_e^2 , the ICM clumping can bias the measured ICM density, which can further bias the measured ICM gas mass (e.g., Walker et al. 2019). The ICM clumping is typically induced by bulk motion and turbulence in the ICM. This deviation from the hydrostatic equilibrium suggests that the cluster mass from the X-ray data by assuming hydrostatic equilibrium is biased, which has become a key question in cluster cosmology (e.g., Kravtsov & Borgani 2012).

Many of the ICM clumps can originate from cluster galaxies, detached via RPS or tidal interaction/stripping (e.g., Dolag et al. 2009; Vazza et al. 2013) and now evaporating in or mixing with the ICM. The ISM-to-ICM mass ratio in local clusters is small. The ICM-to-stellar mass ratio in $M_{500} > 10^{14}$

M_{\odot} clusters is $\sim 3 - 12$ (e.g., [Leauthaud et al. 2012](#); [Gonzalez et al. 2013](#)). The average ISM-to-stellar mass ratio in cluster galaxies can be estimated by combining the cold gas scaling relation in galaxies (e.g. [Blanton & Moustakas 2009](#); [Boselli et al. 2014d](#)) and galaxy mass function in clusters (e.g., [Ahad et al. 2021](#)). Such an analysis gives an average ISM-to-stellar mass ratio of ~ 0.3 in clusters. Thus, the average ISM-to-ICM mass ratio is only $\sim 5\%$ in nearby clusters. Nevertheless, the evaporation time for the stripped ISM can be substantial so the induced ICM inhomogeneities can be long-lasting. The mixing between the stripped ISM and the ICM is poorly understood. The MHD simulations also suggest that the stripped ISM clouds can grow via mixing under certain conditions, e.g., when the cooling time of the mixed gas is shorter than the mixing time (e.g., [Gronke & Oh 2018](#); [Fielding et al. 2020](#); [Sparre et al. 2020](#)). Moreover, the motion of ISM-less galaxies (or of their dark matter halos only) in clusters can still induce ICM inhomogeneities and turbulence in the wakes behind the galaxy orbits (e.g., [Kim 2007](#); [Ruszkowski & Oh 2011](#)).

There are isolated HI clouds detected in the Virgo cluster (e.g., [Taylor et al. 2012](#)), although no X-ray enhancement was detected from any of the HI clouds from the existing data. Recently, the first example of an X-ray/H α isolated cloud in the intracluster space was discovered in A1367 ([Ge et al. 2021](#)) (the H α cloud was first discovered by [Yagi et al. 2017](#)), presenting a robust example connecting the ICM clumps and the stripped ISM clouds. Follow-up observations with the IRAM 30m telescope also revealed molecular gas in the cloud ([Jáchym et al. 2022](#)). This first example also suggests that at least some ICM clumps are multiphase in nature and implies that the ICM clumps can also be traced in H α from future deep and wide-field H α surveys.

5.3 ICM metal enrichment

The ICM is enriched with metals with an average abundance of ~ 0.3 solar (e.g., [Yates et al. 2017](#); [Mernier et al. 2018](#)). The ICM is composed of pristine gas and ejected ISM from cluster galaxies over the formation and evolution of clusters. The ICM metals should mainly come from stars in cluster galaxies, ejected through AGN feedback (quasar and radio modes), stellar feedback, RPS, galaxy mergers and tidal interactions. The properties of the ICM metals (abundance, distribution and evolution) present important constraints to reconstruct the SF history in cluster galaxies, the evolution of AGN and stellar feedback and other processes to transport metals from galaxies to the ICM. Recent X-ray constraints on the ICM metallicity evolution generally support the “early enrichment” model, giving the little evolution of the ICM metal content since $z \sim 1$ and the typically constant metallicity at the cluster outskirts (e.g., [Mantz et al. 2017](#); [Liu et al. 2020](#)). The strong mass dependency on the ratio between the ICM metallicity and the cluster stellar mass fraction from groups to clusters may also require early enrichment (e.g. [Bregman et al. 2010](#); [Renzini & Andreon 2014](#); [Biffi et al. 2018](#)). The “early enrichment” model

(typically related to strong winds during the formation and rapid growth of galaxies, and sometime their SMBHs) was also supported by the recent simulations (e.g., [Vogelsberger et al. 2018](#); [Pearce et al. 2021](#)), although the detail (e.g., IMF, SN type/rate/yields, transport efficiency) is not yet agreed. Thus, the ICM is mostly enriched beyond z of 1 and the effect of the late enrichment (including RPS) since $z \sim 1$ is minor and mainly shown in the inner regions of clusters.

How much can RPS contribute to the ICM enrichment? In section 5.2, we estimated the average ISM-to-stellar-mass ratio. We can also estimate the average metallicity of cluster galaxies, weighted by the galaxy mass function and the ISM mass fraction. We do that by assuming the mass-metallicity relationship from [Foster et al. \(2012\)](#). Integrating between M_{star} of $10^8 - 10^{11.5} M_{\odot}$, the average metallicity of cluster galaxies is 1.2 solar. Thus, for an ISM-to-ICM mass fraction of 0.05 and an ISM metallicity of 1.2 solar, if 50% of the ISM is stripped from galaxies, the expected ICM metallicity increase is only 10%, for the original ICM metallicity of 0.3 solar. This simple estimate is also consistent with the simulation results from [Domainko et al. \(2006\)](#), which suggests that RPS can only contribute to $\sim 10\% - 15\%$ of the ICM metal. Indeed, if RPS plays an important role on the ICM metal content, one may expect a strong correlation between the ICM metallicity and the cluster mass, as ram pressure increases with the cluster mass ($\propto M^{2/3}$ for the self-similarity). However, the observed correlation between the ICM metallicity and the cluster mass is very weak (e.g., [Truong et al. 2019](#)).

Nevertheless, RPS can still play a role to add on the ICM metal content and modify the ICM metal distribution. Simulations (e.g., [Schindler et al. 2005](#); [Domainko et al. 2006](#); [Kapferer et al. 2007](#)) suggest that RPS is more important around cluster centres where the ram pressure is high, while galactic winds are more important at the outskirts where winds are less confined by the surrounding ICM. RPS also leaves trails and plumes of high-metallicity gas behind galaxies undergoing stripping, which can be detected with the high-resolution ICM abundance maps. Cluster mergers can also enhance RPS and the subsequent metal enrichment ([Ebeling & Kalita 2019](#)).

5.4 Intracluster light and dust contribution

The presence of diffuse stellar light in the intracluster space, dynamically hot and bound to the cluster, has been known for many years (e.g., [Gonzalez et al. 2005](#); [Mihos et al. 2005](#); [Montes 2019](#); [Contini 2021](#)). The intracluster light (ICL) carries the imprint of the growth history of the cluster and contributes to a significant fraction of the stellar mass in clusters (e.g., [Pillepich et al. 2018](#); [Montes 2019](#); [Contini 2021](#)). While the bulk of the ICL is believed to be evolved stellar population removed from cluster galaxies by tidal interactions and mergers (e.g., [Contini 2021](#)), the discovery of star formation in stripped tails as discussed in Sec. 3.3 suggests an *in situ*, young component of the ICL. There have also been reports of blue intracluster light (e.g., [Starikova](#)

et al. 2020). The cosmological simulation by Puchwein et al. (2010) also attributes up to 30% of mass in intracluster stars to young stars formed in the intracluster space, inside cold ISM that was stripped from infalling galaxies by ram pressure, although one has to be aware of the uncertainties of transport processes, cooling and star formation processes in the simulation.

What is the fraction of the ICL that comes from this *in situ* channel? One can write its contribution as:

$$\frac{M_{\text{ICL,SF}}}{M_{\text{ICL}}} = \left(\frac{M_{\text{ICL,SF}}}{M_{\text{ISM,RPS}}}\right) \times \left(\frac{M_{\text{ISM,RPS}}}{M_{\text{ISM}}}\right) \times \left(\frac{M_{\text{ISM}}}{M_{\text{star}}}\right) / \left(\frac{M_{\text{ICL}}}{M_{\text{star}}}\right) \quad (50)$$

where $M_{\text{ICL,SF}}$ is the total mass of ICL formed via the *in situ* channel in the stripped ISM, M_{ICL} is the total mass of the ICL, $M_{\text{ISM,RPS}}$ is the total mass of the stripped ISM, M_{ISM} is the total mass of the ISM and M_{star} is the total stellar mass of the cluster. $M_{\text{ISM}}/M_{\text{star}} \sim 0.3$ as discussed in Sec. 5.2. $M_{\text{ICL}}/M_{\text{star}}$ is uncertain, 0.05 - 0.5 from Montes (2019) (also depending on the detailed definition of the ICL). We can assume an average $M_{\text{ISM,RPS}}/M_{\text{ISM}} \sim 0.5$, which is also consistent with the average estimates from Gullieuszik et al. (2020). Existing observations generally suggest that the star formation efficiency in the stripped tails is not as high as that in the galactic disc (e.g., Boissier et al. 2012; Kenney et al. 2014; Jáchym et al. 2014, 2017; Gullieuszik et al. 2020). Gullieuszik et al. (2020) concluded that the star formation efficiency in the tails of GASP galaxies is ~ 5 times lower than in the galactic disks. In the galactic disks, $\sim 6\%$ of gas is converted to stars in 100 Myr (e.g. Leroy et al. 2008). Thus, we can take $M_{\text{ICL,SF}}/M_{\text{ISM,RPS}} \sim 0.02$, which is also consistent with the typically long gas depletion timescales in stripped ISM ($\sim 10^{10.5}$ yrs from e.g., Cramer et al. 2019). With all these rough estimates, $M_{\text{ICL,SF}}/M_{\text{ICL}} = 0.006 - 0.06$. Here the star formation efficiency in the stripped tails is the biggest uncertainty, as already pointed out by Sun et al. (2010). Nevertheless, the current data do not suggest a significant contribution of the ICL from this *in situ* channel.

The contribution to the ICL by stars formed within the tails of perturbed galaxies has been studied recently using the data gathered during the GASP survey (Gullieuszik et al. 2020). An average SFR in the stripped tail is estimated to be $\sim 0.22 M_{\odot} \text{ yr}^{-1}$ per cluster, for typical GASP clusters with a velocity dispersion of 750 km s^{-1} at $z \sim 0$. Simply extrapolating this estimate to $z = 1$, they concluded that an integrated average value per cluster of $\sim 4 \times 10^9 M_{\odot}$ of stars formed in the tails of RPS galaxies since $z \sim 1$. For this typical GASP cluster, $M_{500} \sim 2 \times 10^{14} M_{\odot}$. With a stellar mass fraction of $\sim 3\%$, the GASP result essentially suggests $M_{\text{ICL,SF}}/M_{\text{ICL}} \sim 0.0007$. The GASP results should only be taken as a lower limit, giving the vast majority of the cluster volume not probed (only the small MUSE fields around each GASP galaxy studied) and the incomplete sample of the cluster galaxies.

Recent studies have also begun to reveal the presence of diffuse dust in the intracluster space (or intracluster dust) (e.g., Planck Collaboration et al. 2016; Gutiérrez & López-Corredoira 2017; Gjergo et al. 2020; Longobardi et al.

2020b, and references therein). Two methods have been applied, direct detection of the FIR emission from the dust and the reddening of background sources. Combining the Planck and the IRAS data, [Planck Collaboration et al. \(2016\)](#) constrained the average spectral properties of dust in clusters and derived an average dust-to-gas mass ratio (D/G) of $\sim 2 \times 10^{-4}$. However, most of the dust in clusters resides in galaxies so the contribution from the intracluster dust is small (e.g., [Gjergo et al. 2020](#)). [Gutiérrez & López-Corredoira \(2014, 2017\)](#) applied both methods and put an upper limit of D/G of $\sim 10^{-4}$ for the intracluster dust. [Gjergo et al. \(2020\)](#) attempted to model the dust content of cluster galaxies and suggested a rather small D/G of $\sim 10^{-6}$ for the intracluster dust. They also concluded that cluster spiral galaxies contribute to the bulk of the intracluster dust. [Longobardi et al. \(2020b\)](#) studied the reddening of background sources behind the Virgo cluster and derived a total dust mass of $\sim 2.5 \times 10^9 M_{\odot}$ within 430 kpc (or $\sim 0.43 \times r_{200}$), which suggests a rather high D/G of $\sim 3 \times 10^{-4}$. The dust sputtering time in the hot ICM is on the order of 10 Myr in the cluster core and 1000 Myr at 1 Mpc from the cluster centre ([Draine & Salpeter 1979](#); [Vogelsberger et al. 2019](#)) so the intracluster dust needs to be continuously replenished. We recall that the intracluster dust plays a major role in the energy balance of the ICM enhancing and can even dominating the cooling of the hot gas responsible for the X-ray emission (e.g., [Montier & Giard 2004](#)).

6 The importance of RPS at different epochs and in different environments

6.1 Clusters vs. groups and other environments

In the previous Sections we have described the role of several environmental processes and most notably RPS on the transformations occurring to satellite galaxies in massive haloes (mostly galaxy clusters in the local Universe). We now describe the statistical relevance of these processes on the overall galaxy population as a function of galaxy stellar mass and host halo mass. By using the semi-analytic model of [Henriques et al. \(2015\)](#) we estimate that the fraction of galaxies with $M_{\text{star}} > 10^9 M_{\odot}$ living in haloes more massive than $10^{14} M_{\odot}$ is 25% at $z = 0$. This substantial fraction means that environmental processes acting in clusters cannot be neglected when a complete population of relatively massive galaxies is studied in the local Universe. However, this fraction drops to 5% and 2% at $z = 1$ and $z = 1.5$, respectively. It therefore seems that the most favorable environment for RPS to occur becomes increasingly rare as redshift increases. Moreover, the most massive haloes at $z > 1.5$, the so-called protoclusters, are mostly unrelaxed structures which makes them difficult to identify in galaxy surveys ([Shattow et al. 2013](#)) and could imply that these forming structures do not have dense hot gas for RPS to be effective. A possible partial exception to this are the dense cores of high-redshift protoclusters (SPT-CLJ0459, [Strazzullo et al. 2019](#) and JKCS041, [Andreon et al. 2014](#))

where RPS could potentially be effective. The authors of these studies indeed find a high quiescent fraction ($> 80\%$) for galaxies spectroscopically confirmed in the clusters suggesting that environmental quenching was already active in these systems at these epochs. However, the high stellar mass limit of their observations coupled with the small statistics hampers a clear identification of the quenching mechanism. The simulations presented by [Quilis et al. \(2017\)](#) suggest that the overall effect of stripping is subdominant at $z = 2$ even in clusters with a hot ICM, because a large fraction of this gas is accreted and cools onto the galaxies. These authors also found different behaviours for galaxies with stellar masses below $10^{10}M_{\odot}$, which have eccentric orbits at the outskirts of the cluster and are thus only mildly perturbed, and the most massive ones which have more radial orbits and therefore can reach the dense cluster cores. Even for the latter population the effect of stripping is marginal in these simulations which points to other processes to explain the high passive fractions found in the aforementioned high- z clusters.

Another, less extreme, environment in which galaxies live are galaxy groups. Several definitions for what is a group exists, but in general those environments have a host halo mass in the range $10^{13} - 10^{14}M_{\odot}$. The fraction of galaxies with $M_{\text{star}} > 10^9M_{\odot}$ living in this halo mass range is 47% at $z = 0$ and stays constant (within 5%) up to $z = 1.5$. This intermediate mass range is very important because halos that assemble into massive clusters are often in the group range and are known to pre-process the galaxies ([Dressler et al. 1997](#)) before their final arrival into the clusters. [Oman et al. \(2021\)](#) studied the stripping and quenching times in a local sample of galaxies using models derived and calibrated on a cosmological simulation of massive clusters. These authors found that while in massive clusters the stripping of HI is almost complete before the first pericenter passage, in groups it takes a significantly longer time (~ 3 Gyr), likely due to the reduced ram pressure force exerted by the intragroup medium. In both cases a complete suppression of star formation occurs 2–3 Gyr later. This is not inconsistent with the short quenching times derived for some RPS galaxies in Virgo and Coma. Indeed, this analysis of the full galaxy population includes a significant fraction of objects whose molecular gas reservoir is not stripped and therefore the quenching follows the H_2 consumption timescale of a couple of Gyr. Lastly, these authors found that the lowest mass groups in their sample ($M_{\text{halo}} < 10^{13}M_{\odot}$) strip and quench their satellites extremely inefficiently with typical time-scales that approach the age of the Universe. These results agree with the observations of nearby groups: [Roberts et al. \(2021b\)](#) using a broad-band optical selection found that the frequency of RPS candidates in groups ($M_{\text{halo}} < 10^{14}M_{\odot}$) is lower than in clusters by a factor of ~ 2 . Consistent with this result is also the presence of HI-deficient galaxies ((e.g. [Fabello et al. 2012](#); [Brown et al. 2017](#))) and of radio continuum tails [Roberts et al. \(2021b\)](#) recently discovered in nearby groups.

A particularly favorable environment for RPS to be efficient might be merging clusters of galaxies (e.g. [Roediger et al. 2014](#); [Stroe et al. 2015, 2017](#); [Ebeling & Kalita 2019](#)). In these environments, galaxies belonging to a given structure might suffer an increased external pressure due to their non-isotropic

motion once entering into the other massive halo. The compression of their ISM can trigger star formation, as indeed observed in several merging structures at redshift $z \sim 0.15-0.3$ (e.g. [Stroe et al. 2015, 2017](#); [Ebeling & Kalita 2019](#)). Clear examples of triggered RPS in merging systems in the very local Universe are rare because of the limited sampled volume. There are, however, a few examples which might suggest an increased RPS efficiency in local merging structures. The first one is the observed concentration of young and blue low-mass poststarburst galaxies at the edges of the two infalling substructures within the Coma cluster observed by [Poggianti et al. \(2004\)](#). These objects might be the remnants of RPS galaxies where the external pressure exerted by the ICM of the main body of the cluster while crossing it as members of the infalling substructures enhanced their star formation activity and then totally stopped it on a short timescale. Another possible example is NGC 4522 in the Virgo cluster, a late-type galaxies with asymmetric atomic, molecular, and ionised gas distributions suggesting an ongoing RPS event ([Kenney & Koopmann 1999](#); [Vollmer et al. 2000, 2004b, 2008a](#); [Kenney et al. 2004](#); [Abramson & Kenney 2014](#); [Abramson et al. 2016](#); [Stein et al. 2017](#); [Minchin et al. 2019](#); [Longobardi et al. 2020b](#)). Tuned simulations indicate that the properties of this object can be hardly explained by the external pressure exerted by a smooth and static ICM, but would rather require large bulk motions and local density enhancements as those occurring in a shock-filled ICM experiencing subcluster merging ([Kenney et al. 2004](#)). Another intriguing local example is at the northwest of A1367 where a merger shock and a radio relic were detected ([Ge et al. 2019](#)), around at least five RPS galaxies in proximity (at least in projection) ([Yagi et al. 2017](#)).

[Roberts et al. \(2019\)](#) studied the role of the ICM density as a function of satellite galaxy stellar mass from a sample of local galaxy clusters with Chandra X-ray data. These authors found that for low-mass galaxies the quenched fraction mildly increases in the cluster outskirts at ICM densities below $\rho_{\text{ICM}} = 10^{-29} \text{ g cm}^{-3}$ before increasing sharply beyond this threshold. Their results are consistent with a picture where low-mass cluster galaxies experience an initial, slow-quenching mode driven by gas depletion via star formation in absence of accretion, followed by an accelerated quenching associated with RPS of the cold gas within a quarter of the virial radius. More massive galaxies, instead, might deplete their gas while still moving at larger clustercentric radii and their deeper gravitational potential wells makes them more resistant to RPS until they reach the most dense regions of the ICM. This study, while limited to clusters, might suggest that low-mass galaxies are stripped even in group-like environments while massive ones are more efficiently stripped in massive clusters. A complete consensus on the physical conditions leading to effective RPS is still missing, for instance [Mostoghiu et al. \(2021\)](#), using more than 300 simulated clusters, found that galaxies lose most of their gas when crossing the virial radius (in projected space), while [Oman & Hudson \(2016\)](#) suggest that the stripping occurs on average further-in, near pericenter.

We have seen that low mass galaxies are easily subject to stripping phenomena due to their shallow gravitational potential well. Indeed the stripping

of these objects does not always require a massive halo and can take place in other types of environment. Benítez-Llambay et al. (2013) proposed that dwarf galaxies can be stripped of their gas as they cross the network of filaments that builds the so-called cosmic web. The stripping has a rapid and dramatic influence on the star formation activity of these galaxies and could even explain the scarcity of dwarf galaxies compared with the numerous low-mass halos expected from the cosmological model in the Local Group. On larger scales Lee et al. (2021) studied nearly 70 galaxy filaments around the Virgo cluster finding that galaxies in the filaments have a normal H I content. This could imply that galaxies travelling along the filaments are experiencing a much milder RPS compared to those travelling across the filaments. This result, however, contrasts with the work of Castignani et al. (2022) who found that the star formation, gas content and morphological properties of galaxies in cosmic filaments are at intermediate levels between galaxies in isolation and in clusters suggesting that filaments are dense enough to produce measurable environmental effects (see also Winkel et al. 2021)). In a study of 24 jellyfish galaxies extracted from the GASP survey that do not reside in galaxy clusters, Vulcani et al. (2021) found two star forming objects ($M_{\text{star}} < 10^{9.1} M_{\odot}$) with ionised gas tails that could be associated to cosmic web stripping. The fact that these objects are actively forming stars, as opposed to the passive systems analysed by Benítez-Llambay et al. (2013), suggests that they are experiencing the early phases of the stripping or that the stripping is not rapid and efficient.

RPS can also occur in the gaseous halo of individual galaxies, as shown by Mayer et al. (2006) and Gatto et al. (2013). These authors coupled observations of dwarf quenched galaxies orbiting near the Milky Way (MW) with a stripping model to constrain the properties of the hot corona around the MW. A similar stripping event of a dwarf galaxy in the hot halo of a massive elliptical is reported by Arrigoni Battaia et al. (2012) that studied the interaction of VCC 1249 with M 49 in the Virgo cluster, concluding that both ram-pressure stripping and tidal interaction occurred. The joint action of the two mechanisms led to the removal of the H I gas from the ISM of VCC 1249, while the gravitational tides perturbed the disc generating stellar tails.

In conclusion, RPS can occur in a variety of environments provided that a galaxy travels with sufficiently high velocity through a medium that is dense enough (irrespective of its temperature) to overcome the gravitational potential well that keeps its ISM bound. The lower the mass of the target galaxy, the lower the RPS force needs to be to efficiently strip the gas and quench the star formation activity.

6.2 Evolution with cosmic time

We can also examine the evolution of the average ram pressure in clusters with redshift. As discussed in Sec. 2.1, for fixed cluster mass, one expects the ram pressure to increase with redshift, as $E(z)^{8/3}$, up to the time of cluster virialization and formation at $z \sim 3$. We can also follow the cluster growth

track. The self-similar relation, as shown in the Eq. 13 is clearly incorrect as it does not account for the hierarchical mergers and growth. The cluster growth history presented by McBride et al. (2009) can be roughly approximated by $M(z) \sim E(z)^{-3}$ at $z < 3$, which would suggest the ram pressure to evolve as $\sim E(z)^{2/3}$ (here we assume that RP scales as Eq. 17 that should apply for clusters). Therefore the ram pressure decreases with decreasing z as the cluster assembles its mass. The above simple estimates are consistent with the results from the analytic work by Fujita (2001), which shows that for a given cluster mass, RPS has more influence in high- z clusters to the extent that most of galaxies in rich clusters at $z > 1$ are affected by RPS. As non-gravitational processes reduce the ICM content within R_{500} , the strength of RPS is also tied to the actual contribution of non-gravitational heating with redshift (Fujita 2001), which is however poorly constrained from the current X-ray data at $z > 1$. Nevertheless, RPS is expected to be substantial in high- z clusters to at least $z \leq 2$ (also see Singh et al. 2019).

The detection of direct evidences of RPS beyond the local Universe are made difficult by the surface brightness dimming of the cometary tails. Due to this observational limitation, direct evidence for ongoing RPS at higher redshift is still relatively poor. Cortese et al. (2007) reported the detection of two cluster galaxies at $z \approx 0.2$ with asymmetric and extended features in B band images obtained with HST. Their modelling suggests that the morphologies of these galaxies have been influenced by the combined action of tidal interaction and RPS (see Sec. 3.1). Since then, a few other tens of similar objects have been found in deep HST images of clusters at $0.3 < z < 0.7$ (Owers et al. 2012; Ebeling et al. 2014; McPartland et al. 2016). However, as discussed in Sec. 3.3, the optical band selection is sensitive to intermediate age stars and cannot be taken as a direct proof of an ongoing or recent RPS event. While H I and X-Ray tails are undetectable at high-redshift with current facilities, significant advancements on the optical spectroscopic instrumentation has made the detection of H α tails possible up to $z \sim 0.7$. Vulcani et al. (2016) using HST slit-less spectroscopy analysed the H α morphology of galaxies in 10 clusters at $0.3 < z < 0.7$. Based on visual classification, these authors found that roughly 30% of the galaxies have a regular H α morphology, a 20% show sign of RPS and a 40% show signatures of a recent merger or tidal interaction. By comparing to a field sample, this work demonstrates that the cluster environment shapes galaxy evolution at these redshifts, however the morphological transformations detected can be caused by a variety of mechanisms. Another indirect evidence of RPS is reported by Vaughan et al. (2020) who found more compact H α radii compared to the stellar continuum in cluster galaxies at $0.3 < z < 0.6$ when contrasted to a field sample.

Boselli et al. (2019a) exploited the unique capabilities of MUSE at the Very Large Telescope to obtain deep IFU spectroscopy of the core of a $z = 0.73$ cluster. These observations revealed the first direct evidence of ongoing RPS in intermediate redshift galaxies. These authors reported the presence of two galaxies with extended tails of diffuse gas detected in the [OII] line doublet. The tails extend up to 100 kpc from the galaxy discs, and are not

associated with any stellar component, a typical signature of an RPS event. The surface brightness of these tails, once accounting for the cosmological dimming and the [OII] to H α ratio, is ~ 10 times higher than those measured in the local Universe (see also [Moretti et al. 2022](#)). A possible explanation for this evidence can be found in the (molecular) gas fractions of main-sequence star forming galaxies at $z \sim 0.7$ which are ~ 10 times higher than their local counterparts ([Tacconi et al. 2018](#)). A larger sample is however required to confirm whether the increased surface brightness is a common feature of intermediate- z RPS tails or if it is limited to these objects. [Boselli et al. \(2019a\)](#) also found that these RPS galaxies exhibit a significant star formation activity, consistent with normal galaxies of the same mass and redshift. This could be explained by a recent onset of the ram-pressure that could have produced the tails without significantly reducing the gas content in the star forming disc or by the initial higher gas fraction in these objects which makes the quenching of star formation more difficult.

At even higher redshift, direct evidence of RPS become even more challenging to be seen. As the H α line is redshifted in the near-IR, deep observations from the ground have to overcome the increasing brightness of the night sky, requiring extremely long integrations. Upcoming NIR space telescopes (e.g. the James Webb Space Telescope) will provide the IFU capabilities required for this task. At present, however, we can only rely on indirect evidences of the role of RPS at $z > 1$. Many studies have exploited the exquisite quality of multiwavelength surveys in the deep fields to identify satellite galaxies and to derive the average time it takes for these galaxies to be quenched by environmental processes. [Nantais et al. \(2017\)](#) reported that the quenching efficiency (i.e. the fraction of galaxies quenched by the environment) sharply decreases from $z \sim 0$ to $z \sim 1.5$, as first proposed by [McGee et al. \(2009\)](#). This result implies that at $z \sim 1.5$ the satellite galaxies population is indistinguishable from isolated galaxies in terms of their star formation activity, implying that any environmental process operates on scales comparable to the Hubble time at that epoch. At lower redshift, however, a passive population of galaxies made passive by the environment builds up. [Balogh et al. \(2016\)](#), [Fossati et al. \(2017\)](#), and [Foltz et al. \(2018\)](#) found that the quenching times are long ($\sim 2 - 5$ Gyr in the stellar mass range $M_{\text{star}} = 10^9 - 10^{11} M_{\odot}$ and shorter for more massive objects) which points at the lack of infall of fresh gas from the cosmic web as the dominant environmental quenching mechanisms in galaxy groups. However, when those results are compared to cluster samples at the same redshift, [Balogh et al. \(2016\)](#) and [Foltz et al. \(2018\)](#) found that the average quenching times are shorter in clusters ($M_{\text{halo}} > 10^{14} M_{\odot}$) suggesting that in these massive haloes the dynamical removal of gas, possibly associated to RPS, is occurring. Since the results are obtained by studying the galaxy population as a whole it remains unclear if RPS is occurring only on some galaxies with high relative velocities with respect to the cluster or if it happens on a large fraction of galaxies although with a smaller efficiency than in the local Universe. Lastly, despite having shown analytically that the ram pressure should increase with redshift, we need to consider that high- z

galaxies are usually more compact (van der Wel et al. 2014) and therefore have a higher density of stars and gas, making the effects of a stronger ram pressure less appreciable. Another consequence of the galaxy properties at high- z is that their larger initial gas reservoir requires a significant depletion of the gaseous disc before an effect on the star formation activity can be observed.

7 Comparison with other mechanisms

The large set of results reviewed in the previous Sections can be used to derive some general considerations on the importance of RPS in shaping galaxy evolution in high density regions also in comparison with other perturbing mechanisms such as gravitational interactions (galaxy harassment, e.g. Moore et al. 1996, 1998) or the suppression of gas supply on the disc from the cosmic web once a galaxy becomes satellite of a larger halo (starvation, e.g. Larson et al. 1980; Bekki et al. 2002; Kawata & Mulchaey 2008). In the following Sections we will show that the effects of RPS on galaxy evolution are significantly different than those due to starvation and harassment. We have, however, to caution that these processes are often acting together on individual galaxies and therefore it is not always possible to identify a single dominant mechanism responsible for specific observations.

7.1 Effects on galaxies and timescales

In an RPS event gas removal occurs outside in, suppressing the star formation activity of the perturbed galaxies starting from the outer discs and moving to the inner regions until the ram pressure force cannot overcome the gravitational restoring force (see Sec. 2). In dwarf systems, where the gravitational potential well is shallower, the stripping process can quench the star formation activity over the entire galaxy. As detailed in Sec. 4.2, the RPS episode and the star formation quenching are relatively rapid ($\lesssim 0.5\text{-}1.0$ Gyr) and typically shorter than the crossing time of the cluster ($\tau_{\text{crossing}} \simeq 2$ Gyr, (Boselli & Gavazzi 2006)), with only a small fraction of the most bound gas being stripped on longer timescales. These timescales are valid for intermediate mass galaxies and can be even shorter for dwarf systems ($M_{\text{star}} \lesssim 10^9 M_{\odot}$). In lower density regions the local conditions might not efficiently remove a significant fraction of the gas content of the perturbed galaxies, thus only partially reducing their star formation activity. As described in Sec. 6.2, RPS is expected to be more efficient at higher z due to the evolution of the ICM parameters. However, at early epochs, the galaxies were more compact and gas-rich than their local analogues, making their gas more gravitationally bound. The gas removal due to ram pressure might thus have less critical effects on the star formation activity, possibly leading to longer RPS timescales compared to the local Universe.

These RPS timescales are shorter than those expected for other processes like starvation and harassment. Starvation or strangulation, i.e. the stop of

gas infall on the stellar disc, quenches the activity of star formation on very long timescales. Although the molecular gas depletion timescale is $\tau_{\text{H}_2} \simeq 0.6\text{--}2.3$ Gyr (Leroy et al. 2008, 2013; Bigiel et al. 2011; Boselli et al. 2014c), the total amount of cold gas (HI+H₂) available on the disc of unperturbed spiral galaxies can sustain star formation at a constant rate for $\simeq 4$ Gyrs (Boselli et al. 2014c), or even longer considering that $\sim 30\%$ of the stellar mass is re-injected into the ISM through stellar winds as recycled gas (Kennicutt et al. 1994). Indeed, tuned models of galaxies suffering a starvation scenario, where the infall of fresh gas has been stopped, show that a significant quenching of the star formation activity occurs only after $\gtrsim 7$ Gyr (Boselli et al. 2006, 2014d). These long timescales can be slightly reduced if associated to efficient outflows (McGee et al. 2014; Balogh et al. 2016; Trussler et al. 2020). The same models also indicate that the decrease of the star formation activity is uniform at all galactocentric distances, producing shallow but extended stellar discs (Boselli et al. 2006, 2014d). Starvation cannot produce truncated discs on short timescales as those observed in HI-deficient galaxies, nor thick stellar discs as those of typical bright lenticular galaxies in nearby clusters (e.g. Dressler 2004; Boselli & Gavazzi 2006). Some works based on complete samples of galaxies from large surveys (e.g. SDSS, GAMA, GALEX) suggest long quenching timescales typical of starvation (McGee et al. 2009; Wolf et al. 2009; von der Linden et al. 2010; De Lucia et al. 2012; Wheeler et al. 2014; Taranu et al. 2014; Haines et al. 2015; Paccagnella et al. 2016). Indeed, Wetzel et al. (2013), deriving the quenching timescales of satellite galaxies in SDSS, found that for the complete satellite population the total quenching times are relatively long $\sim 4 - 6$ Gyr. Moreover these authors found that the most likely quenching path for satellite galaxies is the so-called “delayed+rapid” quenching where the SFR of galaxies remain largely unaffected during the delay time (at the expenses of HI being converted into molecular gas) and then the SF activity fades rapidly when the molecular gas reservoir runs out. Long quenching timescales appear to be common at $z \gtrsim 0.5$ indicating a larger and larger dominance of starvation (or lack of gas accretion onto satellite galaxies) compared to RPS as redshift increases (Balogh et al. 2016; Fossati et al. 2017; Foltz et al. 2018).

Harassment also requires relatively long timescales ($\simeq 3$ Gyr) to have significant effects on the perturbed galaxies (e.g. Moore et al. 1996, 1998; Gnedin 2003a; Mastropietro et al. 2005; Bialas et al. 2015). This is due to the fact that the relaxation time, i.e. the time necessary for a galaxy to have its orbit perturbed by a tidal interaction, is very long ($\tau_{\text{relax}} \geq 10^{10}$ yrs, (Byrd & Valtonen 1990; Binney & Tremaine 2008)) in rich clusters such as Coma (Boselli & Gavazzi 2006). Indeed, the probability that an object has to undertake multiple encounters, or a close interaction with another cluster member, is relatively low and might require several crossing of the cluster (Moore et al. 1998; Mastropietro et al. 2005). Harassment is able to truncate the gaseous (and stellar) disc, but also favors dynamical instabilities able to form bars and eventually induce gas infall in the inner regions, thus triggering the nuclear star formation or AGN activity of the perturbed systems (Henriksen & Byrd 1996;

Moore et al. 1996, 1998; Lake et al. 1998; Mastropietro et al. 2005; Ellison et al. 2011). Gravitational interactions can easily increase the overall activity of star formation of the perturbed systems and move them over the main sequence (e.g. Ellison et al. 2008; Scudder et al. 2012). Evidence for an increased nuclear activity of cluster galaxies has been searched for in nearby clusters, but never found with statistically convincing results (e.g. Moss & Whittle 1993, 2000; Moss 2006). An increased activity has been found in the infalling filaments, but far from the cluster, probably induced by tidal interactions (e.g. Porter et al. 2008).

7.2 Region of influence

As presented in Sec. 3, there is a large amount of observational evidence corroborated by models and numerical simulations, indicating that RPS is the dominant perturbing mechanism in local clusters. In the Coma and A1367 clusters tails of ionised gas are observed in $\sim 50\%$ of the late-type galaxies (Yagi et al. 2010, 2017; Gavazzi et al. 2018b) making this systems ideal targets for RPS studies. (see Sec. 3.2.4). This fraction can be even higher if we include tails recently detected in radio continuum (Chen et al. 2020; Roberts & Parker 2020) (see Sec. 3.2.1). If we consider that some tails might be missed for projection effects or for sensitivity, and that the tails observed in H α and radio continuum have a limited life time (10-40 Myr, see Sec. 3.2.4 and 3.2.1), we can justify that ram pressure is active and probably dominant in local clusters of mass $M_{cluster} \simeq 10^{15} M_{\odot}$. This result can also be extended to Virgo ($M_{Virgo} \simeq 10^{14} M_{\odot}$, see Sec. 3.2.4), where there is clear evidence that ram pressure is at place on some of the most massive spirals of the cluster (e.g. NGC 4501, NGC 4569, Vollmer et al. 2004a; Boselli et al. 2006, 2016a), and should be even more efficient on lower mass galaxies (see Sec. 2.2). The recent extremely deep radio observations of the Fornax cluster with MeerKAT (see Sec. 3.2.2) identified a large number of late-type systems with extended tails of HI gas proving that ram pressure can be efficient also in clusters/groups of mass $M_{cluster} \simeq 5 \times 10^{13} M_{\odot}$. At the lowest range of group haloes, galaxies with extended radio continuum tails have been observed by the LoTSS survey in groups of mass $M_{group} \simeq 3 \times 10^{12} M_{\odot}$, showing that RPS can occur also in these haloes. However, in these environments RPS galaxies are rarer than in more massive clusters making the process subdominant and possibly less efficient (Roberts et al. 2021b).

Having established that RPS is a very relevant (sometimes dominant) process in massive haloes, another question that arises is how its efficiency varies with the distance from the central galaxy. Tails of stripped gas have been observed mainly within the virial radius of local clusters. The most extreme known case being the galaxy CGCG097-026 in A1367, where an HI tail has been detected at a projected $R/r_{200} \simeq 2$ (Scott et al. (2012, 2022), see Sec. 3.2.2). A similar evidence comes from galaxies with truncated gaseous or star forming discs which mostly live within the virial radius of nearby clusters and

groups (see Sec. 3.4). Furthermore, the distribution of HI-deficient galaxies (see Sec. 3.6) peaks in the core of the cluster becoming similar to that of isolated objects at $\simeq 1-2 \times r_{200}$. We can thus conclude that RPS shows its effects mainly within the halo virial radius as also shown in the phase-space diagram in Figure 11.

These radial scales can be compared to those predicted by simulations for the other main perturbing mechanisms. Byrd & Valtonen (1990) and Moore et al. (1998) consistently underline that gravitational perturbations due to the potential well of the whole cluster and to flyby encounters with other members, whose density rapidly decreases with the clustercentric distance, make harassment particularly efficient in the innermost regions, at $\lesssim 0.5 \times r_{200}$ (e.g. Moore et al. 1998; Smith et al. 2010; Bialas et al. 2015). Conversely, starvation occurs once a galaxy enters the hot halo surrounding a massive cluster which could be outside the virial radius (up to $R \simeq 3-5 \times r_{200}$ (Bahé et al. 2013; Ayromlou et al. 2021)). However the effects of starvation on the star formation activity of galaxies can be delayed compared to the time of virial radius crossing. This could lead to an observed radial distribution of passive objects more similar to that expected for RPS. Moreover stripped or harassed galaxies can “backsplash” the halo after the first crossing and possibly after having lost gas and star formation activity. They can account for up to 40% of the galaxies observed between 1 and 2.5 virial radii (Wetzel et al. 2013) further complicating an accurate determination of the radius of influence of the aforementioned processes. We therefore warn that the sole position of a perturbed galaxy is not a unique indicator of the perturbing process, however the position in phase-space combined with accurate star formation indicators and ideally with the reconstruction of the star formation history of the galaxy can help in identifying the processes it underwent.

7.3 Dependence on structure formation

Despite the general picture of structure formation and galaxy evolution is becoming increasingly clear, it is still hard to quantify the relative importance of RPS with respect to that of other perturbing mechanisms at different epochs and in different environments. As mentioned in Sec. 6.2, we are still not able to trace with no ambiguity how the efficiency of RPS varied with time because of the complex and competitive evolution of the density of the ICM and of the gravitational bounding forces keeping the gas anchored to the stellar disc of galaxies with increasing z . However, we can intuitively argue that gravitational perturbations were more important than RPS at early epochs. Indeed, there are several indications that the infall of galaxies occurred via smaller groups, characterised by a relatively low velocity dispersion and a high density of objects, where gravitational interactions are more and more efficient in detriment of RPS (pre-processing, (Dressler 2004; Fujita 2004)). Still controversial, however, is the fraction of galaxies accreted as isolated vs. group members. While the merger-tree used in the semi-analytic models of McGee et al. (2009) and

De Lucia et al. (2012) and the hydrodynamic simulations of Han et al. (2018) consistently indicate that a $10^{14.5} M_{\odot}$ mass cluster at $z=0$ has accreted, on average, $\sim 40\text{-}50\%$ of galaxies of stellar mass $M_{\text{star}} \gtrsim 10^8\text{-}10^9 h^{-1} M_{\odot}$ via groups with halo masses $M_{\text{group}} > 10^{13} M_{\odot}$, the N-body simulations of Berrier et al. (2009) rather indicate that 70% of the galaxies are accreted as isolated objects in clusters of similar mass. The same simulations also suggest that less than 12% of the galaxies are accreted within groups with five or more systems, where pre-processing can efficiently perturb their evolution. The merger-tree used by McGee et al. (2009) also suggests that galaxies accreted through groups are, on average, more massive than those accreted as isolated systems. The same models also indicate that the fraction of galaxies falling in as isolated objects was higher in the past than at the present epoch. For reference, we recall that the typical infall rate of galaxies of mass $M_{\text{star}} \geq 10^8 M_{\odot}$ in a cluster like Virgo ($M_{\text{Virgo}} \simeq 10^{14} M_{\odot}$) is ~ 200 gal/Gyr (Boselli et al. 2008a; Sorce et al. 2021). Nonetheless we have observational evidence of two RPS galaxies in a cluster of mass $M_{\text{cluster}} = 2 \times 10^{14} M_{\odot}$ at $z \sim 0.7$ suggesting that, although rare, this process was already at place in these structures. We still do not have sufficient observational data to see whether this process was dominant at these epochs. Given the self-similar evolution of the ICM density suggested by the existing data to $z \simeq 1.8$ as discussed in Sec. 2.1, we can conclude that ram pressure was probably at place in all this redshift range.

It is interesting to underline that, through its first infall into a cluster, which generally occurs on radial orbits, a gas-rich galaxy suffers first a suppression of gas infall on the disc (starvation), with the later addition of an active removal of the cold ISM via RPS. At its passage close to the cluster core, the galaxy might also suffer a violent gravitational perturbation. This evolutionary scenario is only slightly changed if a galaxy is accreted from within a group, in which case the infalling system is expected to suffer starvation already in the group environment (e.g. Kawata & Mulchaey 2008), possibly combined with gravitational perturbations. A typical example is the Fornax cluster, where galaxies with tails have often perturbed morphologies, suggesting that RPS and gravitational perturbations are both active, as predicted by cosmological hydrodynamic simulations in this halo mass regime (e.g. Marasco et al. 2016). As mentioned in Sec. 3.1, the two families of mechanisms have additive and intertwined effects, thus contributing both directly and indirectly to the stripping of the gas (e.g. Weinmann et al. 2010; Bahé & McCarthy 2015; Henriques et al. 2015; Trayford et al. 2016; Cortese et al. 2021, and references in Sec. 3.1). Gravitational perturbations, indeed, flatten the gravitational potential well of galaxies, thus favoring the RPS process.

Other interesting objects are the lenticular galaxies inhabiting nearby clusters. While the physical, structural, and kinematical properties of the dwarf spheroidal galaxies can be easily reproduced by an RPS scenario (e.g. Boselli et al. 2008a; Boselli & Gavazzi 2014), the origin of massive lenticulars is probably dominated by gravitational interactions. Indeed, the structural properties of massive S0 galaxies and the weak dependence of the morphology segregation effect on galaxy density (e.g. Dressler 2004) are hardly explained by an RPS

transformation of spirals into lenticulars, but rather suggest an active role of gravitational perturbations occurring at early epochs when these objects were still members of smaller groups (pre-processing, (e.g. Byrd & Valtonen 1990; Gnedin 2003a; Dressler 2004; Fujita 2004)). This suggests that RPS, if present, was not dominant in the early Universe on the most massive galaxies entering the most massive haloes at that epochs. The same considerations also rule out starvation which is a milder process than RPS: in particular, the lack of fresh gas supply on long timescales after the perturbed galaxy becomes satellites of a larger halo, would lead to a decrease of the surface brightness of the inner disc, opposite to what observed in nearby massive lenticulars (e.g. Boselli et al. 2006, 2022). Starvation in the main cluster halo, which would require long timescales to be efficient, is also in odd with the observed recent formation of lenticulars, relatively rare at redshift $z \sim 0.5$ but dominant in local clusters (Dressler et al. 1997). To conclude, these scenarios clearly indicate that the average galaxy population in rich environments is affected by multiple effects and the objects where a single process dominates are generally rare.

7.4 Effects on the surrounding environment

In the RPS scenario all the components of the ISM (atomic, molecular, ionised, hot gas, and dust) can be stripped from the disc (see Sec. 3.2). The stripped ISM remains multi-phase, as some stripped ISM can cool to form stars and the mixing between the stripped ISM and the hot ICM proceeds. As discussed in Sec. 5.2, 5.3 and 5.4, RPS pollutes the ICM with the stripped ISM, effectively enriching the ICM with time, adding turbulence in the ICM, inducing density inhomogeneity or clumping in the ICM and increasing the ICL content with star formation in the stripped ISM. Nevertheless, the late enrichment with RPS can only contribute to a small fraction of the ICM metals ($\sim 10\%$ - 15%), although the roles of RPS in early enrichment are still unclear, mostly because of the uncertainty in the early enrichment models. The contribution to the ICL by the stars formed within the tails of stripped material of RPS galaxies is also small as discussed in Sec. 5.4.

Starvation, on the other hand, starts to take effect from relatively low-density regions so the galactic halo gas is mixed with the ICM at the outskirts where clumping is stronger than the cluster centre. The halo gas, with low density and the virial temperature of the galaxy, can hardly cool to form stars and may only be quickly heated to replenish the ICM, without leaving long-lasting ICM clumps or adding the ICL content. The halo gas generally has lower metallicity than the disc ISM so its role on the ICM enrichment is small.

Gravitational perturbations like mergers, tidal interaction and harassment act indifferently on all the different components of the perturbed galaxies (all forms of baryonic and dark matter). For cluster galaxies, the galactic dark matter halo is tidally truncated. Both stars and ISM can be dynamically heated to become unbound in the intracluster space, increasing the ICL and ICM content. It is believed that tidal interactions and mergers contribute

to the ICL the most over the hierarchical growth of clusters as discussed in Sec 5.4.

8 Conclusions

The works presented in this review have clearly shown how galaxies suffering an RPS event can be identified with no ambiguity by the presence of extended tails of gas at different phases without a diffuse and evolved stellar counterpart. Galaxies which have been perturbed in the past are generally characterised by radially truncated ISM discs, combined with a normal and extended stellar distribution. Other selection criteria, such as those based on the identification of strong asymmetries in broad-band optical images (jellyfish galaxies), require further multi-wavelength data to ensure they are RPS objects. RPS galaxies where star formation is occurring within the tail would satisfy the jellyfish selection but they are a sub-sample of the full RPS galaxy population.

The results we have collected and presented in this review consistently indicate that RPS is a major mechanism affecting galaxy evolution and it should be always taken into account when the galaxy environment is studied. Systems undergoing or recently perturbed by an RPS event are the dominant galaxy population in nearby massive clusters ($M_{\text{halo}} \gtrsim 10^{14} M_{\odot}$), where radio continuum, HI, H α tails or truncated discs are ubiquitous provided that wide field observations are gathered with a sufficient sensitivity. Galaxies with extended tails have been identified down to halo masses of the order of a few $10^{12} M_{\odot}$, but are generally rare and sometime associated to perturbed stellar morphologies witnessing at the same time an ongoing gravitational perturbations. Galaxies suffering an RPS event have been also identified in clusters up to $z \sim 0.7$, but the lack of complete and wide field spectroscopic surveys still prevent a firm understanding of how frequent these objects are. The physical properties of galaxies and of the high-density regions, and their expected evolution as predicted by hydrodynamic cosmological simulations, combined with statistical galaxy samples let us think that RPS has a milder impact than other mechanisms (starvation, harassment) on galaxy evolution at higher redshift.

Tuned models and hydrodynamic simulations indicate that the RPS event removes the different component of the ISM outside-in. Whereas in dwarf systems the stripping is generally complete, in massive systems some gas can be retained in the inner region, where the gravitational potential well of the galaxy is the deepest. The activity of star formation is reduced by the lack of gas. The perturbed galaxies thus migrate below the main sequence becoming quiescent, red objects without affecting their kinematic properties and the structure of old stellar populations. This quenching process is rapid ($\lesssim 1$ Gyr), in particular in dwarfs systems where most of the gas is removed at the first infall of the galaxy within the ICM before the pericenter of their orbit. Only under particular configurations such as edge-on stripping, when the perturbed gas is pushed along the disc, there might be a short lived burst of the star formation activity of the perturbed galaxies.

Star formation can be present in the tail of stripped material, but this does not occur in all RPS systems. There are, indeed, several objects with spectacular tails without any associated star forming region. The way the stripped gas can or cannot collapse to form stars is still poorly understood, and probably depends both on large (impact parameters between the galaxy and the surrounding ICM along the orbit) and small (turbulence, magnetic fields, self shielding of the gas within the tail) scale factors. A similar uncertainty (also related to this problem) remains in the way the cold gas stripped from the galaxy disc changes phase once mixed with the surrounding hot ICM. This gas contributes to the pollution of the ICM, but its effect remains marginal compared to the one from supernovae feedback in ellipticals.

Recent observations are clearly indicating $H\alpha$ narrow-band, HI, and radio continuum imaging surveys as the best way to identify galaxies undergoing an RPS event, provided that deep observations with wide field cameras coupled with sensitive instruments are used. To this regard, a large progress in this field will be made by the new generation radio facilities ASKAP, MeerKAT, and especially SKA, which will provide radio continuum and line observations at unprecedented sensitivity and angular resolutions for hundreds of thousands of galaxies in nearby and high redshift clusters. Significant progress in the characterisation of the properties of the hot ICM and in the study of the gas phase transformation within the tail of stripped material will be gathered by several X-rays space missions such as eRosita and ATHENA, which will also lead to the discovery of thousands new clusters at intermediate redshift.

Despite the fact that our view on the importance of the RPS process in galaxy evolution has significantly improved since this mechanism has been first proposed in the seventies of last century to explain the nature of head-tail radio galaxies, main questions remains unanswered. Some of them are related to the physics which governs the phase transition of the cold gas stripped from the disc. Indeed new observations and models are required to explain why the tails are not always observed simultaneously in the different cold atomic, molecular, ionised, and hot gas components and understand whether this evidence is physical or just resulting from an observational bias. The same improvements in our understanding of the physics of the RPS process might also be necessary to understand under which conditions the stripped gas collapses or not to form stars. The two physical processes of gas phase transformation and star formation, might be intimately related to the presence, strength and orientation of magnetic fields. Finally, it is still not totally clear which is the role of RPS in galaxy evolution at high redshift, where deep multifrequency data at high angular and spectral resolution are still lacking for significant samples of galaxies. Upcoming multiplexed spectroscopic facilities (e.g. MOONS or ERIS at VLT, PFS at Subaru, JWST) will dramatically increase the size and quality of the observational samples at intermediate to high- z , helping us to solve the remaining pieces of the RPS puzzle.

A Table of galaxies suffering RPS in nearby clusters

Table 2 shows the properties of galaxies suffering RPS in the nearby clusters Virgo, Coma, Norma and A1367. The description of the columns is as follows:

Column 1: galaxy name.

Column 2: morphological type: in order of priority: NED, GoldMine (Gavazzi et al. 2003a).

Column 3: nuclear classification, in order of priority from MUSE IFS or SDSS fiber spectra and published in Gavazzi et al. (2011, 2013a, 2018a).

Column 4: stellar masses are derived using the calibration of Zibetti et al. (2009) for a Chabrier (2003) IMF using the *i* and *g*-band magnitudes taken in order of priority from Cortese et al. (2012), Gavazzi et al., in prep., or for a few objects from dedicated observations. The assumed distance of each object is that given in Table 1, with the exception of the Virgo cluster for which distances are taken as those of the different subgroups to which each galaxy belongs (see Gavazzi et al. 1999).

Column 5: undergoing perturbation: RP = ram pressure, M = merging, H = harassment. When multiple perturbing mechanisms are at place, the first one reported has been identified as the dominant.

Column 6: projected distance from the X-rays centre of the cluster, in units of r_{200} . For the Virgo cluster, this is the distance from M87 even for those objects probably belonging to other cluster substructures.

Column 7: heliocentric velocities from targeted observations (see column 12), GoldMine Gavazzi et al. (2003a) or NED.

Column 8: electron density of the ICM at the projected distance of the cluster from the X-rays centre of the cluster, derived from Fig. 1, in units of 10^{-4} cm^{-3}

Column 9: HI-deficiency parameter, taken in order of preference from Boselli et al. (2014a), GoldMine (Gavazzi et al. 2003a), or from the dedicated references given in column 10.

Column 10: references to dedicated works on each single object, as follows. References for Virgo: AB11: Abramson et al. (2011), AB14: Abramson & Kenney (2014), AB16: Abramson et al. (2016), AB12: Arrigoni Battaia et al. (2012) B05: Boselli et al. (2005), B06a: Boselli et al. (2006), B16: Boselli et al. (2016a), B16a: Boselli et al. (2016b), B18a: Boselli et al. (2018b), B18b: Boselli et al. (2018a), B21a: Boselli et al. (2021), B21b: Boselli et al. in prep., CH07: Chung et al. (2007), CH09: Chung et al. (2009a), CO06: Cortés et al. (2006), CR20: Cramer et al. (2020), C05: Crowl et al. (2005), CK08: Crowl & Kenney (2008), DB08: Duc & Bournaud (2008), F11: Fumagalli et al. (2011), F18: Fossati et al. (2018), HA07: Haynes et al. (2007), HE10: Hester et al. (2010), K04: Kenney et al. (2004), K14: Kenney et al. (2014), J13: Jáchym et al. (2013), L20: Longobardi et al. (2020b), P10: Pappalardo et al. (2010), SO17: Sorgho et al. (2017), V: VESTIGE survey private comm., VE99: Veilleux et al. (1999), V99: Vollmer et al. (1999), V03: Vollmer (2003), V03a: Vollmer & Huchtmeier (2003), V04a: Vollmer et al. (2004a), V05: Vollmer et al. (2005b), V05a: Vollmer et al. (2005a), V06: Vollmer et al. (2006), V08: Vollmer et al. (2008a), V08a: Vollmer et al. (2008b), V09: Vollmer et al. (2009), V18: Vollmer et al. (2018), V21: Vollmer et al. (2021), YO02: Yoshida et al. (2002), YO04: Yoshida et al. (2004) References for Norma: F16: Fossati et al. (2016), FU14: Fumagalli et al. (2014), LA22: Laudari et al. (2022), J14: Jáchym et al. (2014), J19: Jáchym et al. (2019), SU06: Sun et al. (2006), SU07: Sun et al. (2007a), SU10: Sun et al. (2010), ZH13: Zhang et al. (2013) References for Coma: BD86: Bothun & Dressler (1986), CH20: Chen et al. (2020), CR19: Cramer et al. (2019), CR21: Cramer et al. (2021). F12: Fossati et al. (2012), G89: Gavazzi (1989), G18: Gavazzi et al. (2018b), K15: Kenney et al. (2015), V01a: Vollmer et al. (2001a), Y10: Yagi et al. (2010) References for A1367: B94: Boselli et al. (1994), C17: Consolandi et al. (2017), CO06: Cortese et al. (2006), F19: Fossati et al. (2019), P22: Pedrini et al. (2022), G78: Gavazzi (1978), G84: Gavazzi et al. (1984), G87: Gavazzi & Jaffe (1987), G89: Gavazzi (1989), G01a: Gavazzi et al. (2001a), G01b: Gavazzi et al. (2001b), G03: Gavazzi et al. (2003b), G17: Gavazzi et al. (2017), N82: Nulsen (1982), Q00: Quilis et al. (2000), RO21: Roberts et al. (2021a), S10: Scott et al. (2010), S12: Scott et al. (2012), S13: Scott et al. (2013), S15: Scott et al. (2015), S18: Scott et al. (2018), S22: Scott et al. (2022), Y17: Yagi et al. (2017)

Table 2 Galaxies suffering RPS in nearby clusters

Name	Type	Nuc.	$\log M_{\text{star}}$ M_{\odot}	Process	R/r_{200}	cz km s^{-1}	n_e $\frac{\text{cm}^{-3}}{10^4}$	HI-def	Ref.
Virgo									
NGC4254	SA(s)c	COMP	10.39	H,RP	1.07	2405	0.6	0.06	V05,HA07,DB08,B18a,CH09
NGC4294	SB(s)cd	HII	9.23	RP	0.75	355	1.0	0.04	CH07,CH09
NGC4299	SAB(s)dm	HII	8.82	RP	0.73	232	1.1	-0.11	CH07,CH09
NGC4302	Sc	LIN	10.44	RP	0.94	1150	0.7	0.50	CH07,CH09,B16a
NGC4330	Scd?	HII	9.52	RP	0.63	1563	1.3	0.92	CH07,CH09,AB11,F18,L20,V21
NGC4388	SA(s)b	AGN	10.14	RP	0.38	2515	2.7	0.98	VE99,YO02,V03a,YO04,CK08,CH09,P10,V18
NGC4396	SAd	HII	9.25	RP	1.03	-122	0.7	0.20	CH07,CH09,B16a
NGC4402	Sb	HII	10.04	RP	0.41	230	2.4	0.83	C05,CK08,CH09,AB14,AB16,B16a,CR20
NGC4424	SB(s)a?	HII	10.17	RP,M	0.92	437	0.8	0.98	CO06,CH07,CK08,CH09,SO17,B18b
NGC4438	SA(s)0a pec	LIN	10.66	H,RP	0.29	104	3.9	1.20	B05,V05a,V09
NGC4469	SB(s)a?	COMP	10.64	RP	1.08	587	0.6	1.88	B16a,B21b
NGC4470	Sa?	HII	9.20	RP	1.36	2341	0.4	0.32	B16a,V
NGC4491	SB(s)a	HII	9.55	RP	0.27	497	4.4	>1.27	B16a,V
NGC4501	SA(rs)b	LIN	10.98	RP	0.61	2282	1.4	0.58	B16a,V08a
NGC4506	Sa pec	HII	9.39	RP	0.32	737	3.4	>1.31	B16a,V
NGC4522	SB(s)cd	HII	9.38	RP	0.97	2329	0.7	0.68	K04,V06,V08,CK08,CH09,AB16,B16a,L20
NGC4548	SB(rs)b	LIN	10.74	RP	0.71	479	1.1	0.94	V99
NGC4569	SAB(rs)ab	LIN	10.66	RP	0.50	-221	1.8	1.05	V04a,B06a,CK08,B16,B16a
NGC4654	SAB(rs)cd	HII	10.14	RP,H	0.99	1038	0.7	-0.05	V03,CH07,CH09,B16a,L20
IC3105	Im:	HII	7.89	RP	0.98	-167	0.7	0.41	V
IC3412	Irr	HII	8.36	RP	0.72	728	1.1	1.06	V
IC3418	IBm	PAS	9.06	RP	0.30	38	3.7	>2.36	H10, F11,J13,K14,V
IC3476	IB(s)m	HII	9.03	RP	0.51	-170	1.8	0.66	B21a
UGC7636	Im	-	8.20	RP,H	1.32	473	0.5	0.85	AB12
Norma									
ESO137-001	SBC?	HII	9.81	RP	0.18	4461	8.5	-	SU06,SU07,SU10,FU14,J14,F16,J19
ESO137-002	S0?	-	10.54	RP	0.13	5691	12.0	-	SU10,ZH13,LA22
Coma									
NGC4848	Sab	COMP	10.32	RP	0.49	7193	2.5	0.25	BD86,G89,V01a,F12,G18,CH20,RO21
NGC4853	S0	COMP	10.37	RP	0.46	7676	2.8	-	Y10,G18,RO21
NGC4858	Sb	HII	9.40	RP	0.25	9430	8.5	0.96	BD86,Y10,G18,CH20,RO21
NGC4911	Sa	LIN	10.89	RP	0.26	7995	7.9	0.31	Y10,G18
NGC4921	Sb	LIN	11.34	RP	0.33	5481	5.3	0.73	K15,G18,CR21
IC837	S0a	HII	10.00	RP	1.40	7230	0.3	0.40	RO21
IC3913	Sc	HII	9.82	RP	0.99	7525	0.6	0.18	RO21
IC3949	Sa	COMP	10.42	RP	0.27	7553	7.7	1.01	Y10,G18,CH20,RO21
IC4040	Sdm	HII	9.65	RP	0.16	7637	16.2	0.45	BD86,Y10,G18,CH20,RO21
CGCG160-020	BCD	HII	9.22	RP	0.90	4968	0.7	0.26	RO21
CGCG160-033	S0a	AGN	10.02	RP	1.18	6249	0.4	-	RO21
CGCG160-058	Sbc	HII	10.07	RP	0.77	7616	0.9	0.17	RO21
CGCG160-064	Pec	HII	9.16	RP	0.70	7368	1.2	0.92	RO21
CGCG160-067	Pec	HII	9.51	RP	0.77	7664	1.0	-0.18	RO21
CGCG160-073	Sa	HII	9.74	RP	0.35	5435	4.6	0.69	BD86,Y10,G18,CH20,RO21
CGCG160-076	Sc	HII	9.28	RP	0.59	5358	1.7	-0.32	RO21
CGCG160-086	Sb	HII	9.31	RP	0.32	7476	5.6	0.59	BD86,CH20,RO21
CGCG160-098	Sc	HII	9.96	RP	0.70	8762	1.2	0.31	BD86,RO21
CGCG160-106	S0a	HII	9.91	RP	0.55	6902	1.9	0.34	BD86,RO21
CGCG160-108	Sb	HII	9.49	RP	0.54	8202	2.0	0.89	RO21
CGCG160-127	Sc	HII	9.27	RP	1.15	5500	0.4	-0.05	RO21
CGCG160-243	BCD	HII	9.26	RP	0.10	5316	25.9	-	Y10,J17,G18,CR19,CH20,RO21
GMP2601	BCD	HII	8.96	RP	0.43	5602	3.1	-	RO21
GMP2923	BCD	PSB	8.75	RP	0.18	8726	14.3	-	Y10,G18
GMP3016	S..	-	7.49	RP	0.10	7770	25.4	-	Y10,G18
GMP3071	BCD	HII	8.90	RP	0.20	8975	12.2	-	Y10,G18
GMP3271	Pec	HII	9.20	RP	0.36	5007	4.5	-	Y10,G18,RO21
GMP3618	Sa	HII	9.46	RP	0.78	8412	0.9	-	RO21
GMP4060	Sm	PSB	9.12	RP	0.34	8753	4.9	-	Y10,G18
GMP4106	Pec	HII	8.69	RP	1.11	7467	0.4	-0.05	RO21
GMP4232	S..	-	7.39	RP	0.49	7285	2.4	-	Y10,G18
GMP4351	BCD	HII	9.18	RP	0.69	7447	1.2	-0.24	RO21
GMP4555	Pec	HII	9.75	RP	0.46	8142	2.8	-	G18,CH20,RO21
GMP4570	Pec	HII	8.53	RP	0.46	4579	2.8	0.27	G18,CH20
GMP4629	BCD	HII	8.47	RP	0.51	6935	2.2	-	G18,CH20
A1367									
UGC6697	Pec	HII	10.13	RP	0.38	6727	5.1	0.00	N82,G84,G87,G89,B94,G95,G01b,S10,S18,C17,Y17
UGC6697N	Pec	HII	8.78	RP, H	0.37	7542	5.0	-	C17
CGCG097-026	Pec	HII	9.86	H, RP	2.24	6195	0.1	-0.66	S12,S22
CGCG097-073	Pec	HII	9.27	RP, H	0.57	7298	2.2	-0.09	G87,G89,B94,Q00,G01a,Y17,P22,RO21
CGCG097-079	Pec	HII	9.08	RP, H	0.52	7026	2.6	0.17	G87,G89,B94,G01a,S13,S15,Y17,P22,RO21
CGCG097-092	Sb	HII	9.62	RP	0.56	6536	2.3	0.18	Y17
CGCG097-093	Sc	HII	9.22	RP, H	0.20	7298	13.0	0.47	Y17
CGCG097-114	Pec	HII	9.22	H, RP	0.05	8425	48.1	-0.32	G03,C06,F19,RO21
CGCG097-120	Sa	LIN	10.53	RP	0.08	5620	36.1	0.90	G03,F19
CGCG097-122	Pec	HII	10.11	RP, H	0.32	6721	6.2	0.35	Y17
CGCG097-125	S0a	HII	10.32	M, RP	0.08	8311	36.0	-0.05	G03,C06,F19
FGC1287	Sdm	HII	9.81	RP, H	1.58	6825	0.2	0.00	S12
J114432.1+200623	BCD	HII	9.87	RP	0.43	7214	3.9	-	G17

Acknowledgements We warmly thank the two anonymous referees for their accurate reading of the text and for their constructive comments and suggestions which helped improving the completeness and clarity of the manuscript. We warmly thank S. Boissier, G. Consolandi, G. Gavazzi, A. Longobardi, A. Pedrini, P. Serra, S. Tonnesen, M. Yagi for constructive discussions and for giving us access to different set of multifrequency data and for their help in the preparation of some figures presented along the text. We also thank C. Ge and S. Laudari on the help on several figures. AB acknowledges financial support from "Programme National de Cosmologie and Galaxies" (PNCG) funded by CNRS/INSU-IN2P3-INP, CEA and CNES, France. MF acknowledges funding from the European Research Council (ERC) (grant agreement No 757535). MS acknowledges support provided by the SAO grants GO6-17111X and GO0-21118X, the NSF grant 1714764 and the USRA grant 09-0221. Part of the results presented in this work have been gathered or collected from archival datasets by the VESTIGE survey team. We thus warmly thank all members of this collaboration in allowing us to use and reproduce some of their work and results obtained during this project.

References

- Abadi, M. G., Moore, B., & Bower, R. G. 1999, *MNRAS*, 308, 947
Abramson, A., Kenney, J., Crowl, H., & Tal, T. 2016, *AJ*, 152, 32
Abramson, A. & Kenney, J. D. P. 2014, *AJ*, 147, 63
Abramson, A., Kenney, J. D. P., Crowl, H. H., et al. 2011, *AJ*, 141, 164
Ahad, S. L., Bahé, Y. M., Hoekstra, H., van der Burg, R. F. J., & Muzzin, A. 2021, *MNRAS*, 504, 1999
Andersen, V. & Owen, F. N. 1995, *AJ*, 109, 1582
Anderson, M. E. & Sunyaev, R. 2016, *MNRAS*, 459, 2806
Andreon, S., Newman, A. B., Trinchieri, G., et al. 2014, *A&A*, 565, A120
Armitage, T. J., Barnes, D. J., Kay, S. T., et al. 2018, *MNRAS*, 474, 3746
Arrigoni Battaia, F., Gavazzi, G., Fumagalli, M., et al. 2012, *A&A*, 543, A112
Arthur, J., Pearce, F. R., Gray, M. E., et al. 2019, *MNRAS*, 484, 3968
Asplund, M., Grevesse, N., Sauval, A. J., & Scott, P. 2009, *ARA&A*, 47, 481
Ayromlou, M., Kauffmann, G., Yates, R. M., Nelson, D., & White, S. D. M. 2021, *MNRAS*, 505, 492
Bahé, Y. M. & McCarthy, I. G. 2015, *MNRAS*, 447, 969
Bahé, Y. M., McCarthy, I. G., Balogh, M. L., & Font, A. S. 2013, *MNRAS*, 430, 3017
Balogh, M. L., Gilbank, D. G., Muzzin, A., et al. 2017, *MNRAS*, 470, 4168
Balogh, M. L., McGee, S. L., Mok, A., et al. 2016, *MNRAS*, 456, 4364
Balogh, M. L., McGee, S. L., Mok, A., et al. 2014, *MNRAS*, 443, 2679
Balogh, M. L., Navarro, J. F., & Morris, S. L. 2000, *ApJ*, 540, 113
Barger, K. A., Nidever, D. L., Huey-You, C., et al. 2020, *ApJ*, 902, 154
Beck, R. & Krause, M. 2005, *Astronomische Nachrichten*, 326, 414
Behroozi, P. S., Wechsler, R. H., & Conroy, C. 2013, *ApJ*, 770, 57
Bekki, K. 2009, *MNRAS*, 399, 2221
Bekki, K. 2014, *MNRAS*, 438, 444
Bekki, K. & Couch, W. J. 2003, *ApJ*, 596, L13
Bekki, K., Couch, W. J., & Shioya, Y. 2002, *ApJ*, 577, 651
Belfiore, F., Maiolino, R., Maraston, C., et al. 2016, *MNRAS*, 461, 3111
Bellhouse, C., Jaffé, Y. L., McGee, S. L., et al. 2019, *MNRAS*, 485, 1157
Bellhouse, C., McGee, S. L., Smith, R., et al. 2021, *MNRAS*, 500, 1285
Benítez-Llambay, A., Navarro, J. F., Abadi, M. G., et al. 2013, *ApJ*, 763, L41
Berrier, J. C., Stewart, K. R., Bullock, J. S., et al. 2009, *ApJ*, 690, 1292
Bialas, D., Lisker, T., Olczak, C., Spurzem, R., & Kotulla, R. 2015, *A&A*, 576, A103
Bianconi, M., Smith, G. P., Haines, C. P., et al. 2020, *MNRAS*, 492, 4599
Bidaran, B., Pasquali, A., Lisker, T., et al. 2020, *MNRAS*, 497, 1904
Biffi, V., Mernier, F., & Medvedev, P. 2018, *Space Sci. Rev.*, 214, 123
Bigiel, F. & Blitz, L. 2012, *ApJ*, 756, 183
Bigiel, F., Leroy, A. K., Walter, F., et al. 2011, *ApJ*, 730, L13

- Binney, J. & Tremaine, S. 2008, *Galactic Dynamics: Second Edition* (Princeton University Press)
- Biviano, A. & Poggianti, B. M. 2009, *A&A*, 501, 419
- Blanton, M. R. & Moustakas, J. 2009, *ARA&A*, 47, 159
- Blitz, L. & Rosolowsky, E. 2006, *ApJ*, 650, 933
- Bogdán, Á., Bourdin, H., Forman, W. R., et al. 2017, *ApJ*, 850, 98
- Böhringer, H., Dolag, K., & Chon, G. 2012, *A&A*, 539, A120
- Boissier, S., Boselli, A., Duc, P.-A., et al. 2012, *A&A*, 545, A142
- Bolatto, A. D., Leroy, A. K., Rosolowsky, E., Walter, F., & Blitz, L. 2008, *ApJ*, 686, 948
- Boselli, A. 2011, *A Panchromatic View of Galaxies* (Wiley-VCH)
- Boselli, A., Boissier, S., Cortese, L., et al. 2009, *ApJ*, 706, 1527
- Boselli, A., Boissier, S., Cortese, L., & Gavazzi, G. 2008a, *ApJ*, 674, 742
- Boselli, A., Boissier, S., Cortese, L., & Gavazzi, G. 2008b, *A&A*, 489, 1015
- Boselli, A., Boissier, S., Cortese, L., et al. 2005, *ApJ*, 623, L13
- Boselli, A., Boissier, S., Cortese, L., et al. 2006, *ApJ*, 651, 811
- Boselli, A., Boissier, S., Heinis, S., et al. 2011, *A&A*, 528, A107
- Boselli, A., Casoli, F., & Lequeux, J. 1995, *A&AS*, 110, 521
- Boselli, A., Cortese, L., & Boquien, M. 2014a, *A&A*, 564, A65
- Boselli, A., Cortese, L., Boquien, M., et al. 2014b, *A&A*, 564, A67
- Boselli, A., Cortese, L., Boquien, M., et al. 2014c, *A&A*, 564, A66
- Boselli, A., Cuillandre, J. C., Fossati, M., et al. 2016a, *A&A*, 587, A68
- Boselli, A., Eales, S., Cortese, L., et al. 2010, *PASP*, 122, 261
- Boselli, A., Epinat, B., Contini, T., et al. 2019a, *A&A*, 631, A114
- Boselli, A., Fossati, M., Consolandi, G., et al. 2018a, *A&A*, 620, A164
- Boselli, A., Fossati, M., Cuillandre, J. C., et al. 2018b, *A&A*, 615, A114
- Boselli, A., Fossati, M., Ferrarese, L., et al. 2018c, *A&A*, 614, A56
- Boselli, A., Fossati, M., Gavazzi, G., et al. 2015, *A&A*, 579, A102
- Boselli, A., Fossati, M., Longobardi, A., et al. 2020, *A&A*, 634, L1
- Boselli, A., Fossati, M., Longobardi, A., et al. 2019b, *A&A*, 623, A52
- Boselli, A., Fossati, M., Longobardi, A., et al. 2022, *A&A*, 659, A46
- Boselli, A. & Gavazzi, G. 2006, *PASP*, 118, 517
- Boselli, A. & Gavazzi, G. 2009, *A&A*, 508, 201
- Boselli, A. & Gavazzi, G. 2014, *A&A Rev.*, 22, 74
- Boselli, A., Gavazzi, G., Combes, F., Lequeux, J., & Casoli, F. 1994, *A&A*, 285, 69
- Boselli, A., Gavazzi, G., Donas, J., & Scodreggio, M. 2001, *AJ*, 121, 753
- Boselli, A., Lequeux, J., & Gavazzi, G. 2002, *A&A*, 384, 33
- Boselli, A., Lupi, A., Epinat, B., et al. 2021, *A&A*, 646, A139
- Boselli, A., Roehly, Y., Fossati, M., et al. 2016b, *A&A*, 596, A11
- Boselli, A., Voyer, E., Boissier, S., et al. 2014d, *A&A*, 570, A69
- Bothun, G. D. & Dressler, A. 1986, *ApJ*, 301, 57
- Botteon, A., van Weeren, R. J., Brunetti, G., et al. 2020, *MNRAS*, 499, L11
- Bracco, A., Benjamin, R. A., Alves, M. I. R., et al. 2020, *A&A*, 636, L8
- Bravo-Alfaro, H., Cayatte, V., van Gorkom, J. H., & Balkowski, C. 2000, *AJ*, 119, 580
- Bravo-Alfaro, H., Cayatte, V., van Gorkom, J. H., & Balkowski, C. 2001, *A&A*, 379, 347
- Bregman, J. N., Anderson, M. E., & Dai, X. 2010, *ApJ*, 716, L63
- Bretherton, C. F., Moss, C., & James, P. A. 2013, *A&A*, 553, A67
- Brown, T., Catinella, B., Cortese, L., et al. 2017, *MNRAS*, 466, 1275
- Bryan, G. L. & Norman, M. L. 1998, *ApJ*, 495, 80
- Byrd, G. & Valtonen, M. 1990, *ApJ*, 350, 89
- Calura, F., Bellazzini, M., & D’Ercole, A. 2020, *MNRAS*, 499, 5873
- Campitiello, M. G., Ignesti, A., Gitti, M., et al. 2021, *ApJ*, 911, 144
- Carter, D., Goudfrooij, P., Mobasher, B., et al. 2008, *ApJS*, 176, 424
- Castignani, G., Combes, F., Jablonka, P., et al. 2022, *A&A*, 657, A9
- Catinella, B., Giovanelli, R., & Haynes, M. P. 2006, *ApJ*, 640, 751
- Catinella, B., Schiminovich, D., Cortese, L., et al. 2013, *MNRAS*, 436, 34
- Cayatte, V., Kotanyi, C., Balkowski, C., & van Gorkom, J. H. 1994, *AJ*, 107, 1003
- Cayatte, V., van Gorkom, J. H., Balkowski, C., & Kotanyi, C. 1990, *AJ*, 100, 604
- Chabrier, G. 2003, *PASP*, 115, 763

- Chemin, L., Balkowski, C., Cayatte, V., et al. 2006, MNRAS, 366, 812
- Chen, H., Sun, M., Yagi, M., et al. 2020, MNRAS, 496, 4654
- Chiboucas, K., Tully, R. B., Marzke, R. O., et al. 2011, ApJ, 737, 86
- Chung, A., van Gorkom, J. H., Kenney, J. D. P., Crowl, H., & Vollmer, B. 2009a, AJ, 138, 1741
- Chung, A., van Gorkom, J. H., Kenney, J. D. P., & Vollmer, B. 2007, ApJ, 659, L115
- Chung, E. J., Rhee, M.-H., Kim, H., et al. 2009b, ApJS, 184, 199
- Chung, E. J., Yun, M. S., Verheijen, M. A. W., & Chung, A. 2017, ApJ, 843, 50
- Churazov, E., Khabibullin, I., Lyskova, N., Sunyaev, R., & Bykov, A. M. 2021, A&A, 651, A41
- Chyży, K. T., Ehle, M., & Beck, R. 2007, A&A, 474, 415
- Chyży, K. T., Jurusik, W., Piotrowska, J., et al. 2018, A&A, 619, A36
- Ciesla, L., Boselli, A., Elbaz, D., et al. 2016, A&A, 585, A43
- Ciesla, L., Boselli, A., Smith, M. W. L., et al. 2012, A&A, 543, A161
- Clarke, A. J., Debattista, V. P., Roškar, R., & Quinn, T. 2017, MNRAS, 465, L79
- Colless, M. & Dunn, A. M. 1996, ApJ, 458, 435
- Combes, F., Baker, A. J., Schinnerer, E., et al. 2009, A&A, 503, 73
- Combes, F., Dupraz, C., Casoli, F., & Pagani, L. 1988, A&A, 203, L9
- Conselice, C. J., Bershad, M. A., & Jangren, A. 2000, ApJ, 529, 886
- Conselice, C. J., Gallagher, John S., I., & Wyse, R. F. G. 2001, AJ, 122, 2281
- Consolandi, G., Gavazzi, G., Fossati, M., et al. 2017, A&A, 606, A83
- Constantin, A. & Vogeley, M. S. 2006, ApJ, 650, 727
- Contini, E. 2021, Galaxies, 9, 60
- Corbelli, E., Bianchi, S., Cortese, L., et al. 2012, A&A, 542, A32
- Cortés, J. R., Kenney, J. D. P., & Hardy, E. 2006, AJ, 131, 747
- Cortese, L., Bekki, K., Boselli, A., et al. 2016, MNRAS, 459, 3574
- Cortese, L., Boissier, S., Boselli, A., et al. 2012, A&A, 544, A101
- Cortese, L., Catinella, B., & Smith, R. 2021, PASA, 38, e035
- Cortese, L., Davies, J. I., Pohlen, M., et al. 2010, A&A, 518, L49
- Cortese, L., Fritz, J., Bianchi, S., et al. 2014, MNRAS, 440, 942
- Cortese, L., Gavazzi, G., Boselli, A., et al. 2006, A&A, 453, 847
- Cortese, L., Gavazzi, G., Boselli, A., & Iglesias-Paramo, J. 2004a, A&A, 416, 119
- Cortese, L., Gavazzi, G., Boselli, A., Iglesias-Paramo, J., & Carrasco, L. 2004b, A&A, 425, 429
- Cortese, L. & Hughes, T. M. 2009, MNRAS, 400, 1225
- Cortese, L., Marcillac, D., Richard, J., et al. 2007, MNRAS, 376, 157
- Cortese, L., van de Sande, J., Lagos, C. P., et al. 2019, MNRAS, 485, 2656
- Côté, P., Piatek, S., Ferrarese, L., et al. 2006, ApJS, 165, 57
- Cowie, L. L. & McKee, C. F. 1977, ApJ, 211, 135
- Cowie, L. L. & Songaila, A. 1977, Nature, 266, 501
- Cramer, W. J., Kenney, J. D. P., Cortes, J. R., et al. 2020, ApJ, 901, 95
- Cramer, W. J., Kenney, J. D. P., Sun, M., et al. 2019, ApJ, 870, 63
- Cramer, W. J., Kenney, J. D. P., Tonnesen, S., et al. 2021, ApJ, 921, 22
- Croston, J. H., Pratt, G. W., Böhringer, H., et al. 2008, A&A, 487, 431
- Crowl, H. H. & Kenney, J. D. P. 2006, ApJ, 649, L75
- Crowl, H. H. & Kenney, J. D. P. 2008, AJ, 136, 1623
- Crowl, H. H., Kenney, J. D. P., van Gorkom, J. H., & Vollmer, B. 2005, AJ, 130, 65
- Cybulski, R., Yun, M. S., Fazio, G. G., & Gutermuth, R. A. 2014, MNRAS, 439, 3564
- Davies, J. I., Baes, M., Bendo, G. J., et al. 2010, A&A, 518, L48
- Davies, J. I., Bianchi, S., Baes, M., et al. 2013, MNRAS, 428, 834
- de Jong, T., Klein, U., Wielebinski, R., & Wunderlich, E. 1985, A&A, 147, L6
- De Looze, I., Baes, M., Zibetti, S., et al. 2010, A&A, 518, L54
- De Lucia, G., Weinmann, S., Poggianti, B. M., Aragón-Salamanca, A., & Zaritsky, D. 2012, MNRAS, 423, 1277
- Deb, T., Verheijen, M. A. W., Gullieuszik, M., et al. 2020, MNRAS, 494, 5029
- Dickey, J. M. 1997, AJ, 113, 1939
- Dickey, J. M. & Gavazzi, G. 1991, ApJ, 373, 347
- Dolag, K., Borgani, S., Murante, G., & Springel, V. 2009, MNRAS, 399, 497

- Domainko, W., Mair, M., Kapferer, W., et al. 2006, *A&A*, 452, 795
- Donas, J., Buat, V., Milliard, B., & Laget, M. 1990, *A&A*, 235, 60
- Donas, J., Milliard, B., & Laget, M. 1995, *A&A*, 303, 661
- Donnari, M., Pillepich, A., Joshi, G. D., et al. 2021, *MNRAS*, 500, 4004
- Donnert, J., Vazza, F., Brügggen, M., & ZuHone, J. 2018, *Space Sci. Rev.*, 214, 122
- Draine, B. T. 2003, *ARA&A*, 41, 241
- Draine, B. T. & Salpeter, E. E. 1979, *ApJ*, 231, 77
- Dressler, A. 1980, *ApJ*, 236, 351
- Dressler, A. 2004, *Clusters of Galaxies: Probes of Cosmological Structure and Galaxy Evolution*, 206
- Dressler, A., Oemler, Jr., A., Couch, W. J., et al. 1997, *ApJ*, 490, 577
- Duc, P.-A. & Bournaud, F. 2008, *ApJ*, 673, 787
- Durret, F., Chiche, S., Lobo, C., & Jauzac, M. 2021, *A&A*, 648, A63
- Ebeling, H. & Kalita, B. S. 2019, *ApJ*, 882, 127
- Ebeling, H., Stephenson, L. N., & Edge, A. C. 2014, *ApJ*, 781, L40
- Eckert, D., Gaspari, M., Gastaldello, F., Le Brun, A. M. C., & O'Sullivan, E. 2021, *Universe*, 7, 142
- Ehlert, S., Allen, S. W., Brandt, W. N., et al. 2015, *MNRAS*, 446, 2709
- Ehlert, S., von der Linden, A., Allen, S. W., et al. 2014, *MNRAS*, 437, 1942
- Ellison, S. L., Patton, D. R., Mendel, J. T., & Scudder, J. M. 2011, *MNRAS*, 418, 2043
- Ellison, S. L., Patton, D. R., Simard, L., & McConnachie, A. W. 2008, *AJ*, 135, 1877
- Elmegreen, D. M., Elmegreen, B. G., Frogel, J. A., et al. 2002, *AJ*, 124, 777
- Engargiola, G., Plambeck, R. L., Rosolowsky, E., & Blitz, L. 2003, *ApJS*, 149, 343
- Fabello, S., Kauffmann, G., Catinella, B., et al. 2012, *MNRAS*, 427, 2841
- Faltenbacher, A., Kravtsov, A. V., Nagai, D., & Gottlöber, S. 2005, *MNRAS*, 358, 139
- Farouki, R. & Shapiro, S. L. 1980, *ApJ*, 241, 928
- Feretti, L. & Giovannini, G. 2008, in *A Pan-Chromatic View of Clusters of Galaxies and the Large-Scale Structure*, ed. M. Plionis, O. López-Cruz, & D. Hughes, Vol. 740, 24
- Ferland, G. J., Fabian, A. C., Hatch, N. A., et al. 2009, *MNRAS*, 392, 1475
- Ferrarese, L., Côté, P., Cuillandre, J.-C., et al. 2012, *ApJS*, 200, 4
- Fielding, D. B., Ostriker, E. C., Bryan, G. L., & Jermyn, A. S. 2020, *ApJ*, 894, L24
- Foltz, R., Wilson, G., Muzzin, A., et al. 2018, *ApJ*, 866, 136
- Forman, W., Jones, C., Churazov, E., et al. 2007, *ApJ*, 665, 1057
- Fossati, M., Fumagalli, M., Boselli, A., et al. 2016, *MNRAS*, 455, 2028
- Fossati, M., Fumagalli, M., Gavazzi, G., et al. 2019, *MNRAS*, 484, 2212
- Fossati, M., Gavazzi, G., Boselli, A., & Fumagalli, M. 2012, *A&A*, 544, A128
- Fossati, M., Gavazzi, G., Savorgnan, G., et al. 2013, *A&A*, 553, A91
- Fossati, M., Mendel, J. T., Boselli, A., et al. 2018, *A&A*, 614, A57
- Fossati, M., Wilman, D. J., Mendel, J. T., et al. 2017, *ApJ*, 835, 153
- Foster, C., Hopkins, A. M., Gunawardhana, M., et al. 2012, *A&A*, 547, A79
- Freeman, K. C. 1970, *ApJ*, 160, 811
- Fuchs, B. & von Linden, S. 1998, *MNRAS*, 294, 513
- Fujita, Y. 2001, *ApJ*, 550, 612
- Fujita, Y. 2004, *PASJ*, 56, 29
- Fujita, Y., Takizawa, M., Nagashima, M., & Enoki, M. 1999, *PASJ*, 51, L1
- Fumagalli, M., Fossati, M., Hau, G. K. T., et al. 2014, *MNRAS*, 445, 4335
- Fumagalli, M., Gavazzi, G., Scaramella, R., & Franzetti, P. 2011, *A&A*, 528, A46
- Fumagalli, M., Krumholz, M. R., Prochaska, J. X., Gavazzi, G., & Boselli, A. 2009, *ApJ*, 697, 1811
- Galametz, A., Pentericci, L., Castellano, M., et al. 2018, *MNRAS*, 475, 4148
- Gallazzi, A. R., Pasquali, A., Zibetti, S., & Barbera, F. L. 2021, *MNRAS*, 502, 4457
- Gatto, A., Fraternali, F., Read, J. I., et al. 2013, *MNRAS*, 433, 2749
- Gavazzi, G. 1978, *A&A*, 69, 355
- Gavazzi, G. 1989, *ApJ*, 346, 59
- Gavazzi, G., Bonfanti, C., Sanvito, G., Boselli, A., & Scodreggio, M. 2002, *ApJ*, 576, 135
- Gavazzi, G. & Boselli, A. 1999, *A&A*, 343, 93
- Gavazzi, G., Boselli, A., Cortese, L., et al. 2006a, *A&A*, 446, 839
- Gavazzi, G., Boselli, A., Donati, A., Franzetti, P., & Scodreggio, M. 2003a, *A&A*, 400, 451

- Gavazzi, G., Boselli, A., & Kennicutt, R. 1991, *AJ*, 101, 1207
- Gavazzi, G., Boselli, A., Mayer, L., et al. 2001a, *ApJ*, 563, L23
- Gavazzi, G., Boselli, A., Scodreggio, M., Pierini, D., & Belsole, E. 1999, *MNRAS*, 304, 595
- Gavazzi, G., Boselli, A., van Driel, W., & O’Neil, K. 2005, *A&A*, 429, 439
- Gavazzi, G., Catinella, B., Carrasco, L., Boselli, A., & Contursi, A. 1998, *AJ*, 115, 1745
- Gavazzi, G., Consolandi, G., Belladitta, S., Boselli, A., & Fossati, M. 2018a, *A&A*, 615, A104
- Gavazzi, G., Consolandi, G., Dotti, M., et al. 2013a, *A&A*, 558, A68
- Gavazzi, G., Consolandi, G., Gutierrez, M. L., Boselli, A., & Yoshida, M. 2018b, *A&A*, 618, A130
- Gavazzi, G., Consolandi, G., Viscardi, E., et al. 2015, *A&A*, 576, A16
- Gavazzi, G., Consolandi, G., Yagi, M., & Yoshida, M. 2017, *A&A*, 606, A131
- Gavazzi, G., Contursi, A., Carrasco, L., et al. 1995, *A&A*, 304, 325
- Gavazzi, G., Cortese, L., Boselli, A., et al. 2003b, *ApJ*, 597, 210
- Gavazzi, G., Fumagalli, M., Cucciati, O., & Boselli, A. 2010, *A&A*, 517, A73
- Gavazzi, G., Fumagalli, M., Fossati, M., et al. 2013b, *A&A*, 553, A89
- Gavazzi, G. & Jaffe, W. 1985, *ApJ*, 294, L89
- Gavazzi, G. & Jaffe, W. 1986, *ApJ*, 310, 53
- Gavazzi, G. & Jaffe, W. 1987, *A&A*, 186, L1
- Gavazzi, G., Marcelin, M., Boselli, A., et al. 2001b, *A&A*, 377, 745
- Gavazzi, G., O’Neil, K., Boselli, A., & van Driel, W. 2006b, *A&A*, 449, 929
- Gavazzi, G., Savorgnan, G., & Fumagalli, M. 2011, *A&A*, 534, A31
- Gavazzi, G., Tarenghi, M., Jaffe, W., Butcher, H., & Boksenberg, A. 1984, *A&A*, 137, 235
- Ge, C., Luo, R., Sun, M., et al. 2021, *MNRAS*, 505, 4702
- Ge, C., Sun, M., Liu, R.-Y., et al. 2019, *MNRAS*, 486, L36
- George, K., Poggianti, B. M., Bellhouse, C., et al. 2019, *MNRAS*, 487, 3102
- Gerhard, O., Arnaboldi, M., Freeman, K. C., & Okamura, S. 2002, *ApJ*, 580, L121
- Ghirardini, V., Bulbul, E., Kraft, R., et al. 2021, *ApJ*, 910, 14
- Gioia, I. M., Gregorini, L., & Klein, U. 1982, *A&A*, 116, 164
- Giovanelli, R. & Haynes, M. P. 1985, *ApJ*, 292, 404
- Gjergo, E., Palla, M., Matteucci, F., et al. 2020, *MNRAS*, 493, 2782
- Gnedin, O. Y. 2003a, *ApJ*, 589, 752
- Gnedin, O. Y. 2003b, *ApJ*, 582, 141
- Gómez, P. L., Nichol, R. C., Miller, C. J., et al. 2003, *ApJ*, 584, 210
- Gonzalez, A. H., Sivanandam, S., Zabludoff, A. I., & Zaritsky, D. 2013, *ApJ*, 778, 14
- Gonzalez, A. H., Zabludoff, A. I., & Zaritsky, D. 2005, *ApJ*, 618, 195
- Gordon, Y. A., Pimblett, K. A., Owers, M. S., et al. 2018, *MNRAS*, 475, 4223
- Gronke, M. & Oh, S. P. 2018, *MNRAS*, 480, L111
- Gronke, M., Oh, S. P., Ji, S., & Norman, C. 2022, *MNRAS*, 511, 859
- Gu, L., Yagi, M., Nakazawa, K., et al. 2013, *ApJ*, 777, L36
- Gullieuszik, M., Poggianti, B. M., McGee, S. L., et al. 2020, *ApJ*, 899, 13
- Gullieuszik, M., Poggianti, B. M., Moretti, A., et al. 2017, *ApJ*, 846, 27
- Gunn, J. E. & Gott, III, J. R. 1972, *ApJ*, 176, 1
- Guo, Q., White, S., Angulo, R. E., et al. 2013, *MNRAS*, 428, 1351
- Gupta, A., Yuan, T., Martizzi, D., Tran, K.-V. H., & Kewley, L. J. 2017, *ApJ*, 842, 75
- Gutiérrez, C. M. & López-Corredoira, M. 2014, *A&A*, 571, A66
- Gutiérrez, C. M. & López-Corredoira, M. 2017, *ApJ*, 835, 111
- Haan, S. & Braun, R. 2014, *MNRAS*, 443, 186
- Haines, C. P., Gargiulo, A., La Barbera, F., et al. 2007, *MNRAS*, 381, 7
- Haines, C. P., La Barbera, F., Mercurio, A., Merluzzi, P., & Busarello, G. 2006, *ApJ*, 647, L21
- Haines, C. P., Pereira, M. J., Smith, G. P., et al. 2015, *ApJ*, 806, 101
- Haines, C. P., Smith, G. P., Egami, E., et al. 2009, *ApJ*, 704, 126
- Han, S., Smith, R., Choi, H., et al. 2018, *ApJ*, 866, 78
- Haynes, M. P. & Giovanelli, R. 1984, *AJ*, 89, 758
- Haynes, M. P., Giovanelli, R., & Kent, B. R. 2007, *ApJ*, 665, L19
- Healy, J., Blyth, S. L., Verheijen, M. A. W., et al. 2021, *A&A*, 650, A76
- Helfer, T. T., Thornley, M. D., Regan, M. W., et al. 2003, *ApJS*, 145, 259

- Helou, G., Soifer, B. T., & Rowan-Robinson, M. 1985, *ApJ*, 298, L7
- Henderson, B. & Bekki, K. 2016, *ApJ*, 822, L33
- Henriksen, M. & Byrd, G. 1996, *ApJ*, 459, 82
- Henriques, B. M. B., White, S. D. M., Thomas, P. A., et al. 2015, *MNRAS*, 451, 2663
- Henriques, B. M. B., White, S. D. M., Thomas, P. A., et al. 2017, *MNRAS*, 469, 2626
- Hernández-Fernández, J. D., Haines, C. P., Diaferio, A., et al. 2014, *MNRAS*, 438, 2186
- Hess, K. M. & Wilcots, E. M. 2013, *AJ*, 146, 124
- Hester, J. A. 2006, *ApJ*, 647, 910
- Hester, J. A., Seibert, M., Neill, J. D., et al. 2010, *ApJ*, 716, L14
- Hidaka, M. & Sofue, Y. 2002, *PASJ*, 54, 33
- Hirschmann, M., De Lucia, G., & Fontanot, F. 2016, *MNRAS*, 461, 1760
- Hollenbach, D. J. & Tielens, A. G. G. M. 1997, *ARA&A*, 35, 179
- Hu, W., Cortese, L., Staveley-Smith, L., et al. 2021, *MNRAS*, 0, 0
- Hughes, T. M. & Cortese, L. 2009, *MNRAS*, 396, L41
- Hughes, T. M., Cortese, L., Boselli, A., Gavazzi, G., & Davies, J. I. 2013, *A&A*, 550, A115
- Ichinohe, Y., Simionescu, A., Werner, N., & Takahashi, T. 2017, *MNRAS*, 467, 3662
- Ignesti, A., Vulcani, B., Poggianti, B. M., et al. 2022, *ApJ*, 924, 64
- Iodice, E., Capaccioli, M., Grado, A., et al. 2016, *ApJ*, 820, 42
- Jáchym, P., Combes, F., Cortese, L., Sun, M., & Kenney, J. D. P. 2014, *ApJ*, 792, 11
- Jáchym, P., Kenney, J. D. P., Ržuička, A., et al. 2013, *A&A*, 556, A99
- Jáchym, P., Kenney, J. D. P., Sun, M., et al. 2019, *ApJ*, 883, 145
- Jáchym, P., Sun, M., Kenney, J. D. P., et al. 2017, *ApJ*, 839, 114
- Jáchym, P., Sun, M., Yagi, M., et al. 2022, *A&A*, 658, L5
- Jaffé, Y. L., Poggianti, B. M., Moretti, A., et al. 2018, *MNRAS*, 476, 4753
- Jaffé, Y. L., Smith, R., Candlish, G. N., et al. 2015, *MNRAS*, 448, 1715
- Janz, J., Salo, H., Su, A. H., & Venhola, A. 2021, *A&A*, 647, A80
- Jordán, A., Blakeslee, J. P., Côté, P., et al. 2007, *ApJS*, 169, 213
- Junais, Boissier, S., Boselli, A., et al. 2021, *A&A*, 650, A99
- Kaiser, N. 1986, *MNRAS*, 222, 323
- Kang, H. & Ryu, D. 2011, *ApJ*, 734, 18
- Kantharia, N. G., Rao, A. P., & Sirothia, S. K. 2008, *MNRAS*, 383, 173
- Kapferer, W., Kronberger, T., Weratschnig, J., et al. 2007, *A&A*, 466, 813
- Kapferer, W., Sluka, C., Schindler, S., Ferrari, C., & Ziegler, B. 2009, *A&A*, 499, 87
- Kauffmann, G., Heckman, T. M., Tremonti, C., et al. 2003, *MNRAS*, 346, 1055
- Kauffmann, G., White, S. D. M., Heckman, T. M., et al. 2004, *MNRAS*, 353, 713
- Kawata, D. & Mulchaey, J. S. 2008, *ApJ*, 672, L103
- Kenney, J. D. P., Abramson, A., & Bravo-Alfaro, H. 2015, *AJ*, 150, 59
- Kenney, J. D. P., Geha, M., Jáchym, P., et al. 2014, *ApJ*, 780, 119
- Kenney, J. D. P. & Koopmann, R. A. 1999, *AJ*, 117, 181
- Kenney, J. D. P., Tal, T., Crowl, H. H., Feldmeier, J., & Jacoby, G. H. 2008, *ApJ*, 687, L69
- Kenney, J. D. P., van Gorkom, J. H., & Vollmer, B. 2004, *AJ*, 127, 3361
- Kenney, J. D. P., Young, J. S., Hasegawa, T., & Nakai, N. 1990, *ApJ*, 353, 460
- Kennicutt, R. C., J. 1983, *AJ*, 88, 483
- Kennicutt, Robert C., J., Tamblyn, P., & Congdon, C. E. 1994, *ApJ*, 435, 22
- Kennicutt, R. C., Calzetti, D., Aniano, G., et al. 2011, *PASP*, 123, 1347
- Kennicutt, Jr., R. C. 1998, *ARA&A*, 36, 189
- Kewley, L. J., Dopita, M. A., Sutherland, R. S., Heisler, C. A., & Trevena, J. 2001, *ApJ*, 556, 121
- Kewley, L. J., Nicholls, D. C., & Sutherland, R. S. 2019, *ARA&A*, 57, 511
- Kim, W.-T. 2007, *ApJ*, 667, L5
- Koda, J., Yagi, M., Yamanoi, H., & Komiyama, Y. 2015, *ApJ*, 807, L2
- Koopmann, R. A., Haynes, M. P., & Catinella, B. 2006, *AJ*, 131, 716
- Koopmann, R. A. & Kenney, J. D. P. 2004a, *ApJ*, 613, 866
- Koopmann, R. A. & Kenney, J. D. P. 2004b, *ApJ*, 613, 851
- Köppen, J., Jáchym, P., Taylor, R., & Palouš, J. 2018, *MNRAS*, 479, 4367
- Koulouridis, E., Ricci, M., Giles, P., et al. 2018, *A&A*, 620, A20
- Koyama, S., Koyama, Y., Yamashita, T., et al. 2017, *ApJ*, 847, 137
- Kraft, R. P., Roediger, E., Machacek, M., et al. 2017, *ApJ*, 848, 27

- Kravtsov, A. V. & Borgani, S. 2012, *ARA&A*, 50, 353
- Kronberger, T., Kapferer, W., Ferrari, C., Unterguggenberger, S., & Schindler, S. 2008a, *A&A*, 481, 337
- Kronberger, T., Kapferer, W., Unterguggenberger, S., Schindler, S., & Ziegler, B. L. 2008b, *A&A*, 483, 783
- Krumholz, M. R., McKee, C. F., & Tumlinson, J. 2009, *ApJ*, 693, 216
- Kuzmin, G. 1956, *Astron. Zh.*, 33, 27
- Lake, G., Katz, N., & Moore, B. 1998, *ApJ*, 495, 152
- Lal, D. V. 2020, *ApJS*, 250, 22
- Larson, R. B., Tinsley, B. M., & Caldwell, C. N. 1980, *ApJ*, 237, 692
- Laudari, S., Jáchym, P., Sun, M., et al. 2022, *MNRAS*, 509, 3938
- Leauthaud, A., George, M. R., Behroozi, P. S., et al. 2012, *ApJ*, 746, 95
- Lee, B. & Chung, A. 2018, *ApJ*, 866, L10
- Lee, B., Chung, A., Tonnesen, S., et al. 2017, *MNRAS*, 466, 1382
- Lee, J., Kimm, T., Katz, H., et al. 2020, *ApJ*, 905, 31
- Lee, Y., Kim, S., Rey, S.-C., & Chung, J. 2021, *ApJ*, 906, 68
- Leroy, A. K., Walter, F., Brinks, E., et al. 2008, *AJ*, 136, 2782
- Leroy, A. K., Walter, F., Sandstrom, K., et al. 2013, *AJ*, 146, 19
- Lewis, I., Balogh, M., De Propriis, R., et al. 2002, *MNRAS*, 334, 673
- Li, H., Wuyts, S., Lei, H., et al. 2019a, *ApJ*, 872, 63
- Li, Y., Bryan, G. L., & Quataert, E. 2019b, *ApJ*, 887, 41
- Lisker, T., Glatt, K., Westera, P., & Grebel, E. K. 2006, *AJ*, 132, 2432
- Liu, A., Tozzi, P., Ettori, S., et al. 2020, *A&A*, 637, A58
- Liu, Q., Yee, H. K. C., Drissen, L., et al. 2021, *ApJ*, 908, 228
- Livio, M., Regev, O., & Shaviv, G. 1980, *ApJ*, 240, L83
- Lizée, T., Vollmer, B., Braine, J., & Nehlig, F. 2021, *A&A*, 645, A111
- Longobardi, A., Boselli, A., Boissier, S., et al. 2020a, *A&A*, 633, L7
- Longobardi, A., Boselli, A., Fossati, M., et al. 2020b, *A&A*, 644, A161
- Loni, A., Serra, P., Kleiner, D., et al. 2021, *A&A*, 648, A31
- Lopes, P. A. A., Ribeiro, A. L. B., & Rembold, S. B. 2017, *MNRAS*, 472, 409
- Lotz, M., Dolag, K., Remus, R.-S., & Burkert, A. 2021, *MNRAS*, 506, 4516
- Lotz, M., Remus, R.-S., Dolag, K., Biviano, A., & Burkert, A. 2019, *MNRAS*, 488, 5370
- Lovisari, L., Ettori, S., Gaspari, M., & Giles, P. A. 2021, *Universe*, 7, 139
- Luo, Y., Kang, X., Kauffmann, G., & Fu, J. 2016, *MNRAS*, 458, 366
- Machacek, M., Jones, C., Forman, W. R., & Nulsen, P. 2006, *ApJ*, 644, 155
- Machacek, M. E., Nulsen, P., Stirbat, L., Jones, C., & Forman, W. R. 2005, *ApJ*, 630, 280
- Mahajan, S., Haines, C. P., & Raychaudhury, S. 2011a, *MNRAS*, 412, 1098
- Mahajan, S., Mamon, G. A., & Raychaudhury, S. 2011b, *MNRAS*, 416, 2882
- Mahajan, S., Raychaudhury, S., & Pimblet, K. A. 2012, *MNRAS*, 427, 1252
- Maloney, P. R., Hollenbach, D. J., & Tielens, A. G. G. M. 1996, *ApJ*, 466, 561
- Mantz, A. B., Allen, S. W., Morris, R. G., et al. 2017, *MNRAS*, 472, 2877
- Manzer, L. H. & De Robertis, M. M. 2014, *ApJ*, 788, 140
- Marasco, A., Crain, R. A., Schaye, J., et al. 2016, *MNRAS*, 461, 2630
- Marcolini, A., Brighenti, F., & D'Ercole, A. 2003, *MNRAS*, 345, 1329
- Markevitch, M. & Vikhlinin, A. 2007, *Phys. Rep.*, 443, 1
- Martin, D. C., Seibert, M., Neill, J. D., et al. 2007, *Nature*, 448, 780
- Mastropietro, C., Moore, B., Mayer, L., et al. 2005, *MNRAS*, 364, 607
- Mathiesen, B., Evrard, A. E., & Mohr, J. J. 1999, *ApJ*, 520, L21
- Mayer, L., Mastropietro, C., Wadsley, J., Stadel, J., & Moore, B. 2006, *MNRAS*, 369, 1021
- McBride, J., Fakhouri, O., & Ma, C.-P. 2009, *MNRAS*, 398, 1858
- McDonald, M., Allen, S. W., Bayliss, M., et al. 2017, *ApJ*, 843, 28
- McGee, S. L., Balogh, M. L., Bower, R. G., Font, A. S., & McCarthy, I. G. 2009, *MNRAS*, 400, 937
- McGee, S. L., Bower, R. G., & Balogh, M. L. 2014, *MNRAS*, 442, L105
- McPartland, C., Ebeling, H., Roediger, E., & Blumenthal, K. 2016, *MNRAS*, 455, 2994
- Mei, S., Blakeslee, J. P., Côté, P., et al. 2007, *ApJ*, 655, 144
- Merluzzi, P., Busarello, G., Dopita, M. A., et al. 2013, *MNRAS*, 429, 1747
- Mernier, F., Biffi, V., Yamaguchi, H., et al. 2018, *Space Sci. Rev.*, 214, 129

- Merritt, D. 1983, *ApJ*, 264, 24
- Merritt, D., Graham, A. W., Moore, B., Diemand, J., & Terzić, B. 2006, *AJ*, 132, 2685
- Mieske, S., Hilker, M., & Infante, L. 2004, *A&A*, 418, 445
- Mihos, J. C., Harding, P., Feldmeier, J., & Morrison, H. 2005, *ApJ*, 631, L41
- Miley, G. 1980, *ARA&A*, 18, 165
- Miley, G. K., Perola, G. C., van der Kruit, P. C., & van der Laan, H. 1972, *Nature*, 237, 269
- Miller, N. A., Hornschemeier, A. E., Mobasher, B., et al. 2009, *AJ*, 137, 4450
- Miller, N. A. & Owen, F. N. 2001, *AJ*, 121, 1903
- Minchin, R. F., Taylor, R., Köppen, J., et al. 2019, *AJ*, 158, 121
- Mishra, H. D. & Dai, X. 2020, *AJ*, 159, 69
- Miwa, T. & Noguchi, M. 1998, *ApJ*, 499, 149
- Mok, A., Wilson, C. D., Golding, J., et al. 2016, *MNRAS*, 456, 4384
- Mok, A., Wilson, C. D., Knapen, J. H., et al. 2017, *MNRAS*, 467, 4282
- Montes, M. 2019, arXiv e-prints, [arXiv:1912.01616](https://arxiv.org/abs/1912.01616)
- Montier, L. A. & Giard, M. 2004, *A&A*, 417, 401
- Moore, B., Katz, N., Lake, G., Dressler, A., & Oemler, A. 1996, *Nature*, 379, 613
- Moore, B., Lake, G., & Katz, N. 1998, *ApJ*, 495, 139
- Moore, B., Lake, G., Quinn, T., & Stadel, J. 1999, *MNRAS*, 304, 465
- Morandi, A., Sun, M., Forman, W., & Jones, C. 2015, *MNRAS*, 450, 2261
- Moretti, A., Paladino, R., Poggianti, B. M., et al. 2018, *MNRAS*, 480, 2508
- Moretti, A., Paladino, R., Poggianti, B. M., et al. 2020a, *ApJ*, 897, L30
- Moretti, A., Paladino, R., Poggianti, B. M., et al. 2020b, *ApJ*, 889, 9
- Moretti, A., Radovich, M., Poggianti, B. M., et al. 2022, *ApJ*, 925, 4
- Mori, M. & Burkert, A. 2000, *ApJ*, 538, 559
- Morokuma-Matsui, K., Kodama, T., Morokuma, T., et al. 2021, *ApJ*, 914, 145
- Moss, C. 2006, *MNRAS*, 373, 167
- Moss, C. & Whittle, M. 1993, *ApJ*, 407, L17
- Moss, C. & Whittle, M. 2000, *MNRAS*, 317, 667
- Mostoghiu, R., Arthur, J., Pearce, F. R., et al. 2021, *MNRAS*, 501, 5029
- Mostoghiu, R., Knebe, A., Cui, W., et al. 2019, *MNRAS*, 483, 3390
- Muñoz, R. P., Eigenthaler, P., Puzia, T. H., et al. 2015, *ApJ*, 813, L15
- Müller, A., Poggianti, B. M., Pfrommer, C., et al. 2021, *Nature Astronomy*, 5, 159
- Murphy, E. J., Kenney, J. D. P., Helou, G., Chung, A., & Howell, J. H. 2009, *ApJ*, 694, 1435
- Muzzin, A., van der Burg, R. F. J., McGee, S. L., et al. 2014, *ApJ*, 796, 65
- Muzzin, A., Wilson, G., Yee, H. K. C., et al. 2012, *ApJ*, 746, 188
- Nantais, J. B., Muzzin, A., van der Burg, R. F. J., et al. 2017, *MNRAS*, 465, L104
- Nantais, J. B., van der Burg, R. F. J., Lidman, C., et al. 2016, *A&A*, 592, A161
- Navarro, J. F., Frenk, C. S., & White, S. D. M. 1997, *ApJ*, 490, 493
- Nehlig, F., Vollmer, B., & Braine, J. 2016, *A&A*, 587, A108
- Nguyen, H. T., Schulz, B., Levenson, L., et al. 2010, *A&A*, 518, L5
- Niklas, S., Klein, U., & Wielebinski, R. 1995, *A&A*, 293, 56
- Nulsen, P. E. J. 1982, *MNRAS*, 198, 1007
- Oman, K. A., Bahé, Y. M., Healy, J., et al. 2021, *MNRAS*, 501, 5073
- Oman, K. A. & Hudson, M. J. 2016, *MNRAS*, 463, 3083
- Oman, K. A., Hudson, M. J., & Behroozi, P. S. 2013, *MNRAS*, 431, 2307
- Oosterloo, T. & van Gorkom, J. 2005, *A&A*, 437, L19
- Osterbrock, D. E. & Ferland, G. J. 2006, *Astrophysics of gaseous nebulae and active galactic nuclei*
- Owen, F. N., Keel, W. C., Wang, Q. D., Ledlow, M. J., & Morrison, G. E. 2006, *AJ*, 131, 1974
- Owers, M. S., Couch, W. J., Nulsen, P. E. J., & Randall, S. W. 2012, *ApJ*, 750, L23
- Owers, M. S., Hudson, M. J., Oman, K. A., et al. 2019, *ApJ*, 873, 52
- Paccagnella, A., Vulcani, B., Poggianti, B. M., et al. 2016, *ApJ*, 816, L25
- Pallero, D., Gómez, F. A., Padilla, N. D., et al. 2022, *MNRAS*, 511, 3210
- Pappalardo, C., Lançon, A., Vollmer, B., et al. 2010, *A&A*, 514, A33
- Patej, A. & Loeb, A. 2015, *ApJ*, 798, L20
- Pearce, F. A., Kay, S. T., Barnes, D. J., Bahé, Y. M., & Bower, R. G. 2021, *MNRAS*, 507,

1606

- Pedrini, A., Fossati, M., Gavazzi, G., et al. 2022, *MNRAS*, 511, 5180
- Peluso, G., Vulcani, B., Poggianti, B. M., et al. 2021, arXiv e-prints, [arXiv:2111.02538](https://arxiv.org/abs/2111.02538)
- Peng, Y., Maiolino, R., & Cochrane, R. 2015, *Nature*, 521, 192
- Peng, Y.-j., Lilly, S. J., Kovač, K., et al. 2010, *ApJ*, 721, 193
- Persic, M. & Salucci, P. 1991, *ApJ*, 368, 60
- Pillepich, A., Nelson, D., Hernquist, L., et al. 2018, *MNRAS*, 475, 648
- Pimblet, K. A., Shabala, S. S., Haines, C. P., Fraser-McKelvie, A., & Floyd, D. J. E. 2013, *MNRAS*, 429, 1827
- Pinzke, A., Oh, S. P., & Pfrommer, C. 2013, *MNRAS*, 435, 1061
- Planck Collaboration, Adam, R., Ade, P. A. R., et al. 2016, *A&A*, 596, A104
- Planck Collaboration, Ade, P. A. R., Aghanim, N., et al. 2013, *A&A*, 554, A140
- Poggianti, B. M. & Barbaro, G. 1997, *A&A*, 325, 1025
- Poggianti, B. M., Bridges, T. J., Komiyama, Y., et al. 2004, *ApJ*, 601, 197
- Poggianti, B. M., Fasano, G., Omizzolo, A., et al. 2016, *AJ*, 151, 78
- Poggianti, B. M., Gullieuszik, M., Tonnesen, S., et al. 2019a, *MNRAS*, 482, 4466
- Poggianti, B. M., Ignesti, A., Gitti, M., et al. 2019b, *ApJ*, 887, 155
- Poggianti, B. M., Jaffé, Y. L., Moretti, A., et al. 2017a, *Nature*, 548, 304
- Poggianti, B. M., Moretti, A., Gullieuszik, M., et al. 2017b, *ApJ*, 844, 48
- Porter, S. C., Raychaudhury, S., Pimblet, K. A., & Drinkwater, M. J. 2008, *MNRAS*, 388, 1152
- Postman, M., Franx, M., Cross, N. J. G., et al. 2005, *ApJ*, 623, 721
- Postman, M. & Geller, M. J. 1984, *ApJ*, 281, 95
- Puchwein, E., Springel, V., Sijacki, D., & Dolag, K. 2010, *MNRAS*, 406, 936
- Quilis, V., Moore, B., & Bower, R. 2000, *Science*, 288, 1617
- Quilis, V., Planelles, S., & Ricciardelli, E. 2017, *MNRAS*, 469, 80
- Radovich, M., Poggianti, B., Jaffé, Y. L., et al. 2019, *MNRAS*, 486, 486
- Ramatsoku, M., Serra, P., Poggianti, B. M., et al. 2020, *A&A*, 640, A22
- Ramatsoku, M., Serra, P., Poggianti, B. M., et al. 2019, *MNRAS*, 487, 4580
- Ramos-Martínez, M., Gómez, G. C., & Pérez-Villegas, Á. 2018, *MNRAS*, 476, 3781
- Randall, S., Nulsen, P., Forman, W. R., et al. 2008, *ApJ*, 688, 208
- Rasmussen, J., Ponman, T. J., & Mulchaey, J. S. 2006, *MNRAS*, 370, 453
- Rasmussen, J., Ponman, T. J., Verdes-Montenegro, L., Yun, M. S., & Borthakur, S. 2008, *MNRAS*, 388, 1245
- Rawle, T. D., Altieri, B., Egami, E., et al. 2014, *MNRAS*, 442, 196
- Reddy, N. A. & Yun, M. S. 2004, *ApJ*, 600, 695
- Rémy-Ruyer, A., Madden, S. C., Galliano, F., et al. 2014, *A&A*, 563, A31
- Rengarajan, T. N., Karnik, A. D., & Iyengar, K. V. K. 1997, *MNRAS*, 290, 1
- Renzini, A. & Andreon, S. 2014, *MNRAS*, 444, 3581
- Reynolds, T. N., Westmeier, T., Staveley-Smith, L., Chauhan, G., & Lagos, C. D. P. 2020, *MNRAS*, 493, 5089
- Rhee, J., Smith, R., Choi, H., et al. 2020, *ApJS*, 247, 45
- Rhee, J., Smith, R., Choi, H., et al. 2017, *ApJ*, 843, 128
- Roberts, I. D. & Parker, L. C. 2020, *MNRAS*, 495, 554
- Roberts, I. D., Parker, L. C., Brown, T., et al. 2019, *ApJ*, 873, 42
- Roberts, I. D., van Weeren, R. J., McGee, S. L., et al. 2021a, *A&A*, 650, A111
- Roberts, I. D., van Weeren, R. J., McGee, S. L., et al. 2021b, *A&A*, 652, A153
- Roberts, I. D., van Weeren, R. J., Timmerman, R., et al. 2022, *A&A*, 658, A44
- Roediger, E. & Brüggen, M. 2007, *MNRAS*, 380, 1399
- Roediger, E. & Brüggen, M. 2008, *MNRAS*, 388, 465
- Roediger, E., Brüggen, M., & Hoeft, M. 2006, *MNRAS*, 371, 609
- Roediger, E., Brüggen, M., Owers, M. S., Ebeling, H., & Sun, M. 2014, *MNRAS*, 443, L114
- Roediger, E. & Hensler, G. 2005, *A&A*, 433, 875
- Roediger, E. & Hensler, G. 2008, *A&A*, 483, 121
- Roediger, E., Kraft, R. P., Nulsen, P., et al. 2013, *MNRAS*, 436, 1721
- Roediger, E., Kraft, R. P., Nulsen, P. E. J., et al. 2015, *ApJ*, 806, 103
- Roman-Oliveira, F., Chies-Santos, A. L., Ferrari, F., Lucatelli, G., & Rodríguez Del Pino, B. 2021, *MNRAS*, 500, 40

- Roman-Oliveira, F. V., Chies-Santos, A. L., Rodríguez del Pino, B., et al. 2019, *MNRAS*, 484, 892
- Rubin, V. C., Whitmore, B. C., & Ford, W. Kent, J. 1988, *ApJ*, 333, 522
- Rudnick, G., Hodge, J., Walter, F., et al. 2017, *ApJ*, 849, 27
- Ruszkowski, M., Brügggen, M., Lee, D., & Shin, M.-S. 2014, *ApJ*, 784, 75
- Ruszkowski, M. & Oh, S. P. 2011, *MNRAS*, 414, 1493
- Rybicki, G. B. & Lightman, A. P. 1979, *Radiative processes in astrophysics*
- Sabater, J., Best, P. N., & Argudo-Fernández, M. 2013, *MNRAS*, 430, 638
- Sabater, J., Best, P. N., & Heckman, T. M. 2015, *MNRAS*, 447, 110
- Safarzadeh, M. & Loeb, A. 2019, *MNRAS*, 486, L26
- Safarzadeh, M. & Scannapieco, E. 2017, *ApJ*, 850, 99
- Salomé, P., Combes, F., Edge, A. C., et al. 2006, *A&A*, 454, 437
- Salomé, P., Combes, F., Revaz, Y., et al. 2011, *A&A*, 531, A85
- Sanders, J. S., Fabian, A. C., Sun, M., et al. 2014, *MNRAS*, 439, 1182
- Sandstrom, K. M., Leroy, A. K., Walter, F., et al. 2013, *ApJ*, 777, 5
- Sarazin, C. L. 1986, *Reviews of Modern Physics*, 58, 1
- Sardaneta, M. M., Amram, P., Boselli, A., et al. 2022, *A&A*, 659, A45
- Sarzi, M., Iodice, E., Coccato, L., et al. 2018, *A&A*, 616, A121
- Schaefer, A. L., Croom, S. M., Allen, J. T., et al. 2017, *MNRAS*, 464, 121
- Schaefer, A. L., Croom, S. M., Scott, N., et al. 2019, *MNRAS*, 483, 2851
- Schaye, J. 2004, *ApJ*, 609, 667
- Schaye, J., Crain, R. A., Bower, R. G., et al. 2015, *MNRAS*, 446, 521
- Schindler, S., Binggeli, B., & Böhringer, H. 1999, *A&A*, 343, 420
- Schindler, S., Kapferer, W., Domainko, W., et al. 2005, *A&A*, 435, L25
- Schulz, S. & Struck, C. 2001, *MNRAS*, 328, 185
- Scott, T. C., Bravo-Alfaro, H., Brinks, E., et al. 2010, *MNRAS*, 403, 1175
- Scott, T. C., Brinks, E., Cortese, L., Boselli, A., & Bravo-Alfaro, H. 2018, *MNRAS*, 475, 4648
- Scott, T. C., Cortese, L., Brinks, E., et al. 2012, *MNRAS*, 419, L19
- Scott, T. C., Cortese, L., Lagos, P., et al. 2022, *MNRAS*, 511, 980
- Scott, T. C., Usero, A., Brinks, E., et al. 2013, *MNRAS*, 429, 221
- Scott, T. C., Usero, A., Brinks, E., et al. 2015, *MNRAS*, 453, 328
- Scudder, J. M., Ellison, S. L., Torrey, P., Patton, D. R., & Mendel, J. T. 2012, *MNRAS*, 426, 549
- Sellwood, J. A. 2014, *Reviews of Modern Physics*, 86, 1
- Sellwood, J. A. & Carlberg, R. G. 1984, *ApJ*, 282, 61
- Serra, P., de Blok, W. J. G., Bryan, G. L., et al. 2016, in *MeerKAT Science: On the Pathway to the SKA*, 8
- Serra, P., Koribalski, B., Duc, P.-A., et al. 2013, *MNRAS*, 428, 370
- Seth, A. C., Dalcanton, J. J., & de Jong, R. S. 2005, *AJ*, 130, 1574
- Shattow, G. M., Croton, D. J., Skibba, R. A., et al. 2013, *MNRAS*, 433, 3314
- Sheardown, A., Fish, T. M., Roediger, E., et al. 2019, *ApJ*, 874, 112
- Sheen, Y.-K., Smith, R., Jaffé, Y., et al. 2017, *ApJ*, 840, L7
- Shin, M.-S. & Ruszkowski, M. 2014, *MNRAS*, 445, 1997
- Shostak, G. S., Hummel, E., Shaver, P. A., van der Hulst, J. M., & van der Kruit, P. C. 1982, *A&A*, 115, 293
- Sijacki, D., Vogelsberger, M., Kereš, D., Springel, V., & Hernquist, L. 2012, *MNRAS*, 424, 2999
- Simionescu, A., Werner, N., Mantz, A., Allen, S. W., & Urban, O. 2017, *MNRAS*, 469, 1476
- Simionescu, A., ZuHone, J., Zhuravleva, I., et al. 2019, *Space Sci. Rev.*, 215, 24
- Singh, A., Gulati, M., & Bagla, J. S. 2019, *MNRAS*, 489, 5582
- Sivanandam, S., Rieke, M. J., & Rieke, G. H. 2010, *ApJ*, 717, 147
- Sivanandam, S., Rieke, M. J., & Rieke, G. H. 2014, *ApJ*, 796, 89
- Skibba, R. A., Masters, K. L., Nichol, R. C., et al. 2012, *MNRAS*, 423, 1485
- Skillman, E. D., Kennicutt, Robert C., J., Shields, G. A., & Zaritsky, D. 1996, *ApJ*, 462, 147
- Smith, R., Fellhauer, M., & Assmann, P. 2012a, *MNRAS*, 420, 1990
- Smith, R. J., Lucey, J. R., Hammer, D., et al. 2010, *MNRAS*, 408, 1417

- Smith, R. J., Lucey, J. R., Price, J., Hudson, M. J., & Phillipps, S. 2012b, *MNRAS*, 419, 3167
- Solanes, J. M., Manrique, A., García-Gómez, C., et al. 2001, *ApJ*, 548, 97
- Solomon, P. M., Rivolo, A. R., Barrett, J., & Yahil, A. 1987, *ApJ*, 319, 730
- Sorce, J. G., Blaizot, J., & Dubois, Y. 2019, *MNRAS*, 486, 3951
- Sorce, J. G., Dubois, Y., Blaizot, J., et al. 2021, *MNRAS*, 504, 2998
- Sorce, J. G., Gottlöber, S., Hoffman, Y., & Yepes, G. 2016, *MNRAS*, 460, 2015
- Sorgho, A., Hess, K., Carignan, C., & Oosterloo, T. A. 2017, *MNRAS*, 464, 530
- Sparks, W. B., Pringle, J. E., Donahue, M., et al. 2009, *ApJ*, 704, L20
- Sparre, M., Pfrommer, C., & Ehlert, K. 2020, *MNRAS*, 499, 4261
- Spitzer, L. 1978, *Physical processes in the interstellar medium*
- Springel, V., White, S. D. M., Jenkins, A., et al. 2005, *Nature*, 435, 629
- Starikova, S., Vikhlinin, A., Kravtsov, A., et al. 2020, *ApJ*, 892, 34
- Stein, Y., Bomans, D. J., Ferguson, A. M. N., & Dettmar, R. J. 2017, *A&A*, 605, A5
- Steinhauser, D., Haider, M., Kapferer, W., & Schindler, S. 2012, *A&A*, 544, A54
- Steinhauser, D., Schindler, S., & Springel, V. 2016, *A&A*, 591, A51
- Stevens, A. R. H., Diemer, B., Lagos, C. d. P., et al. 2019, *MNRAS*, 490, 96
- Stevens, A. R. H., Lagos, C. d. P., Cortese, L., et al. 2021, *MNRAS*, 502, 3158
- Steyrleithner, P., Hensler, G., & Boselli, A. 2020, *MNRAS*, 494, 1114
- Strazzullo, V., Pannella, M., Mohr, J. J., et al. 2019, *A&A*, 622, A117
- Stroe, A., Sobral, D., Dawson, W., et al. 2015, *MNRAS*, 450, 646
- Stroe, A., Sobral, D., Paulino-Afonso, A., et al. 2017, *MNRAS*, 465, 2916
- Su, Y., Kraft, R. P., Roediger, E., et al. 2017, *ApJ*, 834, 74
- Sun, M. 2012, *New Journal of Physics*, 14, 045004
- Sun, M., Donahue, M., Roediger, E., et al. 2010, *ApJ*, 708, 946
- Sun, M., Donahue, M., & Voit, G. M. 2007a, *ApJ*, 671, 190
- Sun, M., Ge, C., Luo, R., et al. 2022, *Nature Astronomy*, 6, 270
- Sun, M., Jones, C., Forman, W., et al. 2006, *ApJ*, 637, L81
- Sun, M., Jones, C., Forman, W., et al. 2007b, *ApJ*, 657, 197
- Sun, M. & Vikhlinin, A. 2005, *ApJ*, 621, 718
- Sun, M., Voit, G. M., Donahue, M., et al. 2009, *ApJ*, 693, 1142
- Tabatabaei, F. S., Schinnerer, E., Krause, M., et al. 2017, *ApJ*, 836, 185
- Tacconi, L. J., Genzel, R., Saintonge, A., et al. 2018, *ApJ*, 853, 179
- Tan, B., Oh, S. P., & Gronke, M. 2021, *MNRAS*, 502, 3179
- Taranu, D. S., Hudson, M. J., Balogh, M. L., et al. 2014, *MNRAS*, 440, 1934
- Taylor, J. E. & Babul, A. 2001, *ApJ*, 559, 716
- Taylor, R., Davies, J. I., Auld, R., & Minchin, R. F. 2012, *MNRAS*, 423, 787
- Thilker, D. A., Bianchi, L., Meurer, G., et al. 2007, *ApJS*, 173, 538
- Toloba, E., Boselli, A., Cenarro, A. J., et al. 2011, *A&A*, 526, A114
- Toloba, E., Boselli, A., Gorgas, J., et al. 2009, *ApJ*, 707, L17
- Toloba, E., Boselli, A., Peletier, R. F., et al. 2012, *A&A*, 548, A78
- Toloba, E., Guhathakurta, P., Boselli, A., et al. 2015, *ApJ*, 799, 172
- Tonnesen, S. & Bryan, G. L. 2009, *ApJ*, 694, 789
- Tonnesen, S. & Bryan, G. L. 2010, *ApJ*, 709, 1203
- Tonnesen, S. & Bryan, G. L. 2012, *MNRAS*, 422, 1609
- Tonnesen, S. & Bryan, G. L. 2021, *ApJ*, 911, 68
- Tonnesen, S., Bryan, G. L., & Chen, R. 2011, *ApJ*, 731, 98
- Tonnesen, S., Bryan, G. L., & van Gorkom, J. H. 2007, *ApJ*, 671, 1434
- Tonnesen, S. & Stone, J. 2014, *ApJ*, 795, 148
- Trayford, J. W., Theuns, T., Bower, R. G., et al. 2016, *MNRAS*, 460, 3925
- Troncoso-Iribarren, P., Padilla, N., Santander, C., et al. 2020, *MNRAS*, 497, 4145
- Truong, N., Rasia, E., Biffi, V., et al. 2019, *MNRAS*, 484, 2896
- Trussler, J., Maiolino, R., Maraston, C., et al. 2020, *MNRAS*, 491, 5406
- Upadhyay, A. K., Oman, K. A., & Trager, S. C. 2021, *A&A*, 652, A16
- Valluri, M. 1993, *ApJ*, 408, 57
- van de Voort, F., Bahé, Y. M., Bower, R. G., et al. 2017, *MNRAS*, 466, 3460
- van den Bosch, F. C., Aquino, D., Yang, X., et al. 2008, *MNRAS*, 387, 79
- van der Burg, R. F. J., McGee, S., Aussel, H., et al. 2018, *A&A*, 618, A140

- van der Burg, R. F. J., Muzzin, A., Hoekstra, H., et al. 2013, *A&A*, 557, A15
- van der Wel, A., Franx, M., van Dokkum, P. G., et al. 2014, *ApJ*, 788, 28
- van Dokkum, P. G., Abraham, R., Merritt, A., et al. 2015, *ApJ*, 798, L45
- Vaughan, S. P., Tiley, A. L., Davies, R. L., et al. 2020, *MNRAS*, 496, 3841
- Vazza, F., Eckert, D., Simionescu, A., Brügggen, M., & Ettori, S. 2013, *MNRAS*, 429, 799
- Veilleux, S., Bland-Hawthorn, J., Cecil, G., Tully, R. B., & Miller, S. T. 1999, *ApJ*, 520, 111
- Verdes-Montenegro, L., Yun, M. S., Williams, B. A., et al. 2001, *A&A*, 377, 812
- Verdugo, C., Combes, F., Dasyra, K., Salomé, P., & Braine, J. 2015, *A&A*, 582, A6
- Vijayaraghavan, R. & Ricker, P. M. 2015, *MNRAS*, 449, 2312
- Vijayaraghavan, R. & Ricker, P. M. 2017, *ApJ*, 841, 38
- Vikhlinin, A., Kravtsov, A., Forman, W., et al. 2006, *ApJ*, 640, 691
- Vogelsberger, M., Genel, S., Springel, V., et al. 2014, *MNRAS*, 444, 1518
- Vogelsberger, M., Marinacci, F., Torrey, P., et al. 2018, *MNRAS*, 474, 2073
- Vogelsberger, M., McKinnon, R., O’Neil, S., et al. 2019, *MNRAS*, 487, 4870
- Voit, G. M. 2005, *Reviews of Modern Physics*, 77, 207
- Völk, H. J. & Xu, C. 1994, *Infrared Physics and Technology*, 35, 527
- Vollmer, B. 2003, *A&A*, 398, 525
- Vollmer, B., Balkowski, C., Cayatte, V., van Driel, W., & Huchtmeier, W. 2004a, *A&A*, 419, 35
- Vollmer, B., Beck, R., Kenney, J. D. P., & van Gorkom, J. H. 2004b, *AJ*, 127, 3375
- Vollmer, B., Braine, J., Balkowski, C., Cayatte, V., & Duschl, W. J. 2001a, *A&A*, 374, 824
- Vollmer, B., Braine, J., Combes, F., & Sofue, Y. 2005a, *A&A*, 441, 473
- Vollmer, B., Braine, J., Pappalardo, C., & Hily-Blant, P. 2008a, *A&A*, 491, 455
- Vollmer, B., Cayatte, V., Balkowski, C., & Duschl, W. J. 2001b, *ApJ*, 561, 708
- Vollmer, B., Cayatte, V., Boselli, A., Balkowski, C., & Duschl, W. J. 1999, *A&A*, 349, 411
- Vollmer, B., Fossati, M., Boselli, A., et al. 2021, *A&A*, 645, A121
- Vollmer, B. & Huchtmeier, W. 2003, *A&A*, 406, 427
- Vollmer, B. & Huchtmeier, W. 2007, *A&A*, 462, 93
- Vollmer, B., Huchtmeier, W., & van Driel, W. 2005b, *A&A*, 439, 921
- Vollmer, B., Marcelin, M., Amram, P., et al. 2000, *A&A*, 364, 532
- Vollmer, B., Pappalardo, C., Soida, M., & Lançon, A. 2018, *A&A*, 620, A108
- Vollmer, B., Soida, M., Beck, R., et al. 2013, *A&A*, 553, A116
- Vollmer, B., Soida, M., Beck, R., et al. 2007, *A&A*, 464, L37
- Vollmer, B., Soida, M., Braine, J., et al. 2012, *A&A*, 537, A143
- Vollmer, B., Soida, M., Chung, A., et al. 2010, *A&A*, 512, A36
- Vollmer, B., Soida, M., Chung, A., et al. 2009, *A&A*, 496, 669
- Vollmer, B., Soida, M., Chung, A., et al. 2008b, *A&A*, 483, 89
- Vollmer, B., Soida, M., Otmianowska-Mazur, K., et al. 2006, *A&A*, 453, 883
- von der Linden, A., Wild, V., Kauffmann, G., White, S. D. M., & Weinmann, S. 2010, *MNRAS*, 404, 1231
- Vulcani, B., Fritz, J., Poggianti, B. M., et al. 2020, *ApJ*, 892, 146
- Vulcani, B., Poggianti, B. M., Finn, R. A., et al. 2010, *ApJ*, 710, L1
- Vulcani, B., Poggianti, B. M., Jaffé, Y. L., et al. 2018, *MNRAS*, 480, 3152
- Vulcani, B., Poggianti, B. M., Moretti, A., et al. 2021, *ApJ*, 914, 27
- Vulcani, B., Treu, T., Schmidt, K. B., et al. 2016, *ApJ*, 833, 178
- Walker, S., Simionescu, A., Nagai, D., et al. 2019, *Space Sci. Rev.*, 215, 7
- Wang, J., Fu, J., Aumer, M., et al. 2014, *MNRAS*, 441, 2159
- Wang, J., Koribalski, B. S., Serra, P., et al. 2016, *MNRAS*, 460, 2143
- Wang, J., Staveley-Smith, L., Westmeier, T., et al. 2021, *ApJ*, 915, 70
- Wang, Q. D., Owen, F., & Ledlow, M. 2004, *ApJ*, 611, 821
- Warmels, R. H. 1986, HI properties of spiral galaxies in the Virgo cluster
- Warmels, R. H. 1988a, *A&AS*, 72, 19
- Warmels, R. H. 1988b, *A&AS*, 72, 57
- Warmels, R. H. 1988c, *A&AS*, 72, 427
- Weinberg, M. D. 2014, *MNRAS*, 438, 3007
- Weinmann, S. M., Kauffmann, G., von der Linden, A., & De Lucia, G. 2010, *MNRAS*, 406, 2249
- Wetzel, A. R., Tinker, J. L., Conroy, C., & van den Bosch, F. C. 2013, *MNRAS*, 432, 336

- Weżgowiec, M., Vollmer, B., Ehle, M., et al. 2011, *A&A*, 531, A44
- Wheeler, C., Phillips, J. L., Cooper, M. C., Boylan-Kolchin, M., & Bullock, J. S. 2014, *MNRAS*, 442, 1396
- Whitmore, B. C., Gilmore, D. M., & Jones, C. 1993, *ApJ*, 407, 489
- Wilson, C. D., Warren, B. E., Israel, F. P., et al. 2009, *ApJ*, 693, 1736
- Winkel, N., Pasquali, A., Kraljic, K., et al. 2021, *MNRAS*, 505, 4920
- Wolf, C., Aragón-Salamanca, A., Balogh, M., et al. 2009, *MNRAS*, 393, 1302
- Wong, O. I., Kenney, J. D. P., Murphy, E. J., & Helou, G. 2014, *ApJ*, 783, 109
- Wood, R. A., Jones, C., Machacek, M. E., et al. 2017, *ApJ*, 847, 79
- Woudt, P. A., Kraan-Korteweg, R. C., Lucey, J., Fairall, A. P., & Moore, S. A. W. 2008, *MNRAS*, 383, 445
- Xie, L., De Lucia, G., Wilman, D. J., et al. 2018, *MNRAS*, 480, 3812
- Yagi, M., Gu, L., Fujita, Y., et al. 2013, *ApJ*, 778, 91
- Yagi, M., Gu, L., Koyama, Y., et al. 2015, *AJ*, 149, 36
- Yagi, M., Koda, J., Komiyama, Y., & Yamanoi, H. 2016, *ApJS*, 225, 11
- Yagi, M., Komiyama, Y., Yoshida, M., et al. 2007, *ApJ*, 660, 1209
- Yagi, M., Yoshida, M., Gavazzi, G., et al. 2017, *ApJ*, 839, 65
- Yagi, M., Yoshida, M., Komiyama, Y., et al. 2010, *AJ*, 140, 1814
- Yamagami, T. & Fujita, Y. 2011, *PASJ*, 63, 1165
- Yates, R. M., Thomas, P. A., & Henriques, B. M. B. 2017, *MNRAS*, 464, 3169
- Yoon, H., Chung, A., Smith, R., & Jaffé, Y. L. 2017, *ApJ*, 838, 81
- Yoshida, M., Ohyama, Y., Iye, M., et al. 2004, *AJ*, 127, 90
- Yoshida, M., Yagi, M., Komiyama, Y., et al. 2012, *ApJ*, 749, 43
- Yoshida, M., Yagi, M., Komiyama, Y., et al. 2008, *ApJ*, 688, 918
- Yoshida, M., Yagi, M., Okamura, S., et al. 2002, *ApJ*, 567, 118
- Yun, K., Pillepich, A., Zinger, E., et al. 2019, *MNRAS*, 483, 1042
- Zabel, N., Davis, T. A., Smith, M. W. L., et al. 2019, *MNRAS*, 483, 2251
- Zaritsky, D., Donnerstein, R., Dey, A., et al. 2019, *ApJS*, 240, 1
- Zhang, B., Sun, M., Ji, L., et al. 2013, *ApJ*, 777, 122
- Zibetti, S., Charlot, S., & Rix, H.-W. 2009, *MNRAS*, 400, 1181
- Zubko, V., Dwek, E., & Arendt, R. G. 2004, *ApJS*, 152, 211
- Zuhone, J. A. & Roediger, E. 2016, *Journal of Plasma Physics*, 82, 535820301